Metamaterial-Inspired Frequency-Selective Surfaces

by

Farhad Bayatpur

A dissertation submitted in partial fulfillment
of the requirements for the degree of
Doctor of Philosophy
(Electrical Engineering)
in The University of Michigan
2009

Doctoral Committee:
Professor Kamal Sarabandi, Chair
Professor Eric Michielssen
Professor Stephen Rand
Professor Christopher Ruf
Assistant Professor Anthony Grbic

to my parents,

Fataneh *and* Hossein

to my cousin,

Reza

ACKNOWLEDGEMENTS

This work would not have been possible without the support of my parents, especially my mother, and my cousin, Mohammadreza Ghahri, over past four years. Thank you Dad and Mom!

I would like to thank my advisor, Professor Kamal Sarabandi, for giving me this opportunity to work with him. It has been a rewarding experience.

I would like to also thank my doctoral committee, Professor Steven Rand, Professor Eric Michielssen, Professor Anthony Grbic, and Professor Chris Ruf for their support and guidance.

I would like to acknowledge the support and guidance of my professors at Sharif University of Technology, Professor Sima Noghanian, Professor Ali Banai, Professor Masoumeh Nasiri-Kenari.

Special thanks to my close friends, Danial Ehyaie, Vahed Qazvinian, Alexis Frank, Hadi Zarkoob, and Dr. Seyed Alireza Tabatabaeenejad to whom I owe a lot.

I would like to thank Mr. Brendan Casey at The University of Michigan Solid-State Electronics Laboratory (SSEL) for helping me in the fabrication and assembly of my circuits.

I would like to thank my colleagues and friends at the Radiation Lab and EECS, Ms. Karla Johnson, Seyed Mohammadreza Faghih-Imani, Dr. Adib Nashashibi, Dr. Amelia Burkle, Dr. Dongsook Kim, Dr. Mojtaba Dehmollaian, Dr. Nader Behdad, Dr. Reza Azadegan, Dr. Wonbin Hong, Dr. Juseop Lee, Dr. Mona Jarrahi, Dr. Mohammadreza Abidian, Dr. Javid Moraveji, Dr. Behzad Ebrahimi, Dr. Kamran Entesari, Morteza Nick, Mariko Buergin, Abdulkadir Yucel, Meysam Moallem, Mehrnoosh Vahidpoor, Adel El-Sherbini, Jackie Vitaz, Scott Rudolph, Yuriy Goykhman, Amit Patel, Mark Haynes, Fikadu Dagefu, Michael Benson, Pelumi Osoba, Felipe Valdes, Young Jun Song, Michael Thiel, Jessie Duan,

Jane Whitcomb, Hatim Bukhari, Onur Bakir, Jungsuek Oh, Sangjo Choi, Line van Nieuwstadt, Dr. Karl Brakora, Mojtaba Mehrara, Ali Besharatian, ...

Finally, I would like to thank my friends at The University of Michigan Swing Dance Club.

Farhad Bayatpur

August 16, 2009

TABLE OF CONTENTS

LIST OF FIGURES

Figure

LIST OF TABLES

LIST OF APPENDICES

ABSTRACT

Metamaterial-Inspired Frequency-Selective Surfaces

by

Farhad Bayatpur

Chair: Kamal Sarabandi

This dissertation presents a new approach to designing spatial filters (frequency-selective surfaces) having extensive applications in communications and radar systems. Unlike conventional surfaces composed of resonance-length elements, the new structures use sub-wavelength elements, and therefore, operate in TEM mode. Consequently, their frequency response is harmonic-free up to a frequency where their elements' dimensions become comparable with the wavelength, λ. Hence, their behavior is well described through quasi-static circuit models. These surfaces, which will be referred to as miniaturized-element surfaces, are easily synthesized since filter theory and circuit simulators can be utilized in their design process. The small dimensions of the elements of the surface and its TEM mode of operation decrease the surface sensitivity to the incidence angle of the excitation (plane-wave). This allows the application of such surfaces in conjunction with phased-arrays and their placement in close proximity ($< \lambda/10$) to an antenna. These surfaces can also operate properly with smaller panel dimensions.

The theory of the new surfaces is introduced in Chapter 3 where a surface consisting of an array of $\lambda/12$-long elements is presented. The transmission response of this surface includes a passband and a transmission zero. For this design, the first harmonic is located at a frequency six times higher than the operation frequency. Using varactors, frequency tuning of nearly an octave is shown. Chapter 4 presents multipole spatial filters. Through an accurate circuit

model, dual-bandpass and maximally flat filters that are $\lambda/240$ thick are demonstrated. Chapter 5 introduces a reconfigurable surface that produces a frequency response with two operation modes: bandstop and bandpass. In addition, using varactors, the center frequency and the bandwidth are tuned independently. The discussion on tunability is continued in Chapter 6 which introduces another varactor-tuned structure that operates, similar to the previous designs, without additional biasing circuitry for the varactors. However, this structure is immune to single point failure as it uses a parallel biasing method. Finally, Chapter 7 demonstrates a $\lambda/10$-thick, coupled filter-antenna array to achieve a high-order filtering for beamforming systems. This design eliminates the need for integrating bulky RF filters required in the receive chain of each element of the system.

CHAPTER 1

Introduction

1.1 Overview

The purpose of this research is to develop new microwave, spatial filters for communication and radar systems that can provide improved functionality and performance. Spatial filters, or frequency-selective surfaces, are formed by periodic arrays of usually metallic elements on a dielectric substrate. Once exposed to the electromagnetic radiation, such surfaces generate a scattered wave with a prescribed frequency response. Currently, frequency-selective surfaces are in use as radomes for antennas and controlling their radar cross-section. The complexity in the design of existing frequency-selective surfaces and their required size and sensitivity to the angle of incidence limit their functionality, thus showing the demand for improving their characteristics. Specific characteristics that we have focused on in this research are the low dependence of the frequency-selective surface on the incidence angle of the exciting wave, the low harmonic content of the frequency response, the ability to operate in a close proximity to a radiation source. In addition, we require these surfaces operability with small dimensions of the frequency-selective surface panel compared to the wavelength. In this chapter, an overview of traditional methods in frequency-selective surface design compared with the new approach is provided, demonstrating performance superior to that of traditional frequency-selective surface allowed in the new method.

A comprehensive study of the previous methods in design of frequency-selective surface revealed that in general they obey a fundamental constraint on the length of elements of

the surface; the dimensions of the elements must be about half of the electromagnetic wavelength at the frequency of operation. On the other hand, one can intuitively deduce hat a smaller periodicity in a periodic array leads to less variability in the induced electric current distribution, which in turn results in a frequency response less sensitivity to the incidence angle. With this background, design of the new frequency-selective surface was started with the goal of producing an inherent frequency selectivity in the surface.

Using sub-wavelength elements, the proposed surfaces produce excellent filtering characteristics. The most unique feature of the proposed approach is its ability to localize frequency selectivity. This feature introduces frequency-selective surfaces with high-order frequency responses that have very low sensitivities with respect to the incidence angle. In addition, these spatial filters can perform properly even at a close distance of about a tenth of the wavelength to an antenna. The localized characteristic also implies that the new surfaces, unlike traditional designs, can take up a small area in comparison to the wavelength and still maintain their frequency-selective properties. Moreover, the frequency responses of the new frequency-selective surfaces are independent of structurally-based resonances given the small size of the elements over the band of operation. This creates harmonic-free surfaces.

Throughout this dissertation, both physical and numerical interpretations of the spectral behavior of the new frequency-selective surface structures are provided. Physical insight into the operation mechanism is the key to further improvements and allows for the creation of more complex surfaces with desired frequency responses.

1.2 Background

Filters play a fundamental role in almost electronic or RF circuit. Once being incorporated into a design, the filter acts as a device that controls the frequency content of the signal for mitigating noise and unwanted interference. Filters are categorized, based on their function, into three major groups: lowpass, bandpass, and highpass filters. A lowpass filter, for example, allows for the lower frequencies to pass through the circuitry and blocks higher frequencies.

Frequency-selective surface (or dichroic) structures to space waves are the counterparts

Figure 1.1: Radomes at the Cryptologic Operations Center, Misawa, Japan (photo courtesy of en. Wikipedia).

of filters in transmission lines. Once exposed to the electromagnetic radiation, a frequency-selective surface (FSS) acts like a spatial filter; some frequency bands are transmitted and some are reflected. In a way, an FSS can be a cover for hiding communication facilities. This is probably the first potential application of FSS structures, as they have actually been used as covers named radomes. Radomes are bandpass FSS filters that are used to reduce the radar cross-section (RCS) of an antenna system outside its frequency band of operation. Fig. 1.1 shows the radomes at the Cryptologic Operation Center in Japan.

Since the early 1960's, because of potential military applications, FSS structures have been the subject of intensive study [1–3]. Marconi and Franklin, however, are believed, [1], to be the early pioneers in this area for their contribution of a parabolic reflector made using half-wavelength wire sections in 1919 [4]. FSSs as frequency-selective materials have been used traditionally in stealth technology for reducing the RCS of communications systems.

The concept of stealth or being able to operate without the knowledge of the enemy has always been a goal of military technology (see Fig. 1.2). In order to minimize the detection, FSS layers cover the facilities to reduce the RCS.

Figure 1.2: Stealth attack plane (photo courtesy of en. Wikipedia).

FSSs most commonly take the form of planar, periodic metal-dielectric arrays in two-dimensional space. Frequency behavior of an FSS is entirely determined by the geometry of the surface in one period (unit cell) provided that the surface size is infinite. A periodic array of patch elements is shown in Fig. 1.3. This array is shown to have a capacitive frequency characteristic.

Although taking different shapes, conventional FSSs have similar operation mechanisms that can be explained by the phenomenon of resonance. Consider an array of elements on a

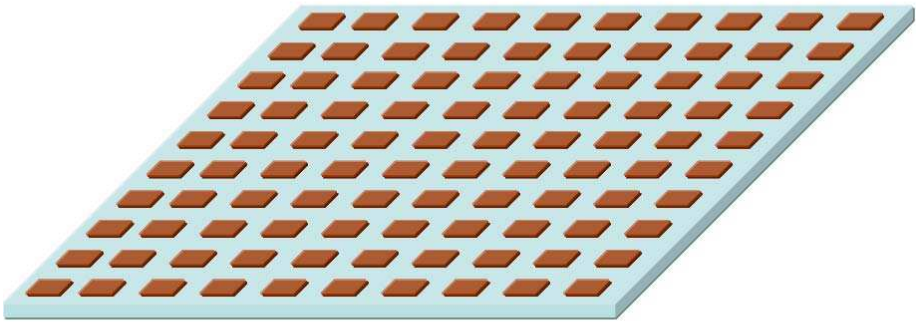

Figure 1.3: Two-dimensional periodic array of patch elements.

planar surface. Upon contact with a plane-wave, the elements of the periodic surface resonate at frequencies where the effective length of the elements is a multiple of the resonance length, $\lambda/2$ [2,12]. Corresponding to the phase front of the wave, these elements have a certain phase delay. As a result, the scattered radiations of individual elements add up coherently. An example of such arrangement of elements is Marconi and Franklin's reflector. This reflector is very much similar to the most famous FSS design, an array of half-wave dipoles. A large reflector antenna constructed using wire-grids is shown in Fig. 1.4.

The resonance characteristics of a resonance-length based FSS usually depend on the way the surface is exposed to the electromagnetic wave. This includes the effective aperture size of the FSS and the incidence angle of the wave. The dependence of the FSS frequency response with respect to these factors could be a major drawback for some applications. As a result, over the years new ideas have been sought to overcome the issue of the dependence on the size and angle. Besides the two major problems mentioned above, harmonics are another effect that influence the performance of an FSS. The situation becomes more involved given that the harmonics of the intended frequency are themselves dependent upon the incidence angle.

A new approach in design of FSS is introduced in this thesis which achieves an inherent frequency-selective characteristic in the surface [38]. In a way, the constitutive parameters of the surface are manipulated such that the material itself shows selectivity. Such manipu-

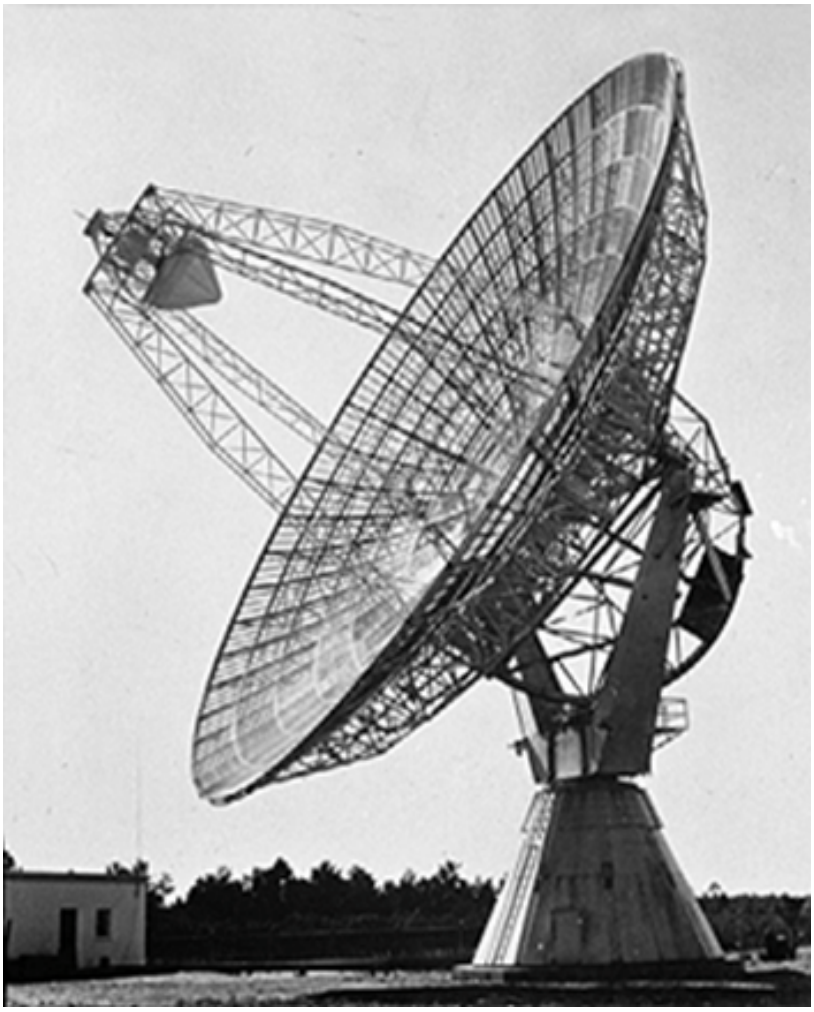

Figure 1.4: Reflector antenna for sattelite communications- The reflector dish is made up of wire sections or dipoles (photo courtesy of en. Wikipedia).

lations are possible in sub-wavelength regime where the elements of the FSS are on the order of $\lambda/10$ or smaller in dimension. In other words, this dissertation takes an approach in which special, artificial materials are designed which are used as thin-layer frequency-selective surfaces. It will be shown that the very small size of the inclusions (FSS elements) on the surface makes it possible to describe the behavior of the FSS using a quasi-static analysis in which the electric and magnetic fields are assumed to be uniform over the elements. The result of this analysis offers useful insight into the physics of the structure, which will be formulated through an equivalent circuit model representing the FSS.

This violation of the old rule of thumb in FSS design, i.e. using resonant length elements ($\lambda/2$), features interesting behaviors. Unique feature of the new design is its localized frequency-selective property, as mentioned above, which results in suppression of harmonics of the intended frequency response. Moreover, by designing the unit cell appropriately, very thin FSS layers with high-order frequency responses and a very low sensitivity with respect to the incidence angle of the wave are achieved.

Characteristics of an FSS made up of an array of elements depend upon many design parameters including the shape of the elements and their lattice geometry. In an introductory fashion, these parameters are presented in the following.

1.3 Elements of Design in Traditional Frequency-Selective Surfaces

As mentioned previously, FSS structures are periodic arrays of special elements printed on a substrate. For numerical analysis, such arrays are assumed to be infinite in dimension as FSSs usually consist of many elements. The infinite array approximation reduces the whole problem of analysis to calculating the frequency response of a single element in the array given the periodic nature of the FSSs. A brief overview of the available FSS elements is provided in this section.

1.3.1 Element Geometries

In general, the FSS structures can be categorized into two major groups: patch-type elements and aperture-type elements. As an introduction to FSS structures two complementary planar arrays, array of patches and array of slots, are usually considered. A simple structure consisting of periodic array of metallic patches (Fig. 1.5) has been shown to have a low-pass characteristic [12–14]. Once hit by a plane-wave, this surface transmits low-frequency content of the wave and reflects the higher frequencies. Another observation is to consider such an array as a capacitive surface given its frequency response provided in Fig. 1.5. The complementary structure (see Fig. 1.5) has an inductive response, hence acting as a highpass

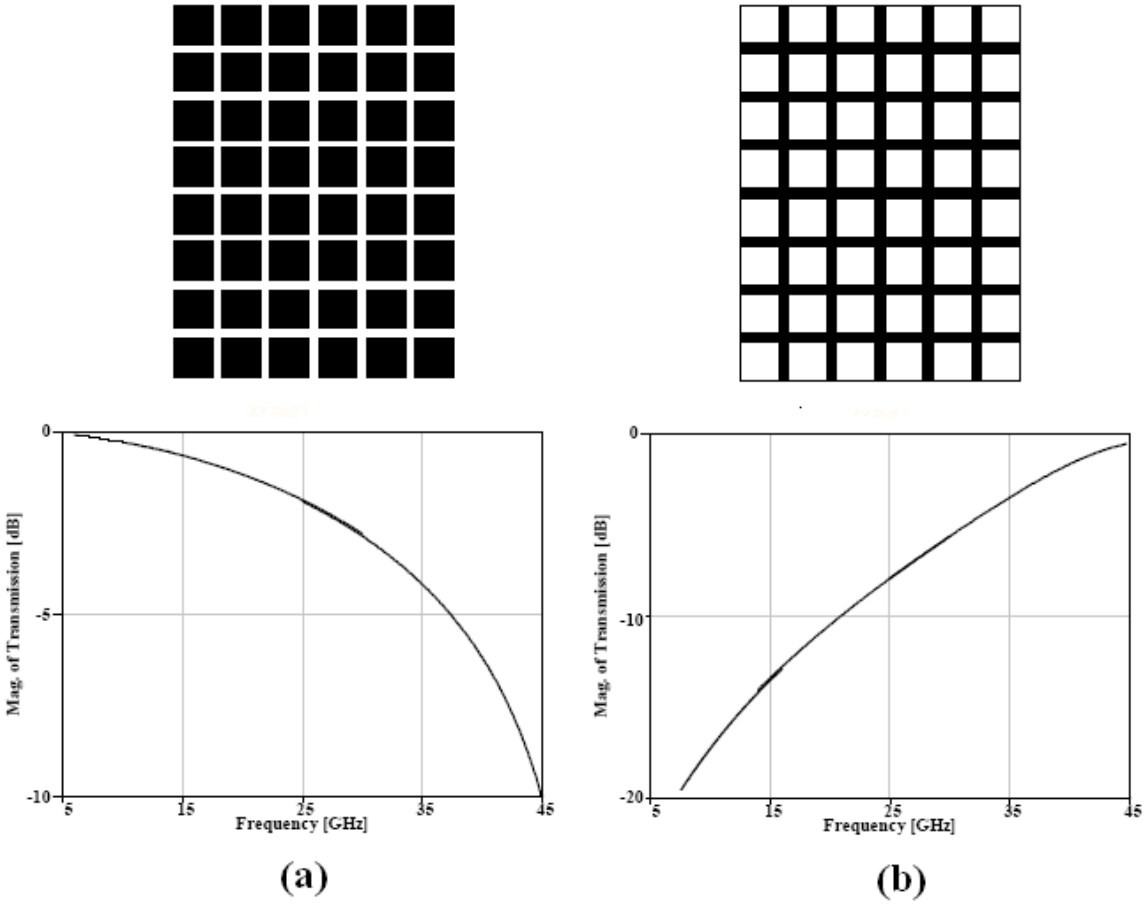

Figure 1.5: Periodic structures comprising of complimentary elements, patches and slots (wire-grid), and their surface impedance- The patch-array produces a capacitive response, whereas the array of slots is inductive [2].

filter. As it will be discussed later, inductive and capacitive surfaces can be put together to produce a desired filter response.

Over the years, a variety of FSS elements were introduced for bandpass and bandstop applications. A complete list of these elements is collected in [1–3]. This list includes an array of the following: circular shapes [14, 15, 36]; metallic plates such as rectangles and dipoles [16, 17, 19, 20], cross-poles, tripoles, and Jerusalem cross [21–25, 39, 40, 52]; three- or four-legged dipoles [26]; rings [27–29, 44]; square loops [30–34]; and gridded square loops [32, 35]; etc. (see Fig. 1.6).

Depending on the application requirements, different FSS designs can be chosen to fulfill

the demands. These requirements usually include level of dependence on the incidence angle of the incoming wave; level of cross-polarization; bandwidth; and level of band separation. A comparison between some of the most famous FSS designs is provided in Table. 1.1 based on the above criteria [2]. As shown, for instance, the dipole array is very sensitive to the angle.

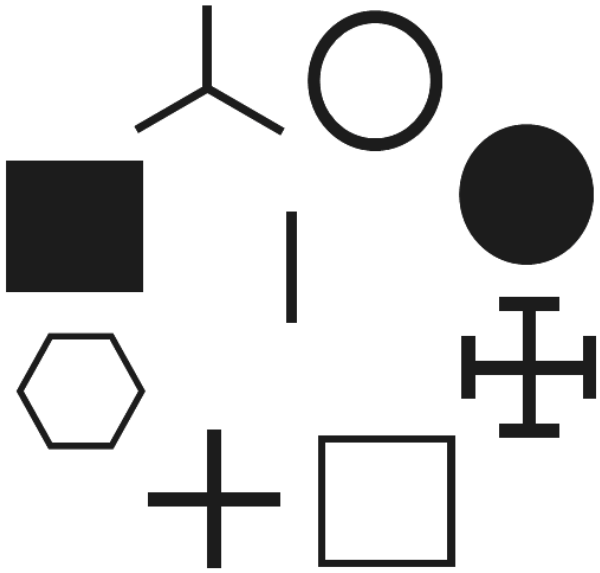

Figure 1.6: A variety of FSS elements over past decades.

1.3.2 Element Dimensions

As mentioned above, FSSs are traditionally designed based on the resonant elements. A planar array of strip dipoles, for example, produces a frequency response consisting of multiple notches at frequencies where the length of the dipoles is a multiple of half a wavelength. A similar effect can explain the operation of other elements. The square loop element, for example, can be imagined as two dipoles that are connected to one another at each end. Using the same argument as that of the dipole, a loop resonates when the length of the two sides equals the length of a resonant dipole, $\lambda/2$. In other words, each side of the loop is

Table 1.1: Comparison Between the Performance of the Common FSS Elements [2]

Element	Angle independence	Cross-polarization level	Larger bandwidth	Smaller band separation
Loaded dipole	1	2	1	1
Jerusalem cross	2	3	2	2
Rings	1	2	1	1
Tripole	3	3	3	2
Crossed dipole	3	3	3	3
Square loop	1	1	1	1
Dipole	4	1	4	1

about $\lambda/4$.

Although the shape of the elements has the utmost importance effect in the frequency response, the way these elements are arranged in the array format is also part of the design work. Moreover, the response also depends on the characteristics of the substrate used. This in fact becomes very important as we will present a square loop element whose sides are as small as $\lambda/12$ [38]. This is where the miniaturized-element FSS design comes to picture. Elements that are much smaller than the wavelength are designed to create capacitive gaps and inductive traces. By thinning and miniaturizing the unit cell, capacitive junctions in the form of shunt or series capacitors are achieved. Inductive traces are also held very close to one another to produce a larger inductive effect as a result of mutual magnetic coupling.

1.4 Applications of Frequency-Selective Surfaces

Originally introduced as spatial filters, FSS structures have been employed in a variety of other applications. As mentioned earlier, radomes are types of bandpass FSSs that are used in conjunction with an antenna system to reduce the RCS of the antenna outside its frequency band of operation. FSSs have been considered in design of multi-frequency reflector antennas, [39,40,43,48], for science investigations and data communication links. A proposed single high-gain antenna along with an FSS subreflector is illustrated in Fig. 1.7, [49]. This

arrangement allows a Cassegrain configuration at X- (7.2 and 8.4 GHz) and Ka- (32 and 34.5 GHz) bands and a prime focus configuration at S- (2.3 GHz) and Ku- (13.8 GHz) bands.

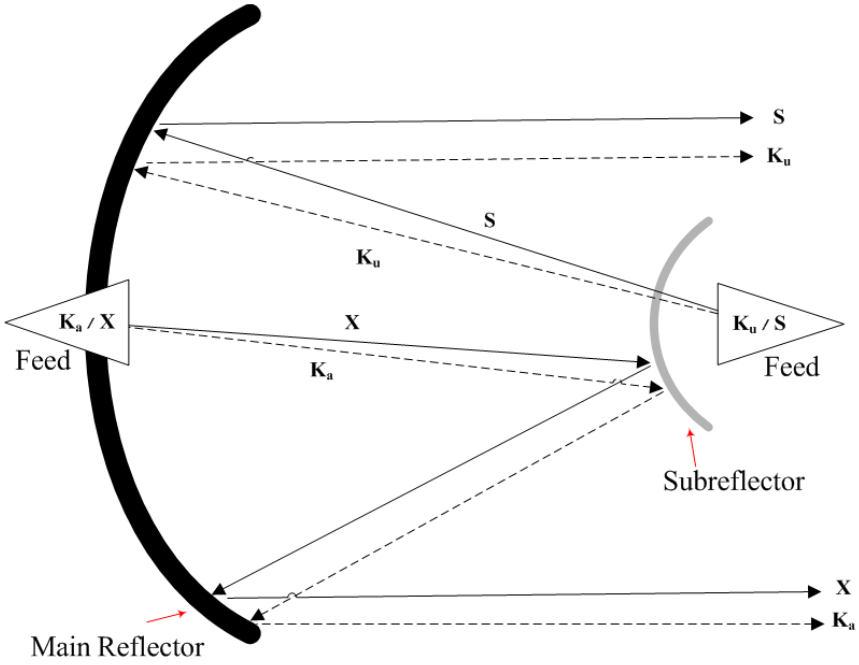

Figure 1.7: Proposed Cassini high-gain antenna (HGA) with a four-frequency FSS [49].

Having reflective charactersitics with a certain phase and amplitude, frequency-selective surfaces can be used in design of reactive impedance surfaces [50]. This idea, which was shown experimentally in [53] for phase shifting, opens a whole new area of research, in addition to frequency filtering, in which FSS structures are utilized to produce a desired reactive response. FSS structures have been used in design of artificial magnetic conductors (AMC) (or high-impedance surfaces) and electromagnetic bandgap (EBG) materials. Bearing particular reactive behaviors, these engineered structures are constructed based on FSS in a straightforward fashion provided below.

A famous example of AMC structures is the Sievenpiper's high-impedance surface presented in a systematic fashion in [58]. This AMC was used as a ground plane for antenna applications in order to suppress the surface waves inside the substrate. Unlike an electric conductor, which allows for flow of the electric current, a magnetic conductor cannot support any electric current, which in turn bans the propagation of surface waves inside the substrate. Sievenpiper's surface is shown in Fig. 1.8, which is basically a circuit-board com-

prising an array of metal protrusions (so-called mushroom elements) on a metallic layer in a 2-D periodic fashion. This architecture, for a wave propagating along the surface, acts like a transmission line with a forbidden frequency band (bandgap). The bandgap frequency of this transmission line is designed so that the surface waves are trapped in the bandgap. As a result, the substrate no longer supports the surface waves. Reducing the undesired waves in the substrate, high-impedance surfaces have been employed in construction of antennas to improve the performance [59].

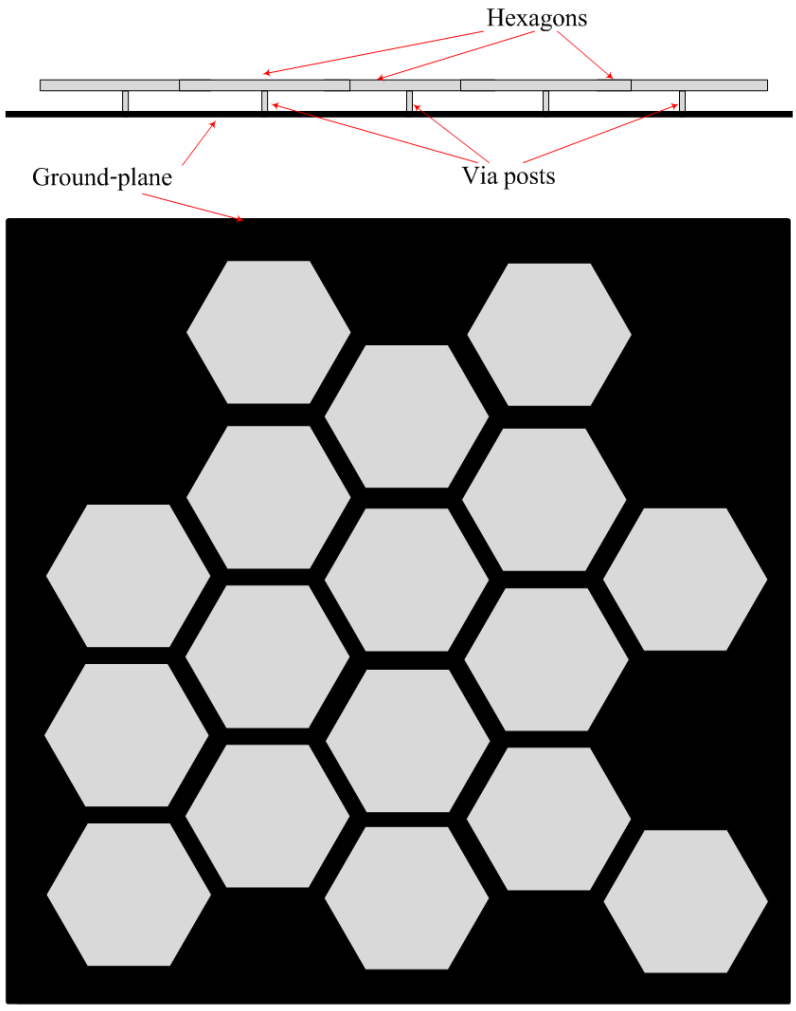

Figure 1.8: Cross-section (top) and the top view (bottom) of Sievenpiper's high-impedance surface [58]

An AMC in a way can be observed as a surface with a large surface impedance. Ideally,

for a plane-wave incident upon the surface, the transverse wave impedance at the AMC surface is infinite. The transverse impedance is defined as the ratio of the transverse electric field over the transverse magnetic field, E_t/H_t. An infinite impedance here corresponds to $H_t \approx 0$, meaning that the surface cannot bear a tangential magnetic field and hence the name magnetic conductor. This is analogous to an electric conductor which shorts the electric field. An easy way of explaining this effect is based on the transmission line theory. Through a $\lambda/4$ impedance inverter, a short impedance is transformed to an open impedance. This basic idea is actually used in design of corrugated surfaces behaving as an open circuit in terms of wave impedance [60, 61]. A corrugated, reactive surface is illustrated in Fig. 1.9.

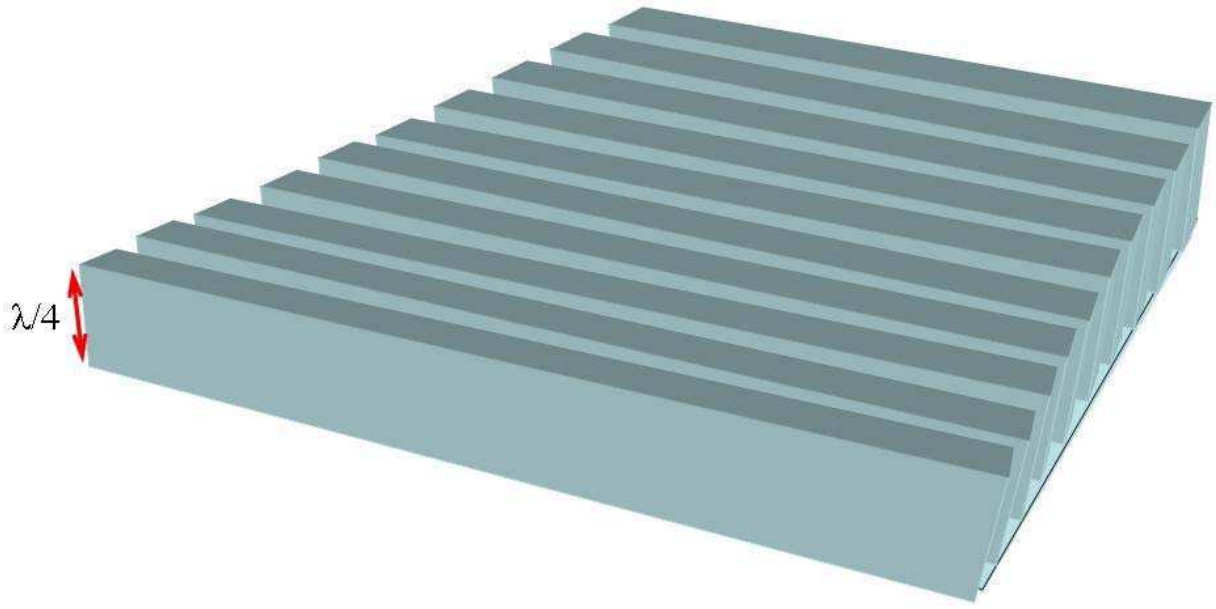

Figure 1.9: A corrugated surface acting as an artificial magnetic conductor (AMC)- The zero impedance of the ground-plane is transformed into an open impedance through the quarter-wave corrugations acting as transmission line stubs.

The problem with the AMC provided in Fig. 1.9 is apparently the overall large thickness of the surface which is $\lambda/4$. Layers of FSS can be used to resolve this issue. An FSS can be designed to produce the required phase shift ($\lambda/4$) for the impedance transformation. The advantage of this method is that the FSS can be very thin, thus eliminating the issue of

height. This way, a thinner AMC is built because the FSS layer produces a steeper phase characteristic along a very thin layer. Apart from AMC, antenna technology can benefit from special types of ground planes designed to couple appropriately with the antenna in order to enhance the performance. In [74], for example, an FSS ground plane is used to increase the bandwidth.

Another area of interest is the application of FSS as a superstrate over the printed antennas to improve their radiation chracteristics. The problem of enhancing the gain of printed circuit antennas has been extensively studied by Jackson and Alexpoulos [65, 66]. A stack of electric and magnetic superstrate layers once arranged and chosen properly is shown

Figure 1.10: Modern architecture- Glass is considered as an inevitable material in modern architecture (photo courtesy of XoaS Design)

to behave like a lens on top of the antenna that bends the rays emanating from the antenna and incident upon the interface of the substrate and the stack of the superstrates according to Snell's law. A transmission line modeling of the multiple layers can be used to find the proper values for the parameters of the layers to achieve the highest gain [67]. FSS, as a reactive surface, has been used in design of superstrates. In [73], an FSS is placed on top of a patch antenna to increase the directivity.

The applications introduced above are rather technical and far away from the real life scenarios. Recently, metal-glass sheets, that are optically transparent but are selective at lower frequencies, have found applications in modern architecture. This introduces a new approach in designing a secure indoor communication network given that glass plays an important role in modern styles of construction nowadays [75, 76]. A glass building is shown in Fig. 1.10.

Such glasses are now commercialized; for example, Nippon is one of the manufacturers in this area [77]. They design a shield film for windows that can shield the desired frequency, which could be either 2.45 GHz for wireless local area network (LAN) applications or 1.9 GHz for Personal Hand-Phone System (PHS) applications. In this research, the challenge is probably finding the proper materials. A variety of opaque materials need to be tested. The choice of material is influenced by two factors: 1) the conductivity of material, which significantly affects FSS performance, and 2) the width of the material, which affects both the resistance of the FSS element and the optical transparency. Silver paint is a potential material that has been used in practice.

1.5 Applications of Miniaturized-Element Frequency-Selective Surfaces

Recently, there has been an interest in design of frequency selective surfaces with unit cell dimensions much smaller than a wavelength. In traditional designs, the frequency-selective properties result from mutual interactions of the elements. Therefore, to observe a desired frequency selective behavior, a large number of unit cells must be present. Consequently,

the overall size of the surface is electrically large. On the other hand, for some applications where a low sensitivity with respect to the incidence angle of the exciting wave is required or in cases where a uniform phase front is difficult to establish, the screen size needs to be small. To address this problem, miniaturized-element frequency-selective surfaces were proposed. The first generation of such surfaces appeared in [37] which was followed by the second generation, introduced in [38], showing a remarkable improvement and enhanced performance.

After introducing the new FSS structures in this dissertation, a few potential applications for such thin-layer FSS structures are discussed. Being made out of very thin substrates, the new FSSs are used as building-blocks of higher-order spatial filters that are made by cascading single-layer FSS layers. Moreover, given the spacial shape of their unit cells, the new surfaces can be loaded with the surface-mount varactor diodes to achieve tunable filter characteristics. The proposed FSS structures enable implementation of higher-order spatial filters over low-profile, conformal antenna arrays.

A super-thin FSS-antenna structure will be presented using a planar antenna covered with a layer of FSS. This FSS-antenna can be utilized to reduce the complexity associated with the vertical integration of beamforming arrays. In addition to improving the antenna performance (selectivity), this method allows for eliminating the bandpass filter needed in the receive path of each antenna element in the beamformer. The latter is important since in steering array designs thousands of such lumped filter components are required. The advantage of using the new surfaces, as opposed to conventional superstrates or FSSs, is that such surfaces can be positioned at a close distance ($< \lambda/10$) to the antenna. Ordinary superstrates are placed over the antennas through a half-wave spacer. Although being very close to the antenna, the miniaturized FSS structures have a very minor effect on the radiation performance of the antenna. This way, the new achievement is the practical demonstration of thin-layer FSS-antenna structures.

1.6 Chapter Outline

1.6.1 Chapter 1: Introduction

In Chapter 1, the motivations and goals of this research are first presented. Next, a brief overview of the past work done in the area of frequency-selective surfaces is provided. Following the introduction section, this dissertation first performs a more comprehensive overview on the available FSS designs, including a discussion for each case to study the design in more detail. After this overview, the new approach, miniaturized-element FSS, is presented. Next, available analysis methods, including common numerical methods and modeling tools, are presented. Finally, the comprehensive section will discuss applications of the FSS structures, including those of the new, state-of-the-art design. These sections are listed below.

1.6.2 Chapter 2: Traditional Frequency-Selective Surfaces: Design, Characterization, and Applications

Frequency-selective surface structures, with resonant unit cells, have been investigated over the years for a variety of applications. As a result of research on the applications mentioned earlier, the behavior of frequency selective surfaces is well understood. In this chapter, a number of FSS elements provided in the literature are introduced.

Numerical analyses of FSS problems are done using various techniques [14, 19, 23, 29, 36, 78, 84]. In the simulation setup, the FSS is treated as an infinite periodic structure, thus reducing the problem size to a single unit cell. The formulation is based on constructing an integral equation for the unit cell. Then the formulation is modified given the periodic arrangement of the cells. Floquet's theorem is applied to the formulation such that the continuous convolution integral is converted to an infinite summation with each summand being a product of the spectral Green's function and the spectral equivalent surface current.

Transmission and reflection characteristics of FSS screens can be measured through a few methods [78]. A common measurement setup consists of two standard horn antennas and a vector network analyzer (VNA). The tests are performed in an anechoic chamber which

simulates a free-space environment. This will be discussed in more detail.

1.6.3 Chapter 3: Metamaterial-Based Miniaturized-Element Frequency-Selective Surfaces

A new design methodology of FSS structures utilizing elements, that are as small as $\lambda/12$ in dimension, is presented in this chapter. Unique features of the new design include localized frequency selective properties, high-order frequency response achieved by a single substrate, lack of passband harmonics in the frequency response, and very low frequency response sensitivity to the incidence angle. High-order frequency response is accomplished through the application of a thin substrate that allows considerable couplings between the elements on the two sides of the substrate. The coupling between the layers in conjunction with each layer characteristics is designed to produce a high-Q, bandpass frequency response, in addition to one or more transmission zeros.

Equivalent circuit modeling of FSS structures is used commonly for a qualitative description of frequency-selective surfaces [24,52]. Using a quasi-static approach, the elements of the periodic array are modeled as inductive and capacitive components loading a transmission line segment. Another approach for modeling, [21], uses antenna array theory and proper modeling of mutual impedance of the FSS elements. Circuit modeling, however, is accurate up to the first order as the circuit ignores higher order Floquet modes. Harmonics of the first resonance are therefore missing in the circuit response. Although not accurate, the circuit model approach is intuitive and gives a physical insight into the behavior of an FSS which is important from a design-level point of view.

1.6.4 Chapter 4: Multipole Miniaturized-Element Frequency-Selective Surfaces

Super-thin, multipole frequency-selective surfaces based on the elements of the miniaturized approach are presented in this chapter. New miniaturized elements are developed to achieve a low thickness and an improved functionality. First, design of a very thin-layer modified miniaturized FSS producing a single-pole bandpass response in addition to

a transmission zero is presented. The modified design is a single-sided circuit-board with a particular unit cell. Next, using similar metallic pattern on the other side of the substrate, a dual-bandpass frequency response is produced. This response is achieved by choosing proper dimensions for the loops and wire of each layer and by appropriately positioning the layers with respect to each other. To establish a benchmark, dual-pole FSSs are created using the conventional method of cascading single-pole FSSs. The single-pole FSS, designed in Chapter 3, is used here as the layers of the benchmark dual-pole FSSs. The proposed dual-bandpass FSS has a thickness of $\lambda/240$ which is six times thinner than the benchmark FSSs.

1.6.5 Chapter 5: Fully Reconfigurable Miniaturized-Element Frequency-Selective Surfaces

A feature of interest in design of FSS structures is the ability to electronically tune the frequency response of these structures. In this chapter another miniaturized FSS is presented whose bandpass frequency response is not only tunable but also transformable from bandpass to bandstop and vice versa. This varactor-tuned surface shows a wide tuning range over a practical capacitance range which is tested and verified through measurements in a waveguide, using lumped capacitors. This chapter establishes the fundamentals of the reconfigurable design and closes with a thorough, practical procedure for fabrication of the actual varactor-loaded surface for operation in a free-space environment.

1.6.6 Chapter 6: An Electronically Tunable Miniaturized-Element Frequency-Selective Surface without Bias Network

In this chapter, the tunability of FSS is discussed as a practical issue. Potential methods of tuning of the new FSS are studied. A practical varactor-tuned FSS will be presented which uses its own metallic traces for biasing the varactors, the main challenge in the tuning. This way no external bias circuitry is required. In [85–93], frequency tunability has been accomplished by altering the substrate constitutive parameters. Other methods include either changing the structure geometry using RF-MEMS technology [96,97], or manipulating

the reactive characteristics of the layers of the FSS by incorporating tuning elements into the layers' design [102–104, 106, 107].

The purpose of this chapter is to demonstrate a new architecture that can conveniently be implemented with varactors. This miniaturized-element FSS consists of two wire layers along with connecting via sections built on a very thin substrate. The design exhibits a bandpass characteristic which can be tuned using varactors mounted on one side of the substrate.

1.6.7 Chapter 7: A Super-Thin, Metamaterial-Based FSS-Antenna Array for Scanned Array Applications

The discussion on the applications of FSS continues in this chapter. The discussion focuses on the application of FSS as antenna superstrates and starts with a more involved overview on the past designs. Next, potential applications that are tightly dependent on the new features provided by the miniaturized-element FSSs are presented. Finally, an FSS-antenna array will be presented with an extremely low profile. In this array, the FSS is intended to perform frequency filtering over an array of patch antennas. The new achievement is a new filter-antenna that is only $\lambda/10$ thick.

1.6.8 Chapter 8: Conclusion

In this chapter, a summary of important elements of this dissertation are provided. This, followed by a discussion on the future potentials, concludes the dissertation.

CHAPTER 2

Traditional Frequency-Selective Surfaces: Design, Characterization, and Applications

Periodic structures, or arrangements of equally spaced, identical elements, have been of interest in many areas of physics and engineering. Although being very old from mathematical stand view, periodic structures have also a long history of development from more practical perspectives. In fact, these arrangements were considered in an engineering design problem over 200 years ago by the physicist David Rittenhouse [14]. He invented a grating with equally-spaced hairs [11]. A periodic structure can be optimized for a particular application which requires certain characteristics. This process includes designing the elements as well as the way they are placed in the periodic array.

2.1 Chapter Introduction

A frequency-selective surface (FSS) is a periodic, planar assembly of generally metallic elements on a dielectric layer. It is built in conjunction with the electromagnetic waves in order to "tailor" an electromagnetic link in the free-space environment. Acting as a barrier for the waves propagating along the link, the FSS controls the flow of the electromagnetic energy. The transfer function of the FSS manipulates the spectral content of the wave. As a result, some of the frequency constituents of the wave are blocked, and some pass through the FSS fence. In another perspective, an FSS is analogous to a filter in circuit theory. For their filtering effects, FSS structures are also called spatial filters in electromagnetic engineering.

There are many examples in real world which clearly confirm the importance of having knowledge about periodic structures. Consider a reflective surface which is to be built by least amount of metallization at a given frequency. Intuitively, the fist observation is that the less the metal is, the weaker the reflection becomes. Now, consider two possibilities: using an array of long strips or an array of short dipoles. Having a larger metalized area, the long strip is expected to produce a stronger reflection, according to our very first observation. Rigorous analysis of the two candidates, however, reveals that the dipole array can actually produce a total reflectivity at a certain frequency, whereas the array of strips never becomes totally reflective. This problem, which was studied by Marconi and Franklin when they proposed their reflector antenna [4], can be explained through modeling the two arrays using circuit theory. This is shown in Fig. 2.1 where the model for the array of long strips is just an inductor, while the array of dipoles is an $L-C$ circuit. The dipole array, therefore, becomes

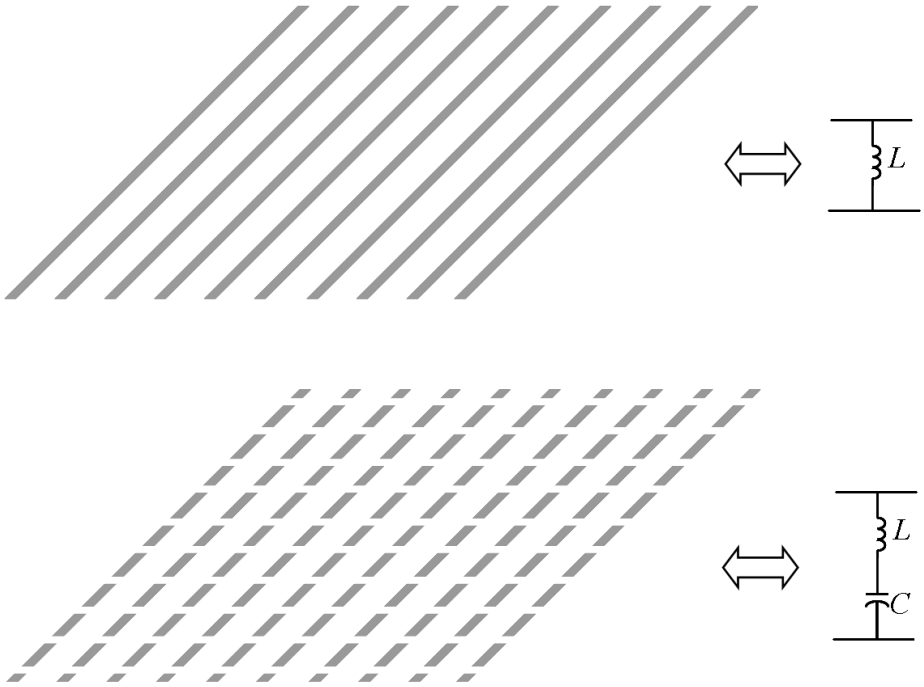

Figure 2.1: A periodic array of infinitely long metallic strips (top) produces an inductive characteristic, whereas an infinite array of closely-spaced dipoles (bottom) produces a notch frequency behavior which in turn results in a total reflectivity at the resonance frequency of the notch. In this way, although the dipole array uses less metallic area, it produces a complete reflective state [1].

total reflective at the frequency of resonance of the $L-C$ circuit.

Following the brief discussions highlighted in Chapter 1, this chapter overviews some of the past, famous FSS structures, including the physical interpretation of their operation. The overview section is followed by a discussion on the methods of characterization and modeling of FSS. Finally, later in this chapter, a more detailed overview on the applications of FSS is presented.

2.2 Overview of the Elements of Traditional Frequency-Selective Surfaces

The operation mechanism of traditional FSSs, as mentioned in Chapter 1, is based on the resonant elements. Simply, the idea is that a plane-wave illuminates an array of metallic elements, thus exciting electric current on the elements. The amplitude of the generated current depends on the strength of the coupling of energy between the wave and the elements. The coupling reaches its highest level at the fundamental frequency where the length of elements is a $\lambda/2$. As a result, the elements are shaped so that they are resonant near the frequency of operation. Depending on its distribution, the current itself acts as an electromagnetic source, thus producing a scattered field. The scattered field added to the incident field constitutes the total field in the space surrounding the FSS. By controlling the scattered field (designing elements), therefore, the required filter response is produced which can be seen in the spectrum of the total field. As mentioned above, the distribution of the current on the elements determines the frequency behavior of the FSS. The current itself depends on the shape of the elements.

Given the dependence of the traditional FSS on the length, excitation of the higher-order modes, in addition to the first fundamental mode, becomes inevitable. As a result, the frequency response of the traditional FSS usually has a high harmonic content. The first and the second possible modes are shown in Fig. 2.2. The issue of harmonics not only affects the frequency characteristics of the FSS but also degrades its scan performance because some of the harmonics may be excited only when the incidence angle changes from normal to the

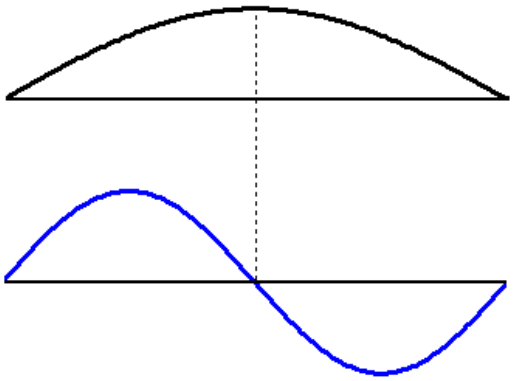

Figure 2.2: The first and the second resonant modes- (top) shows the fundamental mode (frequency f_f) which is excited for any element shape irrespective os the incidence angle. (bottom) shows the first odd mode at about $2f_f$ which may be excited only at oblique incidence. The frequency of this mode may change slightly depending on the element shape [1].

FSS plane.

Although the geometry of the elements has a critical influence on the filtering behavior, there are other parameters that can affect the frequency response. This could be the choice of the parameters of the substrate supporting the elements of the FSS and also its inter-element spacing. The substrate is shown to affect both the frequency of operation and the bandwidth of the response. The spacing between the elements, on the other hand, points out the issue of the grating lobe which is inherent in any array radiator; the larger the spacing, the earlier the onset of the grating lobes. As a result, a smaller inter-element spacing is usually preferred. However, the spacing can also change the bandwidth; a larger spacing in general produces a narrower bandwidth [1].

To develop a better understanding of operation of FSS structures, a comparative study over different types of FSS is provided here. But, first, we need to somehow categorize FSS structures. There are a number of constraints based upon which FSSs are classified. Here, we use Munk's approach in classifying frequency-selective surfaces which is based on the shape of the elements [1].

In Fig. 2.3, four major categories of FSS arrangements are demonstrated which are:

I) The center connected or N-poles, such as dipole, three-legged element, the Jerusalem cross, and the square spiral.

II) The loop types such as the three- and four-legged loaded elements, the circular loops,

and the square and hexagonal loops.

III) Solid interiors or plate types.

IV) Combinations.

Each class along with simulated examples are presented next. All the simulation results belong to the book by Munk on FSS, [1], and use a substrate with dielectric constant of ϵ_r = 2.2 with the thickness of 0.5 mm. The examples were intended for operation at 10 GHz. The simulated results show the performance for both TE and TM polarizations at 0^o and 45^o.

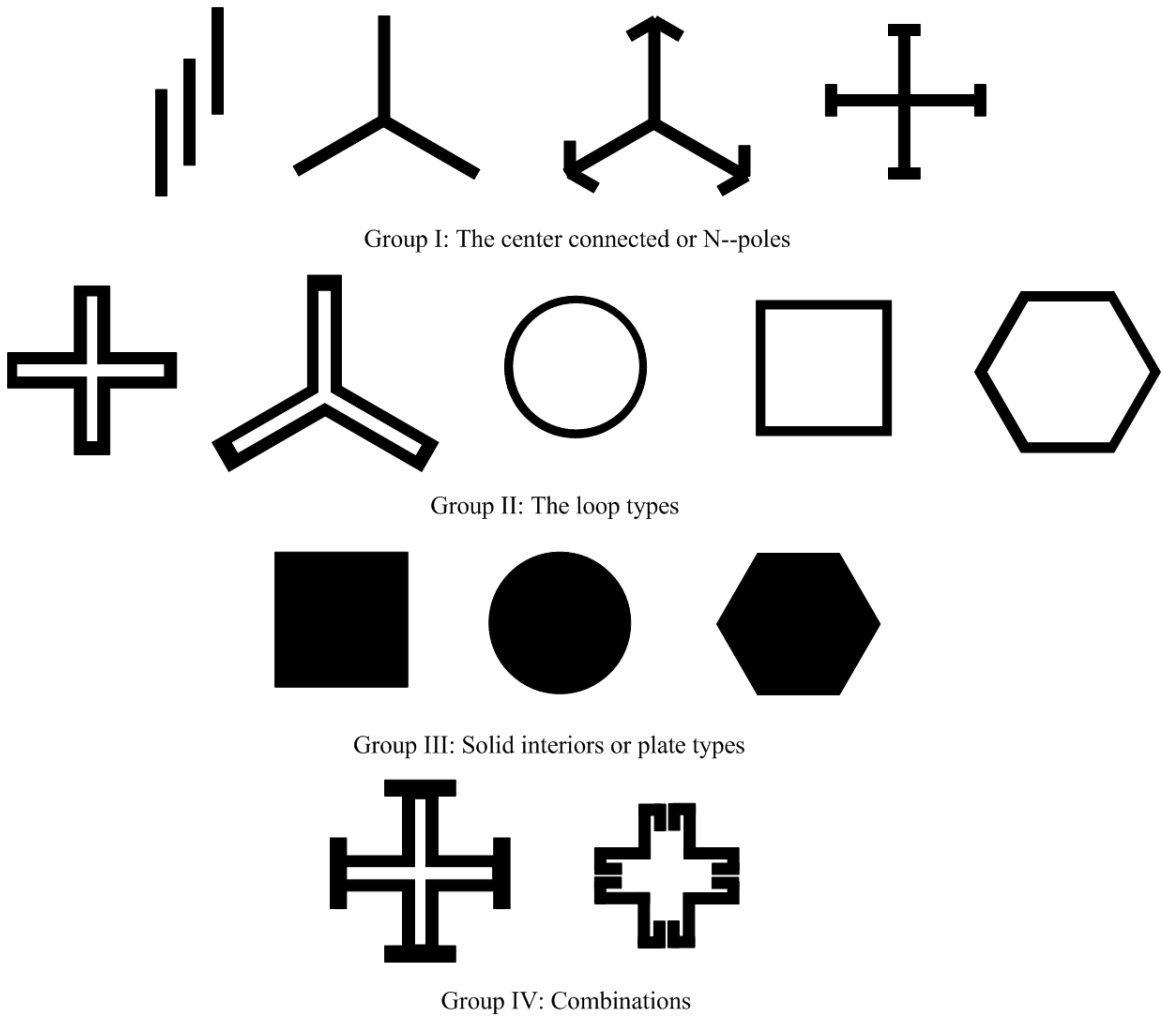

Figure 2.3: Typical FSS Elements classified in four major groups based on their shapes [1].

2.2.1 Class I: Center Connected or N-Pole Elements

Tripole Array

The first example of the class I of traditional FSS is an array of tripoles. As shown in the first row of Fig. 2.3, the tripole element consists of three concentric, thin monopoles which share a common point (the center). Although being large, the tripoles can be packed tightly to reduce the inter-element spacing, and therefore, enhance the bandwidth. Fig. 2.4 shows the calculated reflectivity for closely spaced tripoles in an infinite array on $x - z$ plane. As can be seen, the FSS plane is sandwiched between two dielectric substrates. D_x and D_z in this figure represent the array periodicity along $\hat{x}$ and $\hat{z}$ directions, respectively. Other parameters of the FSS can be found in Fig. 2.4 as well, including the gap between wires and

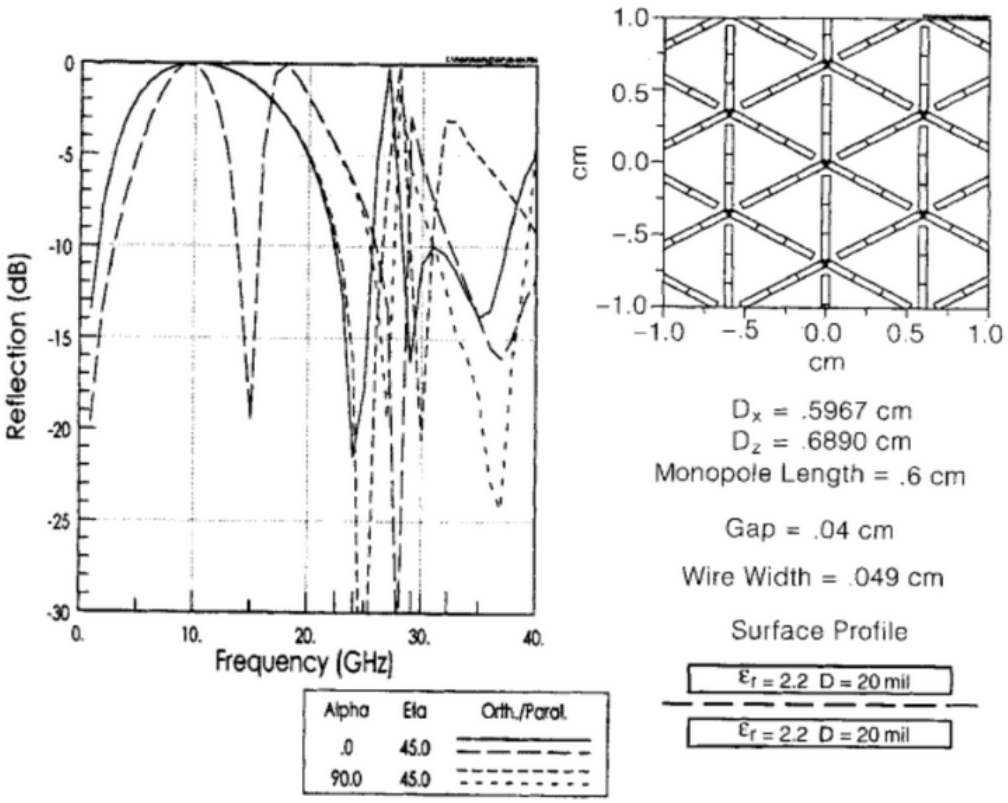

Figure 2.4: Tripole FSS- Simulation results for the reflection coefficient of an array of tripoles. The design frequency is 10 GHz (picture courtesy of Munk's book on FSS, [1]).

the wire width. Based on the simulations, this 10-GHz FSS has its first harmonic at around 27 GHz. The results also show a moderately high dependence on the incidence angle.

Jerusalem Cross

The Jerusalem cross is one of the oldest building-blocks (see the first row in Fig. 2.3) in design of FSS. It consists of two crossing dipoles which are loaded with small, orthogonal sections at their ends. The simulations results shown in Fig.2.5 exhibit a total reflection (first harmonic) at 10 GHz with a null at around 22 GHz which is followed by a second total reflectivity at about 35 GHz (second harmonic). In comparison with the tripole array (see Fig. 2.4), the Jerusalem FSS shows a better stability as the angle of incidence is changed from normal to 45^o, both in terms of response characteristics, i.e. bandwidth, and harmonics.

2.2.2 Class II: Loop Type Elements

Four-Legged Element

The second row of Fig. 2.3 contains the four-legged element. This element is made up of two meandered, half-wave dipoles. The operation mechanism of this element can be explained in a more classic fashion using the transmission line theory. The basic idea is that a half-wave dipole can be "similar" to a shorter dipole which is loaded with a reactance, Z_L. "Similar" here refers to the overall reactive impedance of the dipoles which has to be zero at the resonance. In other words, a reactance can compensate for the effect of the shorter length. It can be shown that the shorter dipole at the resonance frequency of the half-wave dipole is capacitive [6]. As a result, the load Z_L must be inductive so that the total impedance of the dipole becomes zero. To create an inductance, one just needs to short a small piece of transmission line [6]. This idea is illustrated through a circuit analogy of the dipole element in Fig.'s 2.6(a), (b), and (c).

In order to maintain the symmetry with respect to two orthogonal directions, the length of the meandered dipole along the two directions, l, must be equal. This length is, therefore, become a quarter of the dipole dimension, i.e. $l = \lambda/8$ (see Fig. 2.6(d)). This way the element becomes polarization insensitive. The final step is to place two such dipoles side by side and

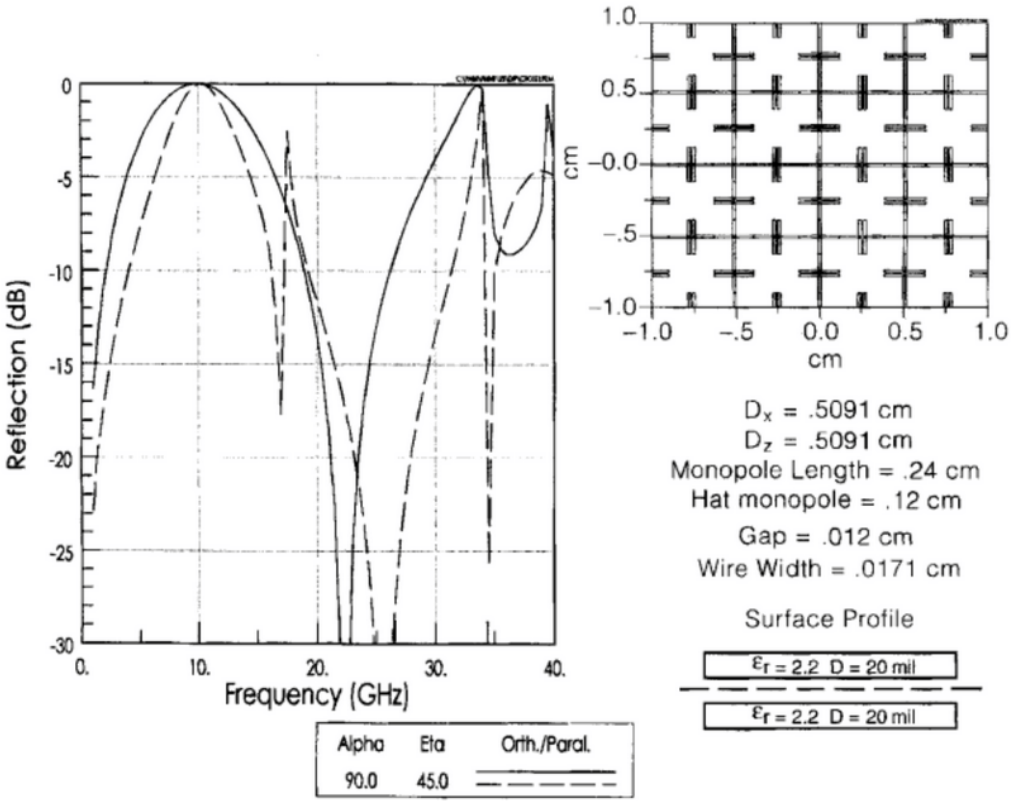

Figure 2.5: Jerusalem Cross FSS- Simulation results for the reflection coefficient of an array of Jerusalem crosses. The design frequency is 10 GHz (picture courtesy of Munk's book on FSS, [1]).

connect them. This is allowed as the corresponding end points from the individual dipoles have the same potential once placed side by side in the array. The result (Fig. 2.6(d)) is the the four-legged element. Fig. 2.7 shows a typical four-legged FSS simulated for different incidence angles. Similar to previous FSSs, the four-legged FSS has a harmonic close to the first resonance.

Hexagonal Element

This element is also shown in the second row in Fig. 2.3. Unlike previous elements, this FSS has a better harmonic performance. A typical design for operation at X-band is provided in Fig. 2.8. As shown, the first null in the reflection response occurs at 29 GHz,

thus pushing the second harmonic to frequencies higher than 40 GHz. This element also has a better scan stability. However, it should be mentioned that this particular example (Fig. 2.8) demonstrates an FSS with a relatively poor filtering response which has a wide bandwidth of about 25 GHz at the center frequency of 10 GHz. Apparently, achieving a narrower bandwidth requires the first null to come to lower frequencies, thus pushing the second harmonic down to lower frequencies close to the main resonance.

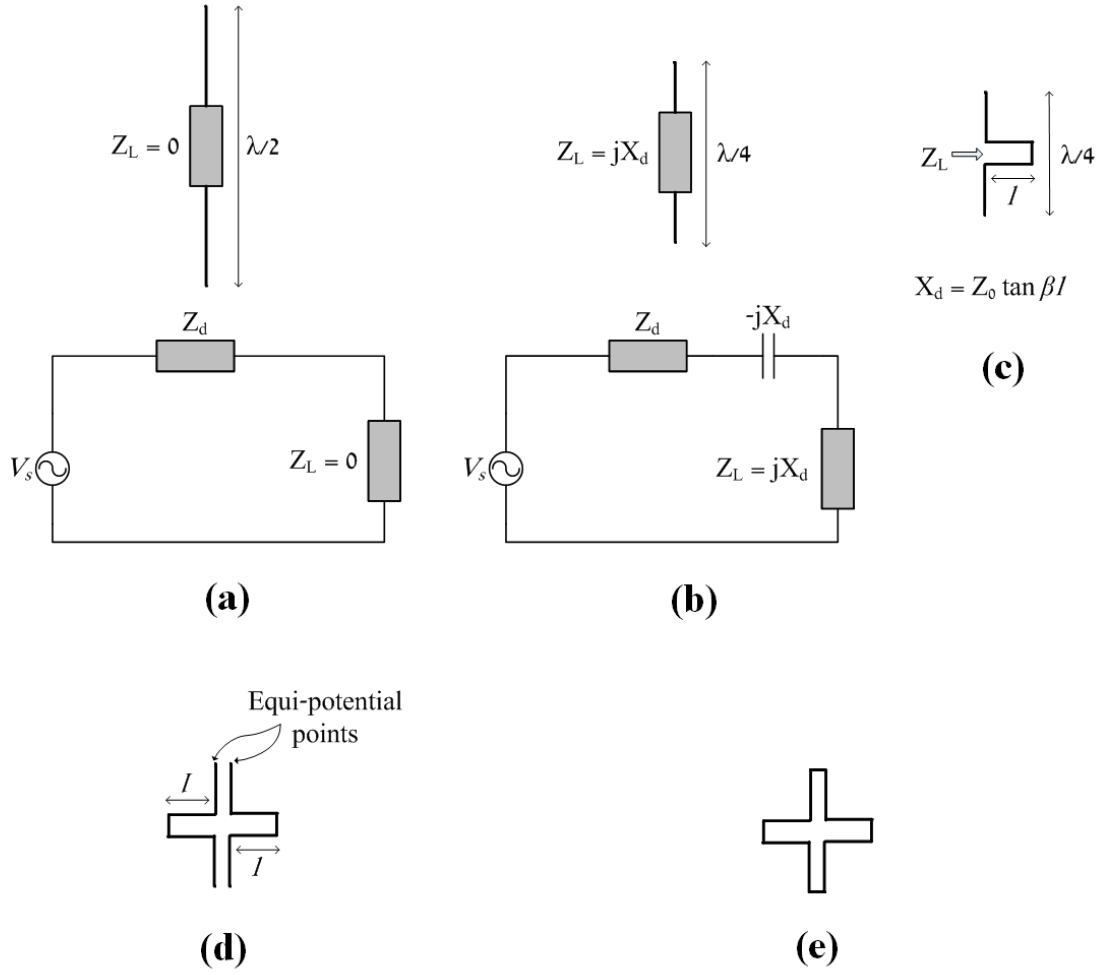

Figure 2.6: Development of the four-legged element- (a) shows a simple half-wave dipole with impedance Z_d which is shortened into a quarter-wave dipole with impedance $Z_d - jX_d$(b) that is loaded with an inductance formed (c) using a short transmission line. Next, two such dipoles are placed side by side (d) and finally are connected at the end points (e) [1].

2.2.3 Class III: Plate Type Elements

The third group on the list includes plate type FSS designs which are of two forms: 1) Array of metallic patches in the shape of a circular disk, square, rectangular, etc. 2) Array of slots on a metallic plate in the form of circular, square, etc. Fig. 2.9 shows the two sub-categories. The first type is usually used as reflecting arrays, whereas the second type is often transparent. This group of elements was actually among the first FSS structures that took attention of designers in the past. Since the patches (holes) dimensions must be close to $\lambda/2$ in this approach, such elements usually suffer from issues of angle dependence and early onset of grating lobes, and thus they are not too favorable for filter designs [1]. Munk closes the overview on this group of elements by quoting from Chen: "Shift of resonant frequency and changes of bandwidth in opposite sense for the perpendicular and the parallel polarizations as functions of incident angle limit many useful applications of this perforated

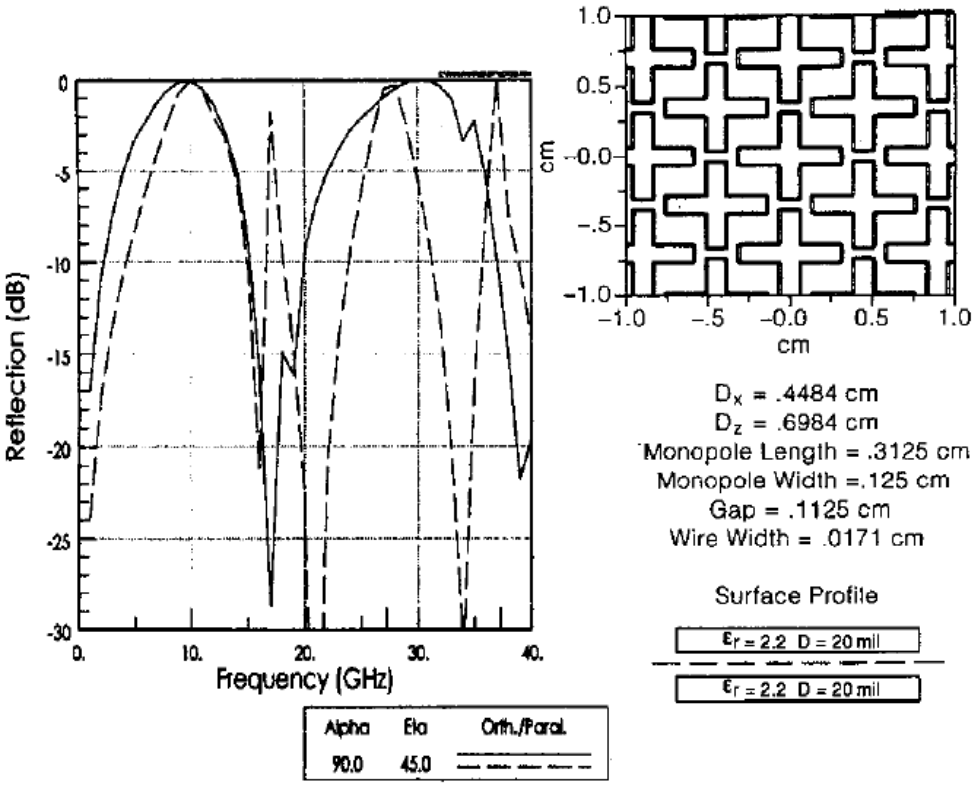

Figure 2.7: Four-Legged FSS- Simulation results for the reflection coefficient of an array of four-legged elements. The design frequency is 10 GHz (picture courtesy of Munk's book on FSS, [1]).

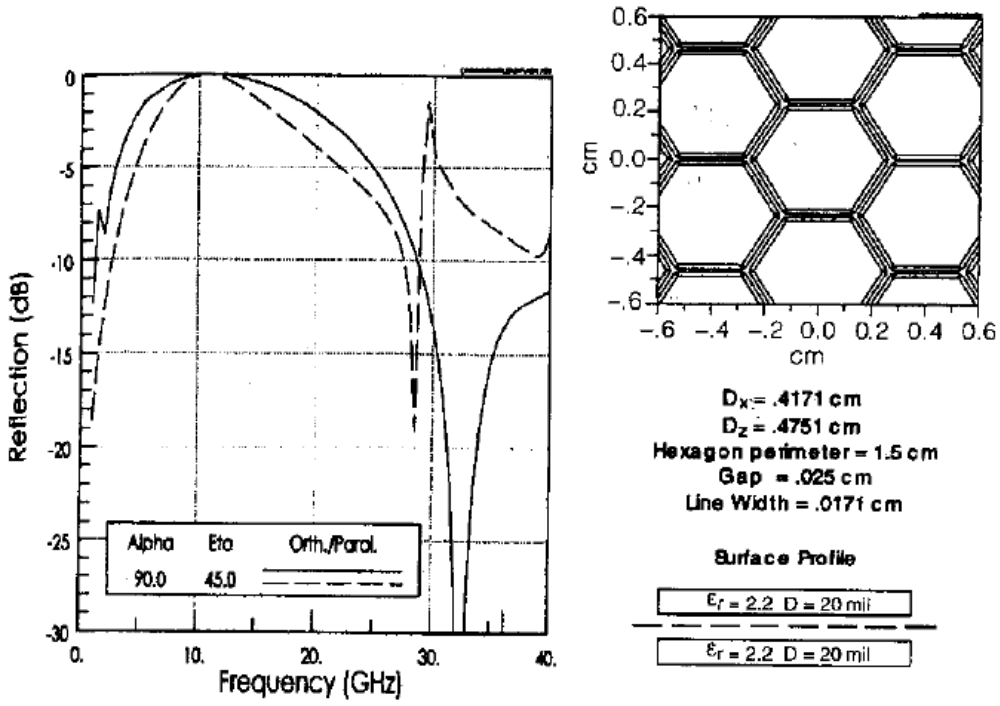

Figure 2.8: Hexagonal FSS- Simulation results for the reflection coefficient of an array of hexagons. The design frequency is 10 GHz (picture courtesy of Munk's book on FSS, [1]).

plate" [36]. As will be discussed in more detail in Chapter 3, such patch arrays can be adapted with the new miniaturized approach in order to perform better.

2.2.4 Class IV: Combination Elements

The groups introduced above include a broad range of elements. However, any combination of the elements belonging to any of these groups can also construct a new element, and this list is endless. These mixed elements comprise another group which Munk calls them combinations. An example of such combinations of the elements is shown in Fig. 2.10. This FSS is a combination of the four-legged element (Fig. 2.7) and the Jerusalem cross (Fig. 2.5).

2.2.5 Evaluation of the Classes of Frequency-Selective Surfaces

Although the ultimate application of the FSS determines the constraints of the design, there are certain features that are typically more important than others. Having being used

as spatial filters, FSS structures are expected to have a low dependence on the angle of incidence. This is perhaps the most important feature of interest in any design.

In order for the resonance frequency of an FSS to be more stable while the angle changes, a generally helpful approach is to keep the inter-element spacing small compared with the wavelength. A large spacing creates higher levels of grating lobes, thus pushing the resonance frequency downward with angle of incidence [1]. Given the set of examples of typical classes of frequency-selective surfaces presented above, a general comment can be made: In terms of angle stability, the leading group is the type II, the loop type FSSs [1]. Although the members of this group (three- and four-legged, square and circular loops, and etc.) may look different at first glance, their operation can be related to that of the dipole. For example, a square loop can be viewed as two bent dipoles (right-angle). As a result, the loop resonates when the two dipoles are at resonance, i.e. they are $\lambda/2$. This condition is satisfied when the circumference of the loop is one wavelength, λ. In other words, meandered, half-wave dipole is the basis for the elements of type II; however, since they can be packed in a smaller area, they show better scan performance.

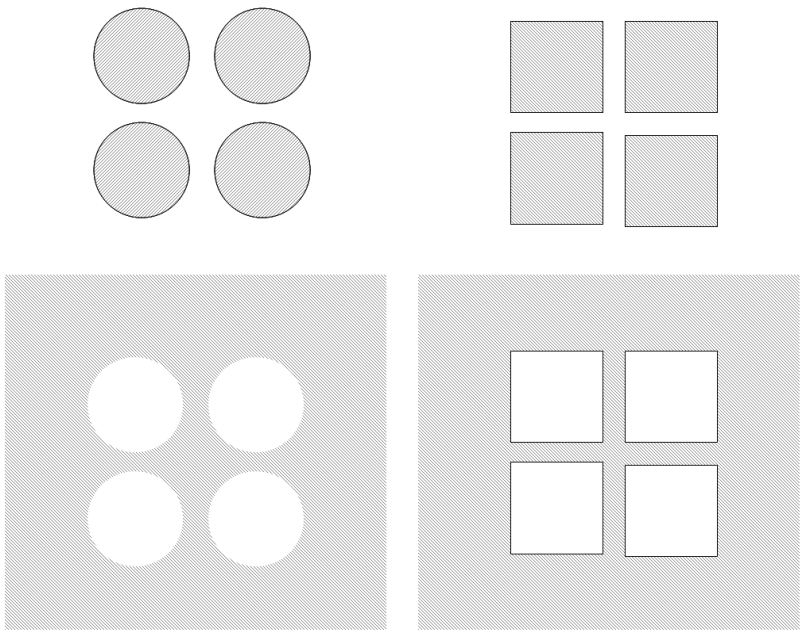

Figure 2.9: Examples of the third class of FSSs, the plate type elements [1].

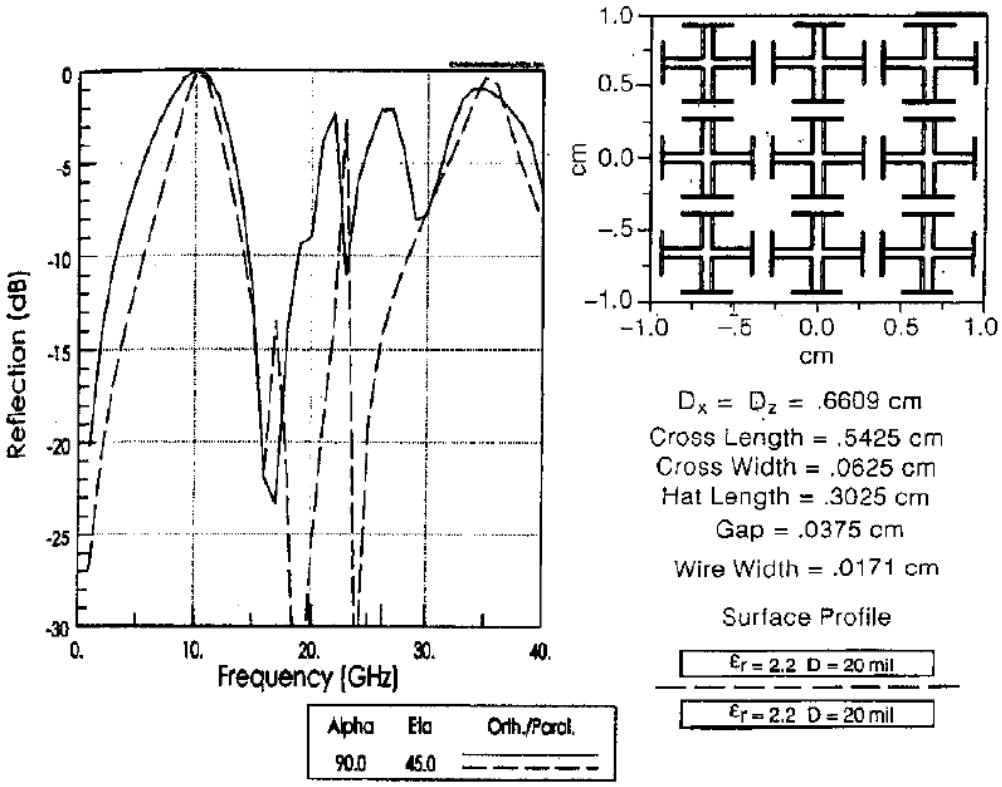

Figure 2.10: Examples of the fourth class of FSSs, the combinations elements. This FSS is a mixture of the the four-legged element and the Jerusalem cross. The design frequency is 10 GHz (picture courtesy of Munk's book on FSS, [1]).

2.3 Methods for Analysis and Characterization of Frequency-Selective Surfaces

An established approach to describe a frequency-selective layer is to use the scattering (S-) parameters [8]. An FSS structure, as a 2-D, planar array, divides the whole free-space into two regions: 1) a half-space that includes a known electromagnetic source, and 2) the other half of the space. In order to solve for the wave propagation everywhere in the space, one needs to account for the effects of the FSS, i.e. the transmission of the wave through the FSS and the reflection of the energy off the FSS plane. Given the reflection and transmission characteristics of the FSS, on the other hand, one can fully describe the interaction of the source and the FSS. As a result, reflectivity (S_{11}) and transmissivity (S_{21}) are the only

parameters needed for characterization of an FSS given that frequency-selective surfaces are typically reciprocal structures.

Numerical analyses of FSS problems are done using various techniques [14, 19, 23, 29, 36, 78, 84]. The problem setup assumes that the FSS is a planar, doubly-periodic structure with an infinite extent. These assumptions together with the uniformity of the excitation (a plane-wave with a uniform amplitude profile) are used to simplify the analysis of such an infinite size problem. Given the symmetries of the problem, the simulation domain is reduced to a single unit cell. This simulation setup becomes complete by applying appropriate boundary conditions around the unit cell in order to account for the symmetries of the planar, periodic FSS. This approach is valid since all the elements of the infinite array are the same; moreover, the excitation is the same for different elements. Depending on the direction of illumination (incidence angle), the phase of the incident wave may vary from element to element. The phase variations, however, are linear along the elements and can be easily included in the boundary conditions.

An FSS problem is usually formulated based on an integral equation approach describing the the unit cell. Next, the formulation is modified so that the effects of the periodic arrangement of the cells (symmetry) is included in the solution. This is done by application of the Floquet's theorem to the formulation such that the continuous convolution integral is converted to an infinite summation with each summand being a product of the spectral Green's function and the spectral equivalent surface current [2].

As mentioned above, these formulations assume that a given FSS is an infinitely large, planar, doubly-periodic array. In practice, however, an FSS not only has finite dimensions but also might have arbitrary, local curvatures. As a result, the symmetry assumptions are no longer valid as the interaction (incidence angle) of the wave with the individual elements of the surface is different. Thus, an exact analysis of such an arbitrary surface requires finding the current distribution over the entire surface. Since the surface usually has a large number of elements, the number of unknowns needed to formulate and the scattering problem becomes very large. More discussion on these issues and available approximate methods for circumventing them can be found in the references provided above.

Transmission and reflection characteristics of FSS screens can be measured through a few

methods [78–81]. To measure the transmissivity, the FSS under test is placed between two directive antennas, one as the transmitter of the signal and the other acting as the receiver. While blocking the direct path of propagation, the FSS filters the frequency content of the radiated wave from the transmitter, thus leaving its signature on the received power by the receiver. In this setup, the antennas are fixed and facing one another, while the FSS plane can be rotated. For oblique incidence measurements, the FSS holder fixture is rotated up to the angle of interest such that the FSS remains between the two antennas. As for the calibration, the FSS is removed and the power transfer from the transmitter to the receiver is measured as the reference value for the transmissivity (thru calibration). This setup should be also able to measure the reflection characteristics of the FSS.

The measurement setup consisting of two standard horn antennas and a vector network

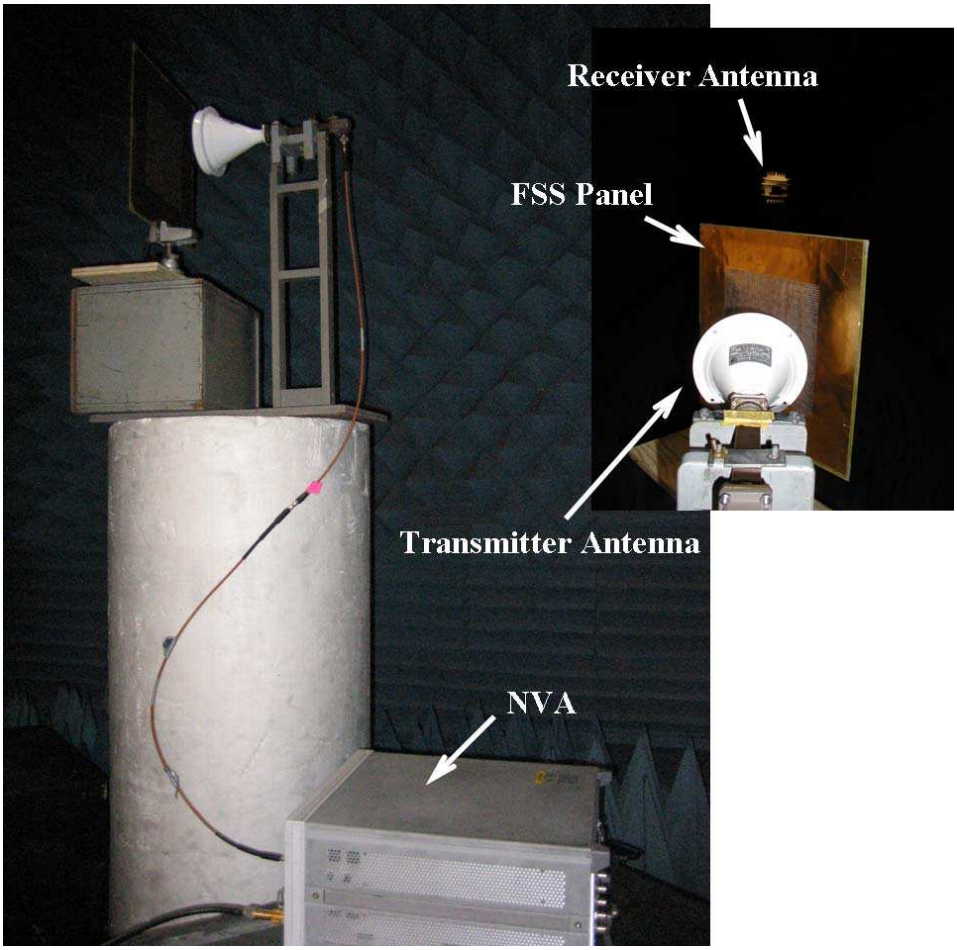

Figure 2.11: FSS transmission measurement setup in the anechoic chamber [2].

analyzer (VNA) is demonstrated in Fig. 2.11. The experiments are performed in an anechoic chamber which simulates the free-space environment. Although common, this method might not be able to accurately measure the FSS characteristics. Especially, in the reflectivity measurement, the reflected signal might be dominated by undesired scattering. Given the finite size of the FSS and its distance to the antennas, diffraction from the edges of the FSS test panel may become so strong that it shadows the actual reflected signal. The large beamwidth of the horn antennas also increases the edge scattering.

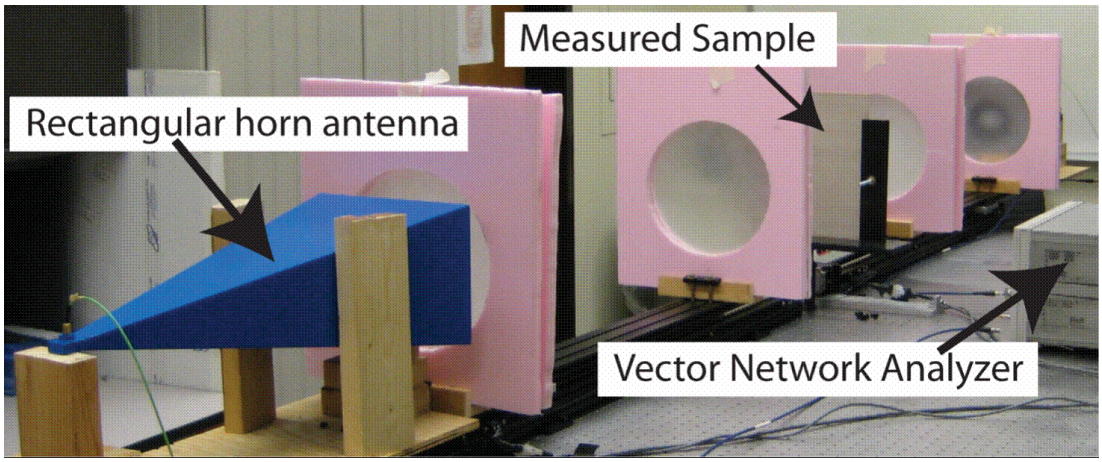

Figure 2.12: Application of lens-corrected horn antennas for precision FSS transmission measurement [80] (Picture courtesy of Mr. S. Rudolph, Radiation Lab, The University of Michigan).

To circumvent the issues of edge diffraction, the precision setup shown in Fig. 2.12 is employed [80,81]. This setup uses lens-corrected horn antennas in order to excite the FSS under test with a collimated beam. This setup also allows for the scan performance measurement with a large, off-normal angle.

An alternative measurement technique is performed in a waveguide environment to emulate an infinitely large FSS operating in a free-space environment [2]. This method was originally proposed for testing the impedance matching of phased-array antennas [79]. For this experiment, the sample (FSS) under test must fit appropriately within the waveguide flanges so that the waveguide metallic walls do not change the actual periodicity of the

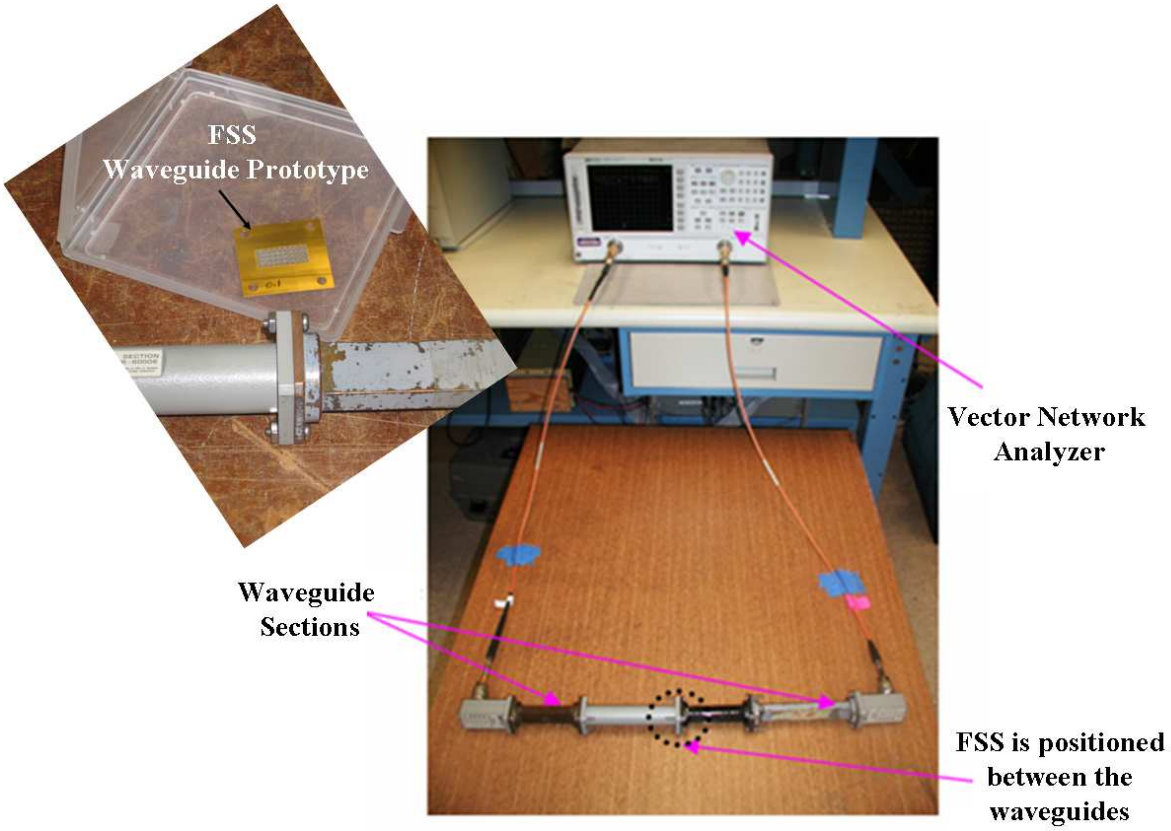

Figure 2.13: FSS measurement setup in the waveguide environment [79].

periodic FSS [82]. This will be discussed in more detail in Section 3.3.4 of the next chapter.

The waveguide measurement arrangement is demonstrated in Fig. 2.13. Although avoiding the effects of undesired diffractions, this measurement method is frequency-dependent since the wave-number of the propagating wave inside the waveguide changes with the frequency. Consequently, the incidence angle at which the wave hits the FSS changes as the frequency varies. As a result, the waveguide setup may be more suitable for single-frequency tests. Moreover, this setup is limited to TE modes for the test excitations [2].

2.4 Traditional Applications of Frequency-Selective Surfaces

Common electromagnetic design problems that can benefit from frequency-selective surfaces is presented here. As briefly discussed in Chapter 1, conventional applications include radomes (bandpass spatial filters) and multi-frequency reflector antennas. Because of their frequency-dependent behavior, FSSs have also been looked at as reactive surfaces and been used in a variety of beamforming applications as well as high-performance antenna designs. In this section, some of the current applications are presented.

2.4.1 Radomes

Frequency-selective surfaces have been employed primarily in design of special covers called radomes that are capable of reducing the radar cross-section (RCS) of antennas under cover. In this application, FSS is transparent to a desired frequency band and reflecting at other frequencies.

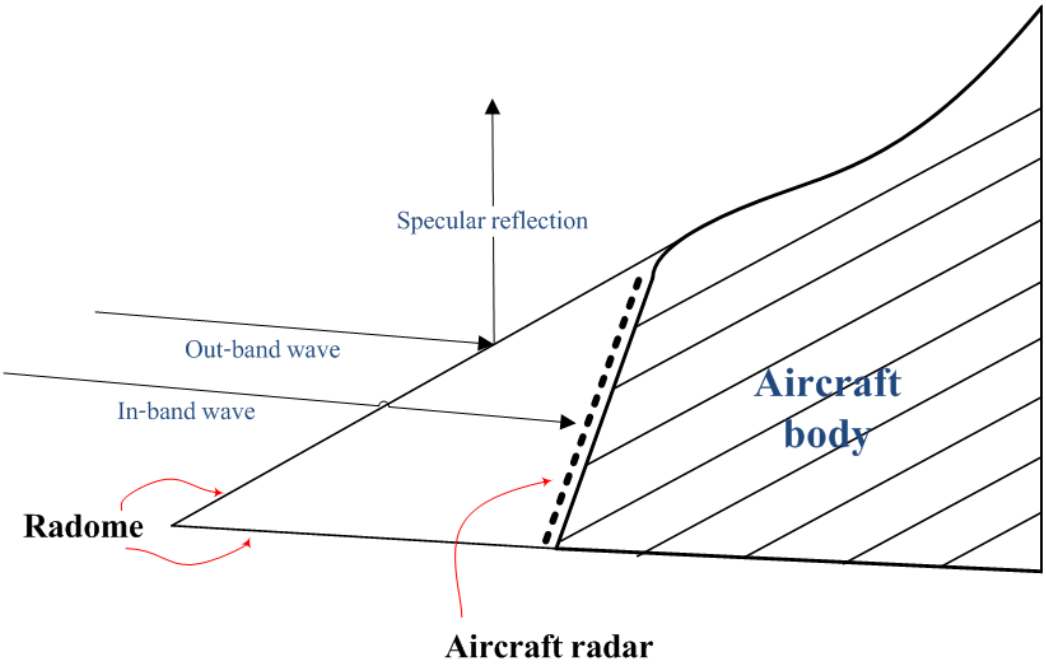

Figure 2.14: Application of frequency-selective surfaces as radome covers in the aircraft technology for reducing the antenna RCS [1].

In practice, bandpass, spatial covers of this type are used in certain applications, for example, in the case of an aircraft. A typical assembly is shown in Fig. 2.14. As shown, the radar (antenna) mounted at the front tip of the airplane is covered by a shaped radome. Radome has two modes of operation: In the transparent mode the signal passes through the radome and is collected by the antenna. In the reflecting mode, however, the radome behaves like a metallic surface which reflects the signal in the specular direction. The advantage of this method is that the radome can be shaped particularly in order to reach the lowest levels of RCS. This can be done by designing the shape of the radome so that the direction of the strong reflection (specular) in reflecting mode is out of the sight of the transmitter of the signal, i.e. it is not directed toward the incoming signal.

2.4.2 Multi-Frequency Reflectors

As mentioned earlier in Chapter 1, frequency-selective surfaces have been utilized in multiband reflector antenna applications [39, 40, 43, 48]. A common approach uses an FSS as a subreflector in addition to the large reflecting dish in a reflector antenna, as shown in Fig. 2.15. The subreflector, which is an FSS, is designed to be reflective at a frequency band and be simultaneously transparent at another desired band. The frequency-dependent subreflector allows for application of multiple feeds in this systems, thus enabling the multi-frequency state of the antenna. Different frequency feeds are optimized and positioned at the real and virtual foci of the subreflector. Hence, only one main reflector can act as a multiband antenna.

A practical application of this idea is the high-gain antenna (HGA) of the Voyager spacecraft which was designed, [39], to diplex S and X bands. An FSS forms the subreflector which is reflecting at X-band whereas is transmitting at S-band. In this antenna, the S-band feed is placed at the prime focus of the reflector, whereas the X-band feed is located at the Cassegrain focal point (see Fig. 2.15). As a result, loaded with an FSS, a single reflector acts as a dual-band antenna, thus reducing the overall mass, volume, and most importantly the fabrication cost. A similar approach was proposed later by Wu to build a four-band reflector system. In this work, a four-frequency FSS was utilized as the subreflector [49].

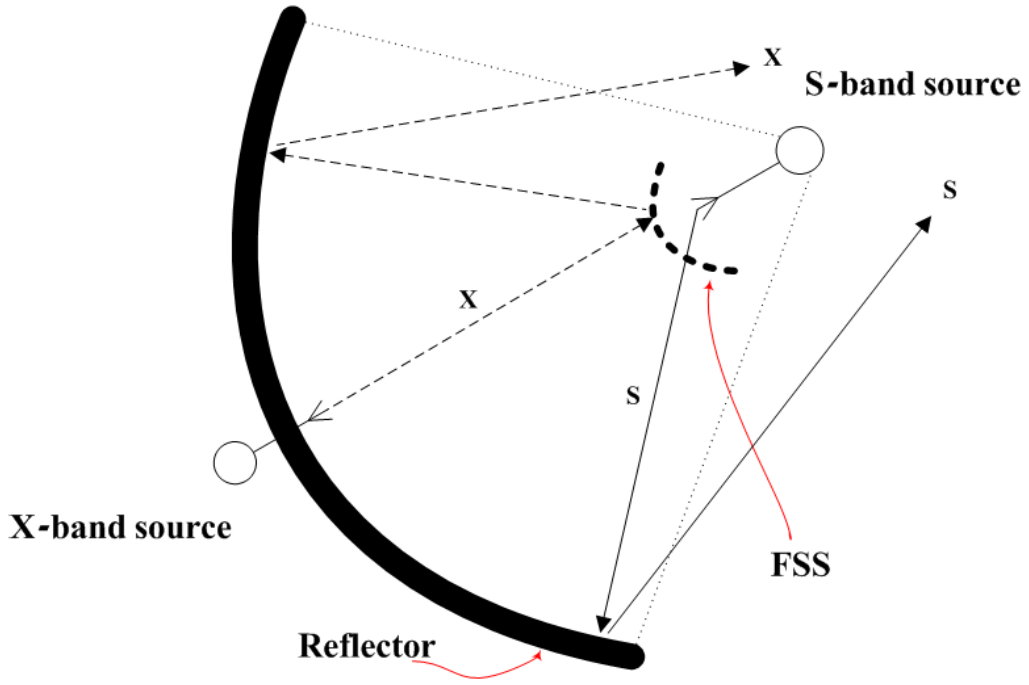

Figure 2.15: Dual-frequency reflector antenna using an FSS as the subreflector [2].

2.4.3 Beam Control Arrays

Frequency-selective surfaces have also been used in creation of impedance surfaces with tuning capability. This problem is believed by Wu, [2], that first appeared in [50] where scattering properties of a corrugated surface loaded with microwave solid-state amplifiers were studied. In this surface, connecting each slot region to an amplifier, the authors of [50] have been able to not only control the phase of the reflected wave but also to manipulate its power gain. It was envisioned that this loaded array would be able to change the phase front (shape) and intensity of an incident plane-wave.

FSSs considered for the beam-shaping application are commonly of the type series resonators, $L-C$ [51, 52]. A possible way for constructing an $L-C$ resonating surface is to use an array of metallic strips that are cut at periodic intervals in order to create capacitive junctions along the strips. This array, which is simply an array of small strips, is shown in Fig. 2.16. The basic idea can be explained using a quasi-optical approach in which the beam is assumed to be a plane-wave over an infinitely long, periodic array in two dimensions on the

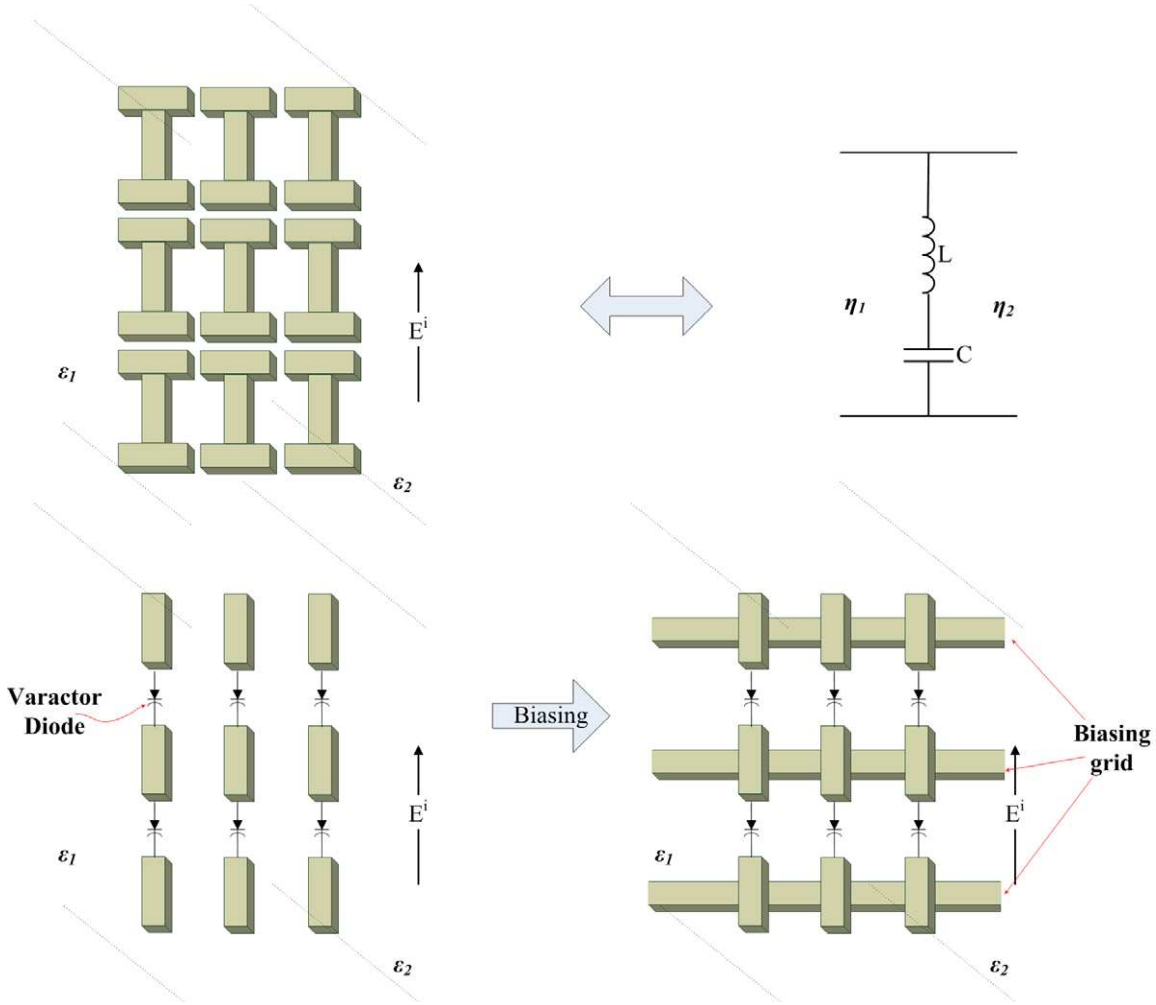

Figure 2.16: An active $L-C$ array comprising metallic strips interrupted by gaps in a periodic fashion. The gaps further are loaded with varactor diodes to alter the gap capacitance [2].

surface. The metallic traces are inductive which together with the gap capacitances create a series combination of inductors with capacitors. By mounting lumped reactive elements such as varactors diodes, one can tune the resonance characteristics of the array. It should be pointed out that this is only an approximate method since if the elements of the array are long, the wave variations along the elements must be taken into account. Nevertheless, this approach builds up a good understanding on the behavior of active arrays.

Two modes of operation can be specified: 1) Transmission mode (shown in Fig. 2.17(a)) for controlling the beam amplitude, and 2) reflection mode (shown in Fig. 2.17(b)) for changing the beam phase. As shown in Fig. 2.17(b), in the reflection mode, the array is backed by a metallic surface to assure the total reflection.

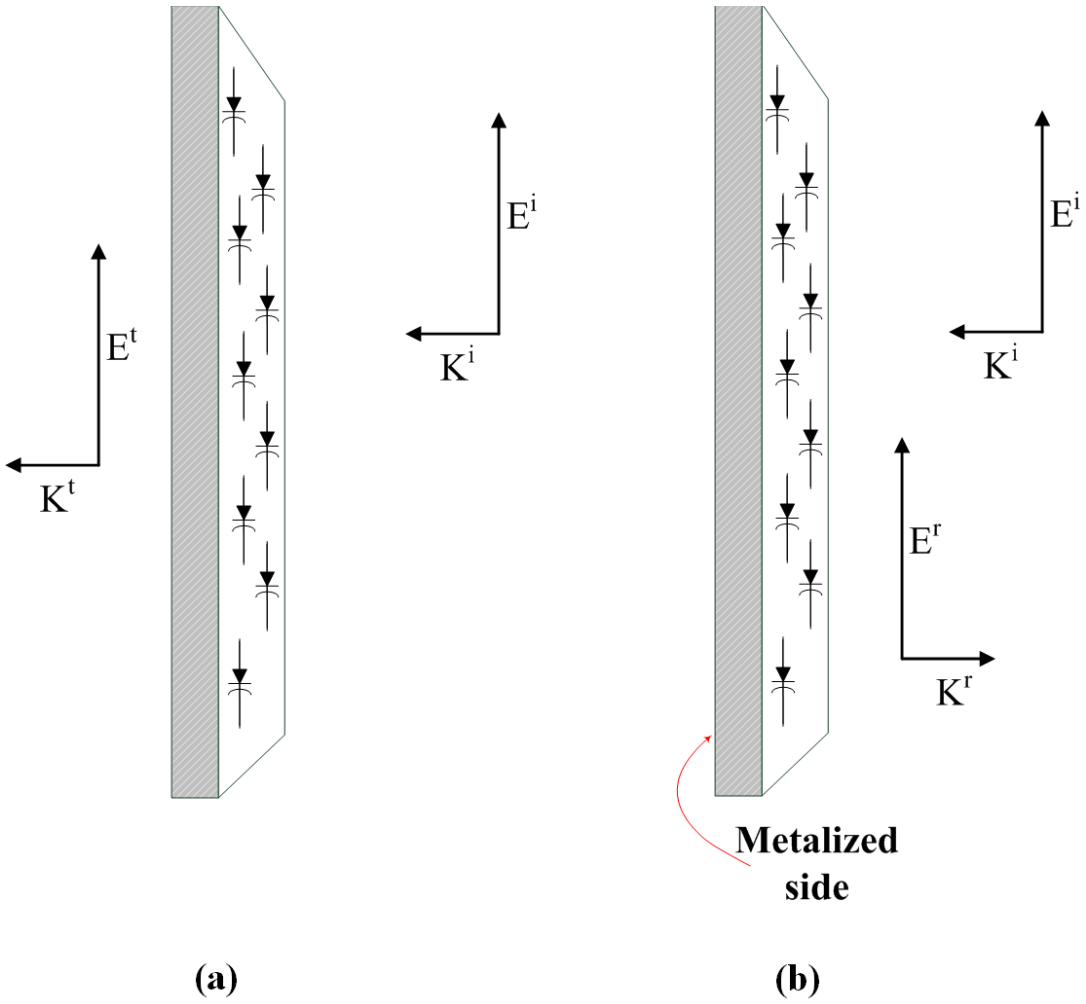

Figure 2.17: Modes of operation for an active $L-C$ array. (a) Transmission mode for adjusting the wave intensity. (b) Reflection mode for changing the phase [2].

The first experimental version of $L-C$ active arrays in reflection mode was demonstrated in [53]. This reflective array was designed to work at 93 GHz and was able to produce a 70^o phase shift with about 6.5 dB loss. This research was further expanded and lead to demonstration of more involved active arrays such as multiplier arrays, oscillator arrays, and amplifier arrays.

Transmission mode operation has also been tested and demonstrated. In [54] an array of PIN diodes is proposed for beam switching. In another attempt, Schottky diodes were used in an array format to manipulate the transmissivity of the array [55]. Experimental follow-up of these methods were later appeared in [56] and [57], respectively.

2.5 Chapter Conclusions

A numerical, comparative study over the conventional elements in design of frequency-selective surfaces is presented in this chapter. Traditional surfaces are categorized based on their geometries, [1], into four major groups: I) The center connected or N-poles, such as dipole, three-legged element, the Jerusalem cross, and the square spiral. II) The loop types such as the three- and four-legged loaded elements, the circular loops, and the square and hexagonal loops. III) Solid interiors or plate types. IV) Combinations which are a mixer of previous groups. Through a physical discussion, it is shown that the operation mechanism of the traditional FSS is dependent on the structural-based resonances. Methods of characterization and numerical simulations are discussed briefly next. The overview study of this section is followed by introducing some of the conventional applications involving frequency-selective surfaces, demonstrating the versatility of these surfaces in microwave engineering.

CHAPTER 3

Metamaterial-Based Miniaturized-Element Frequency-Selective Surfaces

This chapter presents a new approach to the design of surfaces with a controllable, spatial filtering characteristic. These "miniaturized surfaces" are capable of performing functions similar to traditional frequency-selective surfaces discussed in Chapter 2. However, the new surfaces operate based on different principles which allow for functionality superior to that of the traditional surfaces. As a result, their applicability extends beyond that of traditional surfaces into a variety of compact communications applications. A detailed description of the new approach is provided in this chapter.

3.1 Chapter Introduction

Traditional frequency-selective surface (FSS) structures, with resonant unit cells, have been investigated over the years for a variety of applications. These include bandpass and bandstop spatial filters, absorbers, and artificial electromagnetic bandgap materials. A typical FSS is a 2-D planar structure consisting of one or more metallic patterns, each backed by a dielectric substrate. These structures are usually arranged in a periodic fashion; therefore, their frequency response is entirely determined by the geometry of the structure in one period called a unit cell. As a result of research on the applications mentioned above, the behavior of FSSs is well understood [1–3]. The focus of the past studies, however, has been mostly on the bandstop characteristics produced by these surfaces, and structures with bandpass

characteristics have been rarely studied.

Recently, there has been an interest in design of FSS with unit cell dimensions much smaller than a wavelength. In traditional designs, the frequency-selective properties result from mutual interactions of the unit cells. Therefore, to observe a desired frequency selective behavior, a large number of unit cells must be present. Consequently, the overall size of the surface is electrically large. On the other hand, for some applications where a low sensitivity with respect to the incidence angle of the exciting wave is required or in cases where a uniform phase front is difficult to establish, the screen size needs to be small. To address this problem, a new class of FSSs called miniaturized-element frequency-selective surfaces was developed [37]. The new class takes an approach which is different from those of the past designs. In this approach, instead of using a resonant structure as the building block of the frequency selective surface, special unit cells of small dimensions are used. These unit cells act as lumped inductive and capacitive elements and are properly arranged so they couple to the magnetic and electric fields of an incident wave, respectively.

This chapter presents a new miniaturized-element FSS architecture with unit cell dimensions as small as $\lambda/12$ [38]. Due to the sub-wavelength size of its elements, this spatial filter is called a metamaterial-based FSS. Metamaterial is a term used to describe artificial materials comprised of very small inclusions ($< \lambda/10$) in a homogenous medium. Metamaterials produce effects not observed in natural materials. The new miniaturized-element FSS exhibits a high-Q, high-order, bandpass characteristic which can be potentially tuned using varactors mounted on one layer of the structure. A detailed design procedure for the proposed design is presented using an equivalent circuit model whose parameters are extracted from full-wave analysis. This model is used to design a prototype at X-band, with unit cell dimensions of 4 mm $\times$ 4 mm, which is fabricated and tested using a free-space measurement setup to show the validity of the design procedure and the performance of the new design.

3.2 Background

3.2.1 Physics: Elements of Design

A new perspective on the design of frequency-selective materials is presented in this chapter. Through circuit analogy, the fundamentals of design of FSS using the new approach are described. As mentioned in the first chapter, frequency-selective surfaces are spatial filters which are excited by a plane-wave impinging on the surface. Design of a filter in microwave engineering generally includes three steps; 1) deciding on the order of the filter, i.e., the number of resonators needed in the filter; 2) building the resonators and; 3) controlling the mutual interactions (coupling) between the resonators in order to tailor a particular frequency response. Similar steps are taken in design of miniaturized FSSs. For implementing the actual surface, however, first we need to learn how to create the resonators in two-dimensional space on a substrate. To produce a resonant characteristic, both inductive and capacitive effects are required. As a result, finding methods of implementing spatial inductors and spatial capacitors is discussed first.

In order to arrive at configurations that produce a certain reactive behavior, we need to review the fundamentals of operation of a capacitor and also an inductor. According to the electrostatic theory, two conductive objects connected to different dc voltages construct a capacitor for storing electric energy. This energy is present in the electric field whose contours start from one of the objects and land on the other one. Conversely, if we somehow establish an electric field between two conductors, then we have created a capacitor. Fig. 3.1(a) shows the capacitor built between two adjacent metallic patches. The capacitance is proportional to size of the overlapping areas and is inversely proportional to the separation of the patches.

An electric current flowing on a wire, on the other hand, shows inductive effects according to electrodynamic theory. A magnetic field is generated as a result of the moving charges, which, in turn, stores magnetic energy (inductance concept). Similarly, placing the wire in a time-varying magnetic field which has a component perpendicular to the wire on the wire plane produces an electric current along the wire (inductor). This is shown in Fig. 3.1(b). By thinning the wire, the inductance increases.

The basic ideas outlined above were used in the past to construct planar structures

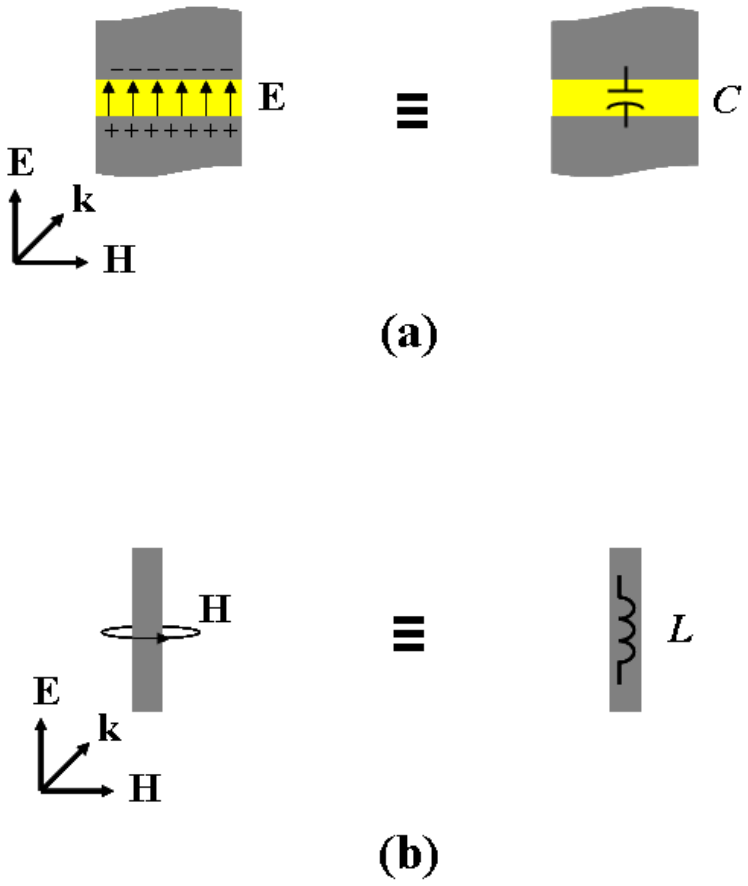

Figure 3.1: Construction of miniaturized capacitive junctions and inductive traces- (a) shows a capacitor formed between two metallic traces because of the electric field established between them; (b) shows the inductive behavior of a wire perpendicular to the magnetic field of the exciting wave.

with the ability to create reactive effects in response to an incident plane-wave. Periodic surfaces with capacitive and inductive characteristics have been investigated and reported previously [1,2]. As mentioned in chapter 1 (see Fig. 1.5), a periodic patch-array is known for producing a capacitive response over a designed frequency band. A wire-grid, on the other hand, is inductive. The brief physical discussion provided above can be used to explain such effects. Interpretation of the reactive arrays is given in Fig. 3.2.

There are approximate analytical solutions for the reactance value of periodic structures described above [5]. Consider an array of metallic, square patches with side length of l and

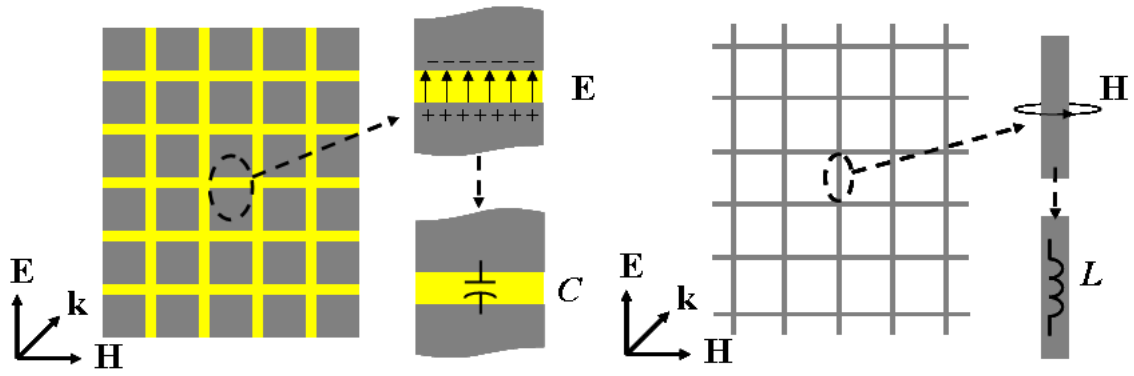

Figure 3.2: Upon incidence of a plane-wave on patch-array, the electric field creates positive and negative charges on the edges of the two adjacent patches, thus producing a gap capacitor. Similarly, in a wire-grid, parallel wires that are normal to the magnetic field act as inductors.

a separation width of s in two dimensions. Given the infinite, periodic arrangement of the patches, the frequency response of the array can be described by just analyzing one unit cell. Here, the term unit cell refers to one period of the surface. Similar approach calculates the approximate inductance associated with a 2-D wire-grid with periodicity of p and wire width of w. The first-order approximation of the capacitance of the patch-array and the inductance of a wire-gird are given, [5], respectively, by:

$$C = \epsilon_0 \epsilon_{eff} (2l/\pi) \log \left[\csc(\pi s/2l)\right] \tag{3.1}$$

$$L = \mu_0 (p/2\pi) \log \left[\csc(\pi w/2p)\right] \tag{3.2}$$

; where ϵ_0 is the permittivity constant of the air (free-space), and ϵ_{eff} is the effective dielectric constant of the substrate. μ_0 is the permeability of air.

The miniaturized approach starts with constructing the reactive elements and then combining them in order to produce the required resonances for filtering. The elements of the FSS are designed such that they act no longer as stand-alone resonant elements. Instead, each element in the array is used to create miniaturized, lumped capacitors (junction capacitors) and inductors (metallic traces). Such interactions can be explained through a quasi-static approach. In the next section, an FSS based on this approach is discussed.

3.2.2 The First Miniaturized-Element Frequency-Selective Surface: A Patch-Wire Design

The first generation of the miniaturized-element FSSs (the patch-wire FSS) was introduced in [37]. This miniaturized FSS is described here. Fig. 3.3(a) shows the patch-wire FSS which is a single-substrate surface comprising periodic patches and a wire-grid, printed on

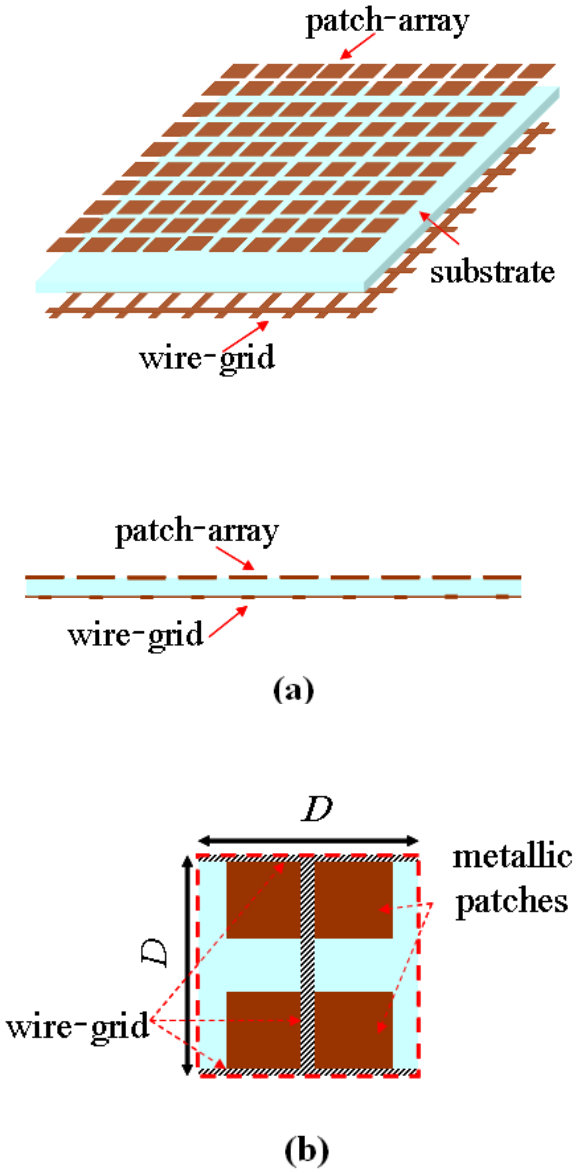

Figure 3.3: The patch-wire miniaturized-element FSS- (a) shows the geometry of the FSS in free-space comprising a patch-array and a wire-gird; (b) presents the FSS's unit cell.

either side of the substrate, with a unit cell (Fig. 3.3(b)) dimension of $\lambda/5$. This arrangement constitutes a parallel LC circuit based on the brief physical discussion presented above. An equivalent circuit model of the FSS is shown in Fig. 3.4. In this circuit, the capacitor models the patch-array, and the inductor represents the wire. There are three pieces of transmission line in this model; the short piece in the middle ($Z_1 = Z_0/\sqrt{\epsilon_r}$) models the substrate, while the other transmission lines correspond with the two half-spaces on either side of the FSS ($Z_0 = 377\ \Omega$).

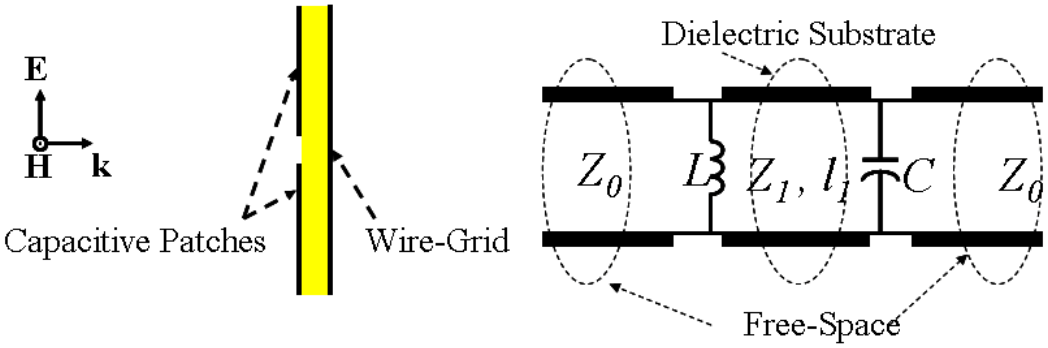

Figure 3.4: The patch-wire miniaturized-element FSS- Lumped equivalent circuit model consisting of a capacitor modeling the patches and an inductor behaving as the wire-grid.

This FSS can produce a single-pole, bandpass filter response given the circuit model. The bandpass behavior has been also verified by optimizing the unit cell parameters using a full-wave simulator. In the optimization, the unit cell size was fixed while other parameters were changing. The design parameters include: D as the periodicity of the FSS; w as the wire width; the gap width between the patches shown by s; and t representing the substrate thickness. A typical response of the single-substrate FSS is shown in Fig. 3.5 for the parameter values listed in Table 3.1. The simulations were performed for a number of incidence angles. As shown, the response shows a slight dependence on the angle.

Due to a high external coupling coefficient, it has been shown that such a single-pole design has a poor selectivity and a high insertion loss. To remedy this shortcoming, two such surfaces are coupled using an impedance inverter to obtain a high-Q, two-pole filter response with a very low insertion loss. Although the performance of this design is high, its fabrication is cumbersome as it requires two substrates (four printed faces) and a spacer

Table 3.1: The Design Parameters of the Patch-Wire Miniaturized-Element FSS in Free-Space

Parameter	w	s	t	ε_r
	1 mm	0.5 mm	0.5 mm	3.4

(quarter-wave impedance converter). Moreover, the overall FSS is quite thick ($\approx \lambda/4$) which might not be practical for some applications. The large thickness also degrades the scan performance. Nevertheless, the patch-wire FSS introduced a new perspective in FSS design. The waveguide measurements of the FSS proves the validity of the new approach and the improved performance of the new FSS compared to the old surfaces.

The miniaturized approach in design of FSS offers much more improvement in the performance, as will be presented in the next section. This is achieved by designing FSS elements having higher-order interactions (coupling) with the incident wave.

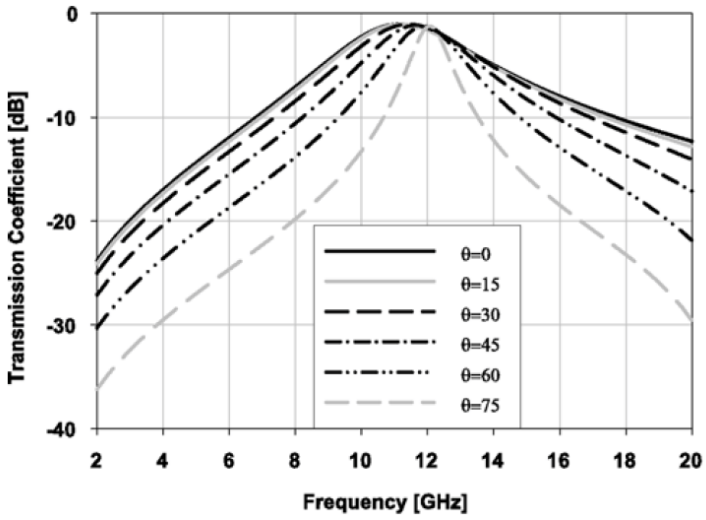

Figure 3.5: The patch-wire miniaturized-element FSS- Full-wave simulations were performed for a number of incidence angles to test the scan performance of the FSS (Picture courtesy of K. Sarabandi, et. al [37]).

3.3 The Loop-Wire Miniaturized-Element Frequency-Selective Surface

In addition to presenting a new methodology in design of FSS (based on the filter theory), the main message of the miniaturized approach is that by shrinking the unit cell dimensions, a better homogeneity in terms of filtering characteristics over the surface is achieved. In other words, the selectivity becomes inherent in the surface. The new feature, therefore, is a localized frequency selectivity. The miniaturization of the elements of the FSS, however, is limited by the fabrication process. Depending on the process and the material used, the width of the metallic traces and also their spacing cannot be smaller than a prescribed dimension. In this section, a new miniaturized-element frequency-selective surface is presented.

The new frequency-selective surface is made up of a 2-D, periodic array of metallic loops and a wire-grid of the same period printed on either side of a very thin substrate. Unique features of the loop-wire design include localized frequency-selective properties, higher-order frequency response achieved by a single substrate, lack of passband harmonics in the frequency response, and very low sensitivity of the frequency response to the incidence angle. High-order frequency response is accomplished through the application of a thin substrate that allows considerable couplings between the elements on the opposite sides of the substrate. The layers' coupling in conjunction with the characteristics of each layer are designed to produce a high-Q, bandpass frequency response, in addition to a transmission zero. It is shown that by inserting variable capacitors in the gap between the metallic loops, the center frequency of the passband can be tuned over nearly an octave. In addition, using a cluster of loops as the unit cell and modifying the parameters of the loops within the cluster, a dual-band characteristic from a single-layer FSS can be achieved. A prototype sample of the loop-wire miniaturized-element FSS, whose unit cell are as small as $\lambda/12$, is fabricated to verify the design performance through a standard free-space measurement setup. The transmission characteristic of the structure is measured and compared with numerical simulation results. To test the tunability performance of the FSS, a waveguide measurement setup is employed. Prototypes of the structure in the form of a waveguide flange at X-band are fabricated and then loaded with fixed-valued, chip capacitors of different values. The

measurement results verify the simulations, thus showing the wide tunability range of the loop-wire FSS with acceptable performance.

3.3.1 Design Specifications

The proposed miniaturized-element loop-wire FSS has two printed layers separated by a very thin dielectric substrate. On the top surface, there is a 2-D, periodic array of metallic, square loops and, on the bottom, there is a wire-grid. A square portion of the surface containing a few unit cells is shown in Fig. 3.6. The structure is designed symmetrically with respect to both x and y axes so that its response is polarization insensitive. Also, in Fig. 3.7, the unit cell static design parameters are indicated including the loop-trace width δ, the spacing between the loops s, the grid-strip width w, the substrate thickness t, and the unit cell dimensions D_x and D_y. In the following, a brief description of the behavior of the layers and their interaction is presented to give insight into the structure operation mechanism.

The study of the FSS's layers starts with the wire-grid. It is well known that thin, metallic strips supporting axial electric current excited by an incident wave generate an inductive response [1]. The total inductance produced depends on the width and length

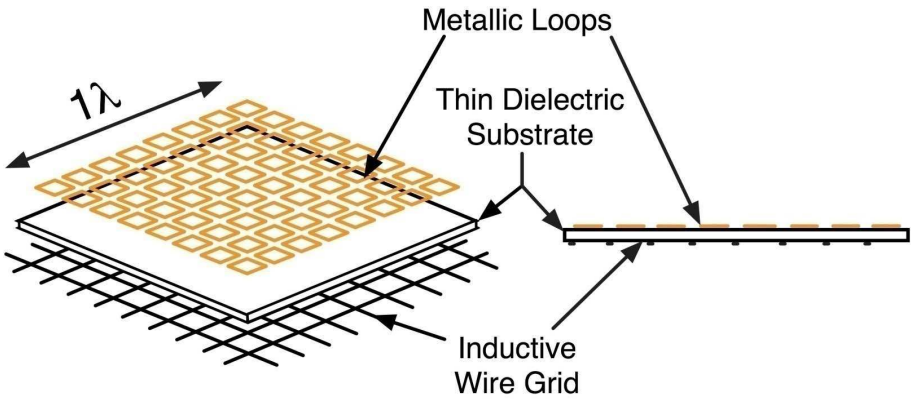

Figure 3.6: The loop-wire miniaturized-element FSS- The FSS surface screen consists of a loop-array on one side of the substrate and a wire-grid on the other side- For changing the capacitive content of the FSS, lumped capacitors interconnect the loops in both $\hat{x}$ and $\hat{y}$ directions to maintain the symmetry of the structure.

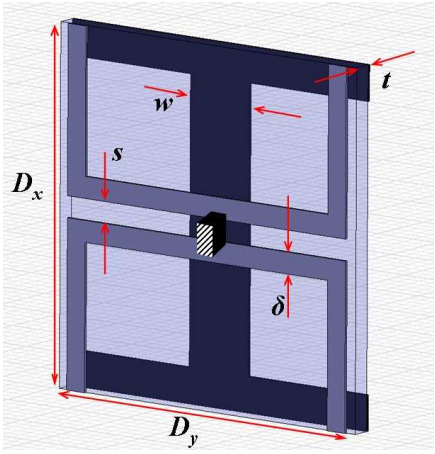

Figure 3.7: The patch-wire miniaturized-element FSS- The unit cell geometry of the FSS including the physical parameters of the loop and the wire that affect the frequency response. The zebra-striped box is where the capacitor is mounted.

of the strips as well as the field polarization with respect to the strips. The wire-grid is symmetrical and, therefore, polarization independent.

The loop layer has a combination of both inductive and capacitive responses [83]. For an $\hat{x}$-polarized (see Fig. 3.6) plane-wave normally incident upon the structure, positive and negative charge densities are established along the adjacent edges of the successive square loops, storing electric energy in the capacitors (gaps) between the loops. A close examination of the loop structure reveals that the loops can also store magnetic energy, giving them an inductive characteristic. This is from the metallic strips of the loops that are parallel with the electric field and support an electric current, thus giving rise to the inductive behavior. Hence, while the two $\hat{y}$-directed sides of the loops, that are perpendicular to the electric field, are acting as the plates of a capacitor, the two $\hat{x}$-directed sides act as inductors. Two neighboring square loops, as a result, constitute a series combination of a capacitor and an inductor, generating the loop layer bandstop characteristic. As mentioned above, the behavior of this miniaturized-element FSS also depends on the interaction of the layers. A very thin substrate is used in this design to increase this interaction which is explained as follows.

The magnetic field induced by the current flowing in the wire-grid encircles the strips of

the grid itself. A portion of that field couples through the square loops on the other layer, inducing some electric current on the loops' traces. Conversely, the current on the loops produces a magnetic field that couples to the wire-grid. This inductive, mutual coupling becomes stronger as the substrate thickness decreases.

In addition to the effect mentioned above, another kind of interaction between the layers is also observed. Based on initial, full-wave simulations of the structure, an $\hat{x}$-polarized incident electric field produces an electric field normal ($\hat{z}$-directed) to the surface between the two layers. This phenomenon, which is shown in Fig. 3.8, can be explained considering the need for displacement currents between the layers at resonance, where significant electric currents are flowing on the loops and the wire-grid. This interesting interaction, which is observed only for cases where the substrate is very thin, is modeled as a capacitive junction at the locations where the strips of the wire-grid and the square loops overlap.

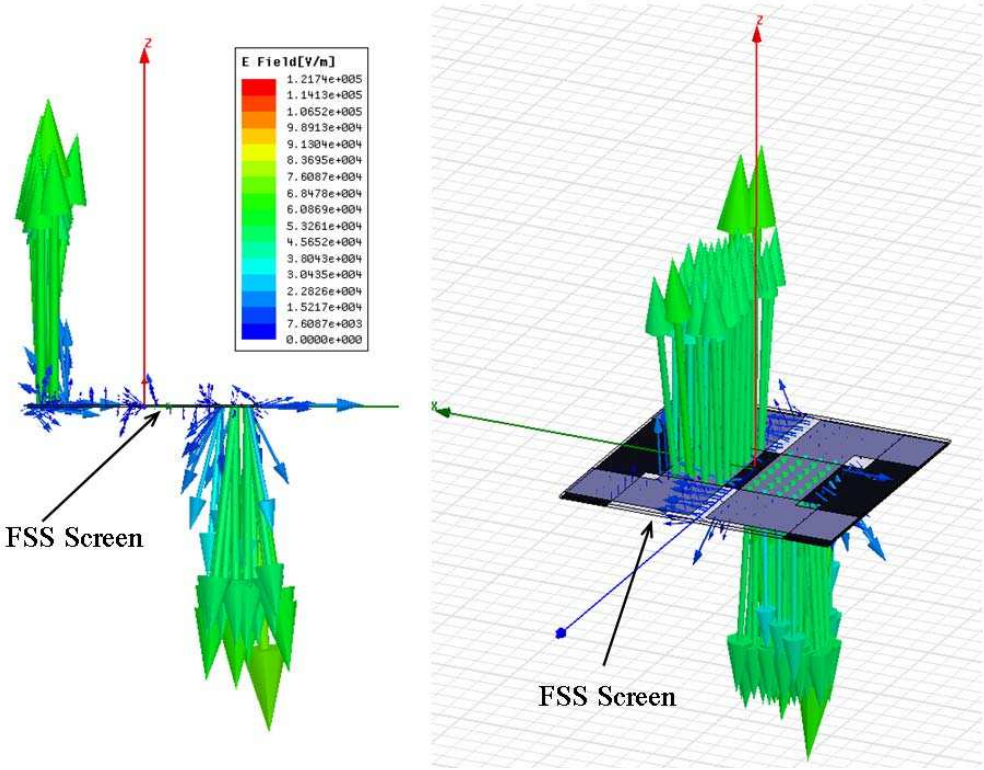

Figure 3.8: The loop-wire miniaturized-element FSS- Vector electric field plot shows the existence of significant normal field components between the two layers justifying the placement of the series capacitance in the equivalent circuit model.

In summary, the proposed structure is a parallel combination of highly coupled bandstop and inductive surfaces. By choosing proper dimensions and aligning the surfaces, desired bandpass or bandstop characteristics are obtained. Finally, the tunability of the response can be achieved by altering the loops' gap capacitance, for example, by interconnecting the loops via lumped capacitors, as shown in Fig. 3.7. The results of a parametric study are presented below for qualitative and quantitative determination of the effect of each surface parameter.

3.3.2 Parametric Study and Circuit Model Development

Parametric study of the miniaturized-element FSS begins with development of a circuit model to describe the expected frequency behavior of the surface qualitatively. A circuit model is highly desirable at the design stage to quickly predict the response of the structure with some level of accuracy. Finding a circuit model for frequency-selective surfaces, however, is not always possible. This is especially true for FSS structures composed of resonant geometries for which significant mode (Bragg) couplings take place. That is, the energy from the fundamental TEM mode of the incident wave is distributed among all non-propagating Bragg modes that eventually constitute the surface current. In these cases, equivalent circuit models do not exist and accurate analysis can only be accomplished using full-wave numerical simulations. The proposed loop-wire design operates entirely in TEM mode and makes use of very small-size elements. As a result, no significant higher order mode couplings are expected. Hence, a simple circuit model is sufficient to characterize the behavior of the structure.

To arrive at an accurate model, sensitivity analyses using a full-wave simulator are carried out. The full-wave approach is also necessary to establish the relationship between the physical parameters of the miniaturized unit cell and the lumped elements of the circuit model. Having an accurate circuit model, one can synthesize a desired frequency response (center frequency, bandwidth, insertion loss, and tuning range) by an optimization method in a reasonably short time using a circuit simulator.

A circuit model based on the qualitative description of the loop-wire structure provided

in the previous section is shown in Fig. 3.9. This model ignores all metallic and dielectric losses. The model includes two parallel branches, representing the two layers.

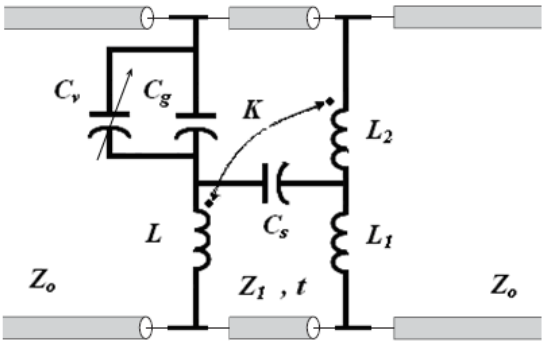

Figure 3.9: The loop-wire miniaturized-element FSS- Equivalent circuit model for the coupled wire-grid and bandstop surfaces of the proposed miniaturized-element frequency selective surface.

The right branch in the circuit models the wire-grid which is purely inductive. For this branch, the sensitivity analysis shows that increasing the strip width w decreases the inductors L_1 and L_2. As will be shown below, the structure has an overall bandpass characteristic with a center frequency denoted by f_c. Reducing the wire-strip width obviously decreases f_c, but simulations also show that the bandpass response bandwidth becomes wider.

The left branch in the model, on the other hand, represents the array of loops that acts like a bandstop (notch) circuit (series LC). The total capacitance used in the circuit model is composed of the loops' gap capacitance, C_g, and the lumped capacitor, C_v, that is mounted in parallel with C_g in the gap between two neighboring loops. The gap capacitance, C_g, is a function of the gap spacing, s, and, to a lesser extent, the loop-strip width, δ (see Fig. 3.7). Characterization of the gap capacitance has been discussed in [5]. As expected, increasing s decreases the capacitance, which in turn increases the notch frequency (f_o) at which there is a transmission zero in the frequency response of the circuit. The simulations indicate that increasing s also increases f_c. It is also observed that increasing δ results in an increase in f_o. This is mostly due to the lower inductance of the wider strip. A more detailed study, however, reveals that changing the loop-trace width also changes the gap capacitance,

as mentioned above. Although increasing δ increases the gap capacitance, the inductance decreases in such a manner that both f_c and f_o increase. This is due to the very small value of the gap capacitance, C_g, compared to that of the lumped capacitor, C_v, mounted between the loops. As a result, the loop-trace width primarily affects the inductance of the loop surface without changing the gap capacitance significantly.

In addition to the elements discussed above, the circuit model has other elements that represent the interactions between the layers. The magnetic interaction discussed in the previous section is modeled by a mutual inductance, K, in the circuit model; this coupling becomes larger to represent increased coupling as the substrate thickness decreases. The displacement current flowing between the layers forms a capacitive junction which is modeled as a series capacitor, C_s. To model the substrate, a very short piece of transmission line is placed between the shunt branches. Sensitivity analysis shows that increasing the substrate

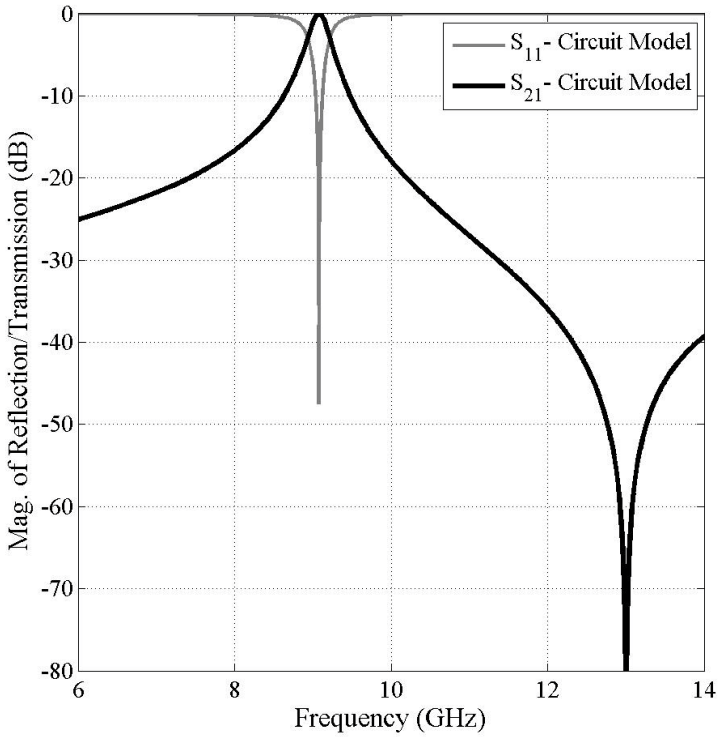

Figure 3.10: The loop-wire miniaturized-element FSS- Circuit model simulation shows a bandpass characteristic with high selectivity and low insertion loss, including a transmission zero.

thickness, t, beyond $200\mu m$, increases the insertion loss drastically, hence degrading the bandpass characteristics of the response. Moreover, f_c slightly decreases as t increases.

Given the equivalent circuit model described above, a set of typical values are chosen for the circuit elements to show the expected frequency response of the surface (Fig. 3.10). A bandpass behavior (about 9GHz) with a transmission zero (about 13GHz) is clearly demonstrated. The value of each circuit element is: $L_1 = 0.15$ nH, $L_2 = 0.05$ nH, $L = 1.5$ nH, $K = -1$, $C_s = 0.05$ pF, and $C(= C_g + C_v) = 0.1$ pF.

3.3.3 Model Verification and Simulation Results

Single-Bandpass Frequency Behavior and Its Tuning Performance

In Section 3.3.2, the synthesis of a highly selective bandpass response by the miniaturized-element FSS was shown to be possible, assuming the accuracy of the circuit model. Next, employing the trial-and-error approach, a full-wave simulator is used to verify the behavior of the structure.

Table 3.2: The Loop-Wire Miniaturized-Element FSSs' Static Design Parameters at X-Band for Free-Space Operation

Design / Parameter	**The 1st**	**The 2nd**	**The 3rd**
s	0.12 mm	0.15 mm	0.12 mm
δ	1.08 mm	0.15 mm	1.08 mm
w	1.2 mm	0.5 mm	1.05 mm
t	0.04 mm	0.125 mm	0.125 mm
ε_r	2.2	2.2	2.2
$D_x \times D_y$	4 mm × 4 mm	2.5 mm × 2.5 mm	4 mm × 4 mm

In this section, three different miniaturized-element designs whose parameters values are provided in Table 3.2 are presented. Full-wave analyses are based on the finite element

method (FEM) using Ansoft HFSS; both dielectric and metallic losses are included. The accuracy of the circuit model is also verified using a sensitivity analysis by which the corresponding values for the elements of the circuit model are extracted to best fit the full-wave results.

In the following, the frequency tuning capability is studied numerically by altering the lumped capacitance mounted in the loops gap. The simulation results for the first loop-wire design (see Table 3.2) are shown in Fig. 3.11. As can be seen, a frequency range from 6.7 to 9.4 GHz is swept by altering the lumped capacitance from 0.7 to 0.2 pF. The simulations predict a very wide tuning range with very little degradation in the structure performance. Fig. 3.12 shows the simulation results for the second loop-wire FSS with unit cell dimensions of $2.5mm \times 2.5$ mm. Among the designs considered here, the second design achieves the smallest cell size. Similar to the first design, the second design has also a very wide frequency tuning range. In this case, the center frequency changes from 6.4 to 9.7 GHz by changing the capacitance from 0.3 to 0.1 pF. This capacitance range is rather small and,

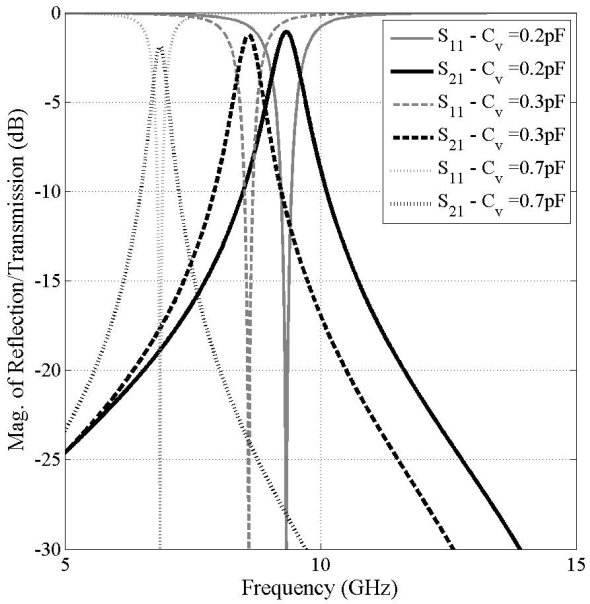

Figure 3.11: The loop-wire miniaturized-element FSS- Full-wave simulations of frequency response (return loss and transmission) of the first loop-wire FSS including metallic and dielectric losses. The results show that a wide tuning range is obtained by tuning the lumped capacitance, C_v, from 0.2 to 0.7 pF.

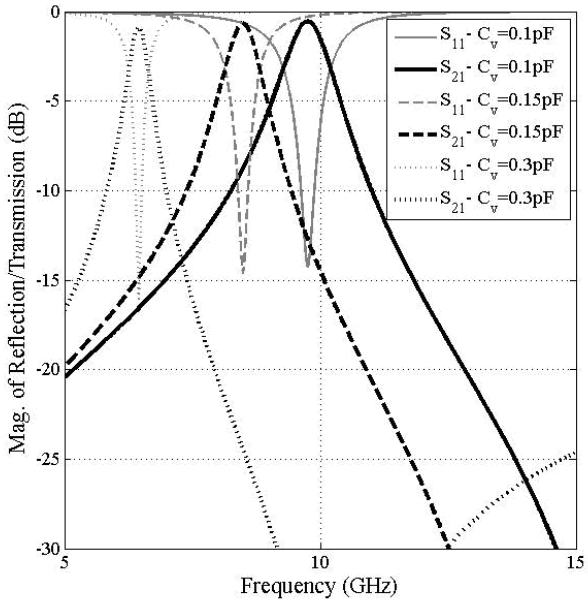

Figure 3.12: The loop-wire miniaturized-element FSS- Full-wave simulations of frequency response (return loss and transmission) of the second loop-wire FSS including metallic and dielectric losses. The results show that a wide tuning range is obtained by tuning the lumped capacitance, C_v, from 0.1 to 0.3 pF.

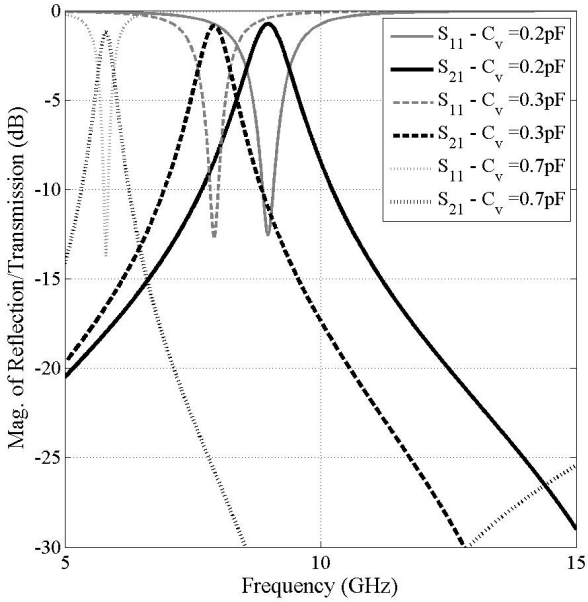

Figure 3.13: The loop-wire miniaturized-element FSS- Full-wave simulations of frequency response (return loss and transmission) of the third loop-wire FSS including metallic and dielectric losses. The results show that a wide tuning range is obtained by tuning the lumped capacitance, C_v, from 0.2 to 0.7 pF. This design provides lower insertion loss and uses a thicker substrate compared to the first design.

thus, not very desirable in practice.

Finally, Fig. 3.13 shows the simulation results for the third loop-wire structure. This design also achieves a wide tuning range for the capacitance range of 0.7 to 0.2 pF. The third design, however, has a lower insertion loss compared to the first design. Another advantage of the third design is in that its substrate is considerably thicker than that of the first and, therefore, is much easier to fabricate and handle experimentally.

As mentioned previously, a major advantage of the miniaturized approach compared with conventional methods relates to the harmonic response of the FSSs. As discussed earlier, old FSSs are comprised of resonance-length elements. Readily, harmonics of the main (first) resonance contaminate the frequency response of such FSSs. An array of dipole, for example, creates multiple strong scattering (resonances) at frequencies where the electrical length of the dipoles is $\lambda/2, \lambda, 3\lambda/2$, etc. Traditional FSS in a sense has limitations because of its dependence on the structurally-based resonances.

The main resonance in the new FSS, however, is located at a frequency which is about an order of magnitude lower than the first resonance of its elements (loops). This confirms that the new approach provides a filtering response independent of the elements' stand-alone

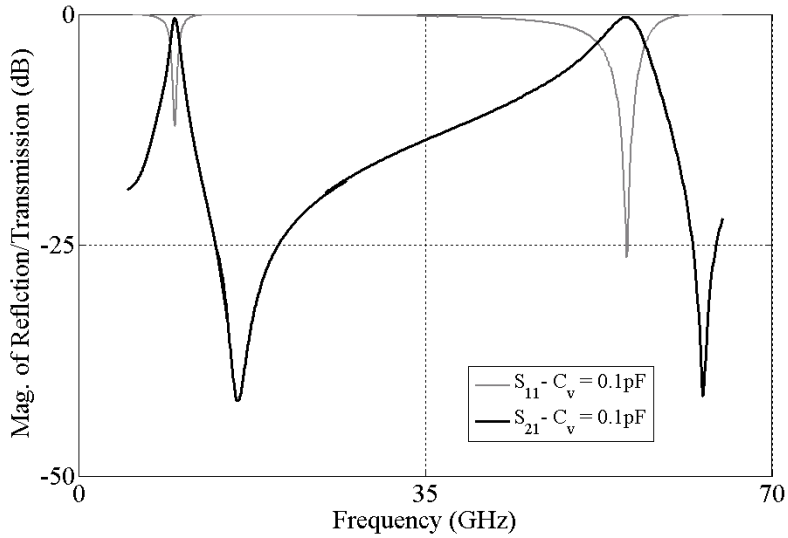

Figure 3.14: The loop-wire miniaturized-element FSS- Full-wave simulations of frequency response (return loss and transmission) of the second loop-wire FSS including metallic/dielectric losses and a capacitance value of $C_v = 0.1$ pF. As can be seen, the first harmonic of the main passband is located at about 60 GHz.

resonances. The spectral response of the second loop-wire FSS (Table 3.2) up to 70 GHz is shown in Fig. 3.14. As shown, the center frequency of the passband ($\approx$ 10 GHz) is over six times lower than the second closest hump ($\approx$ 60 GHz) in the transmission response. Interesting point about this plot is that the frequency of the second transmission zero is exactly where the loops become resonant (loop circumference = λ). This figure well shows the wide band of frequency available to this FSS over which no harmonics exist.

Equivalent Circuit Model for the Single-Bandpass Surface at Normal Incidence

Comparison of the circuit model response with the full-wave simulations for the second design is shown in Fig. 3.15. Extracted circuit elements values are given in Table 3.3. Two different values of the lumped capacitance, i.e., C_v = 0.15 and 0.3 pF, are used to show the validity of the circuit model. As shown, the model response not only predicts the FEM results, but it also tracks the FEM results as the lumped capacitance is tuned. The circuit model, however, ignores the losses associated with the metal and the substrate. The existence of such an accurate lumped circuit model for the loop-wire FSS well proves the

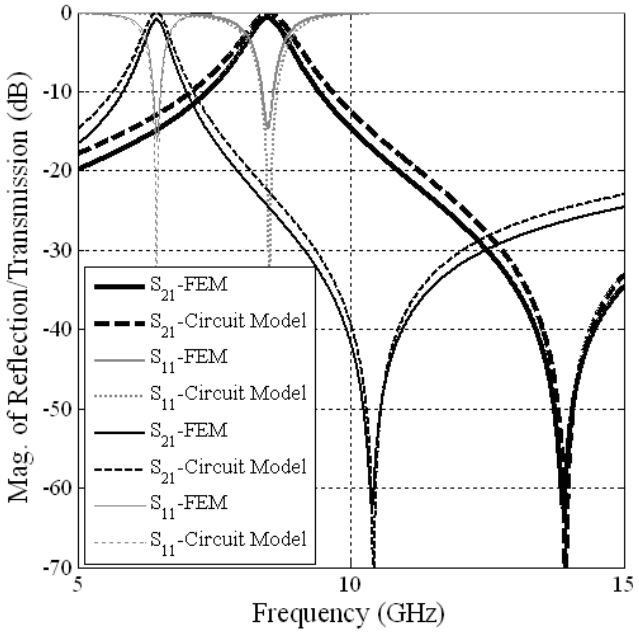

Figure 3.15: The loop-wire miniaturized-element FSS- Circuit model simulations are compared against FEM model for the second miniaturized-element FSS design and for different values of the lumped capacitor: C_v = 0.15 and 0.3 pF.

TEM operation (Section 3.3.2) of this FSS.

Table 3.3: The Circuit Model Values for the Second Loop-Wire Miniaturized-Element FSS (see Fig. 3.15)

C_g	L	L_1	L_2	C_s	K
8.41 fF	0.755 nH	0.523 nH	0.0565 nH	58.75 fF	-0.97

Dual-Bandpass Frequency Response

In many communications and radar applications, frequency-selective surfaces with multi-band characteristics are highly desirable. The new miniaturized-element FSS can be designed to provide such characteristics from just a single substrate layer. This is accomplished in a rather straightforward manner because of the very small unit cell dimensions of the new design and the localized nature of the frequency response. To achieve a multiple bandpass behavior, one needs to increase the number of poles and zeros. For past designs, an increase in the number of poles and zeros translates to having a multilayer FSS. Due to the small size of the unit cells of the loop-wire FSS, the number of poles and zeros can be increased by using a cluster of loops with different parameters as the unit cell.

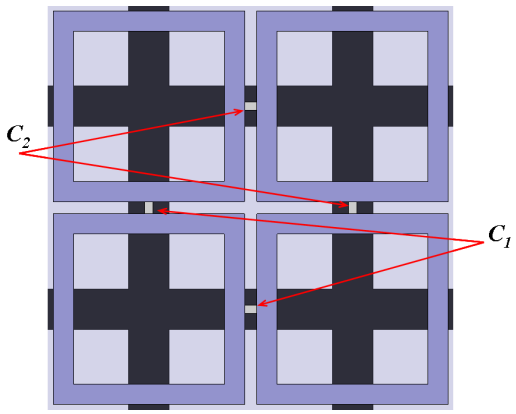

Figure 3.16: Unit cell of a dual-bandpass miniaturized-element FSS composed of a cluster of four identical loops, but with different lumped capacitors.

A dual-band response is demonstrated here by considering a four-loop cluster as the unit cell and simply placing different lumped capacitors in the gaps between the loops, as shown in Fig. 3.16. The equivalent circuit of this composite loop-wire surface is two parallel circuits, each similar to that shown in Fig. 3.9. It can be shown that by proper choice of the lumped capacitors C_1 and C_2, a dual bandpass response can be obtained. Using the parameters of the second design given in Table 3.2, changing the loop-trace width δ from 0.15 to 0.25 mm, and choosing $C_1 = C_1 = 0.1$ pF, a single bandpass frequency response, shown in Fig. 3.17, is produced. By changing the capacitance values to $C_1 = 0.05$ pF and $C_2 = 0.2$ pF, a dual-band response, also shown in Fig. 3.17, is obtained.

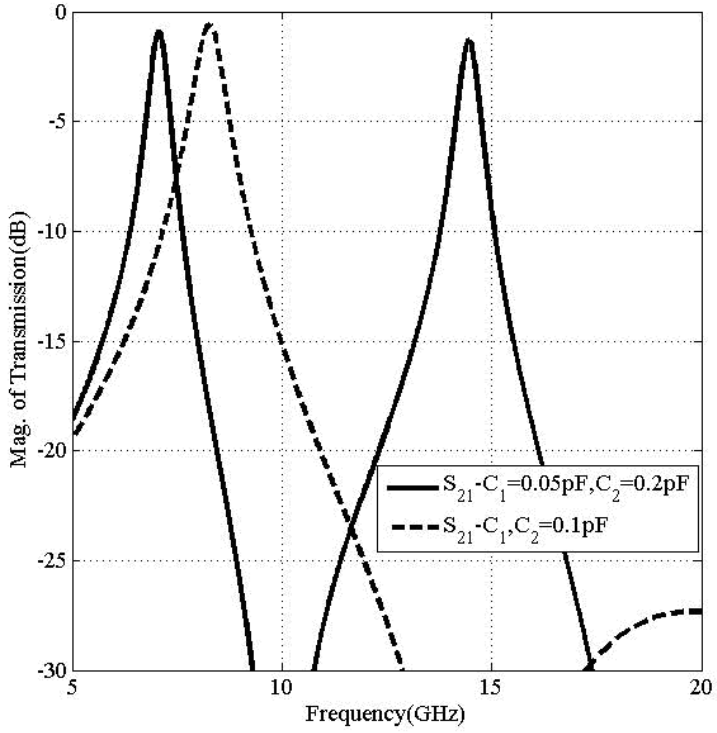

Figure 3.17: Frequency response of a dual-band miniaturized-element FSS obtained by using a cluster of four loops as the unit cell and choosing different values for the lumped capacitors. Two cases are compared to each other: The dashed line is for the case where the two capacitors used in the four-loop cluster are the same ($C_1 = C_2 = 0.1$ pF), and the solid line shows the results when the capacitors are different ($C_1 = 0.05$ pF and $C_2 = 0.2$ pF).

3.3.4 Experimental Verification

Free-Space Measurement

To demonstrate the validity of the simulations in a free-space environment, a prototype sample of the loop-wire miniaturized-element FSS at X-band is fabricated and tested using a free-space measurement setup. The setup is composed of a lens-corrected horn antenna for creation of a uniform phase front over a finite aperture and a high-gain antenna in the far field. The surface is placed adjacent to the horn, as shown in Fig. 3.18, and the receiving antenna is in the far-field region of the horn and surface.

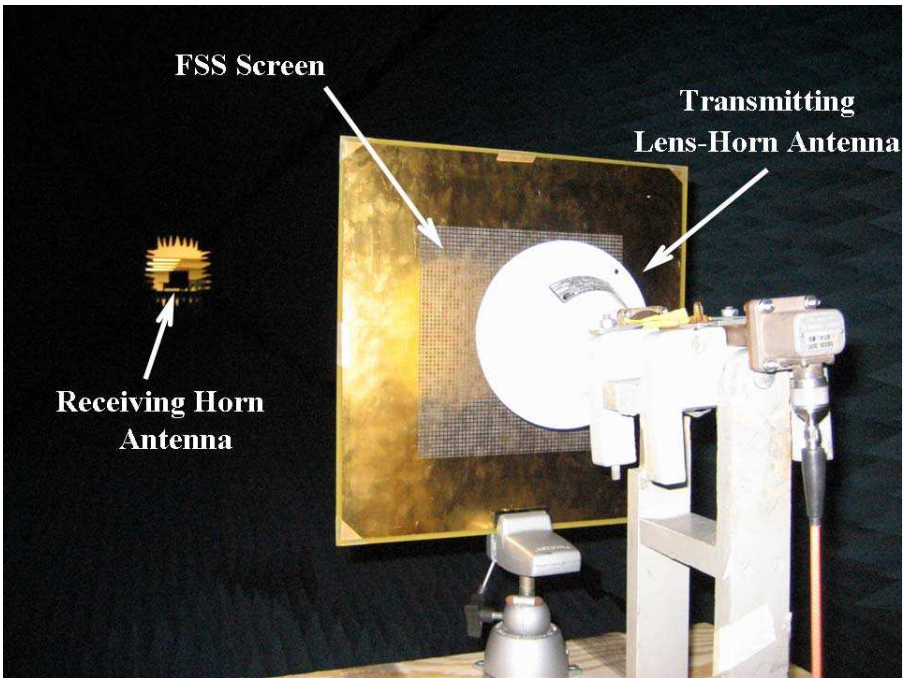

Figure 3.18: Free-space measurement setup consisting of a receiver, a transmitter, and the miniaturized-element FSS in between.

The surface is fabricated using a low-loss Duroid substrate through a printed circuit board etching process. 0.1-pF thin-film chip capacitors with a very small package size (0201 standard size) are then mounted in the loop gaps. The fabricated sample is based on the third design whose parameters values are listed in Table 3.2. The designed screen which is shown in Fig. 3.19 is 6 in $\times$ 6 in and includes 38 $\times$ 38 unit cells.

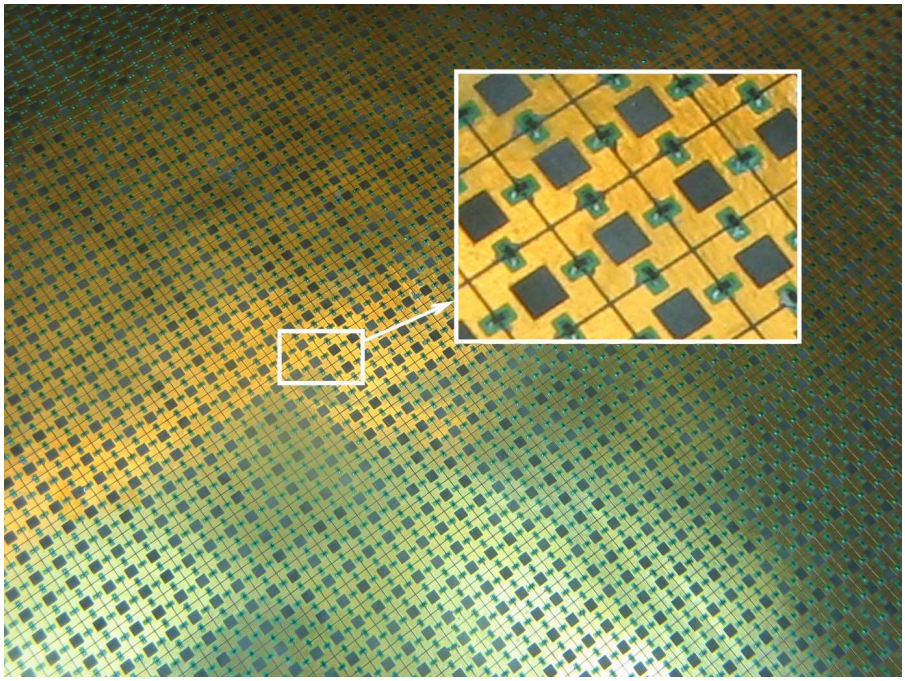

Figure 3.19: Fabricated surface using fixed lumped capacitors. This prototype uses approximately 3000 capacitors with capacitance value of $C = 0.1$ pF. This figure shows the loop layer.

An 8720D vector network analyzer (VNA) is employed to measurer the transmissivity through the sample. A thru calibration is performed to calibrate the network analyzer within a frequency band of 8.4–11.15 GHz (the lens-horn band of operation) in the absence of the surface. Fig. 3.20 compares the simulation and experimental results at normal incidence. Fig. 3.20 also includes the case in which the polarization of the incident wave is rotated by an angle 45 about the surface normal. As predicted by the simulations, the structure is polarization insensitive. The measurement results for oblique incidence up to 45^o , are shown in Fig. 3.21. As expected, the new design shows only minor frequency response dependence to the incidence angle. A good agreement between the measured and simulated results is observed.

Fig. 3.18 proves the ability of the new approach in decreasing the overall dimensions of an FSS. As shown, the panel size of the FSS is as large as the footprint of the transmitter. Another new feature is about the issue of distance mentioned earlier. In this setup, unlike conventional methods for measuring FSS in the air, the FSS is placed very close to the

transmitting antenna and yet performs the filtering.

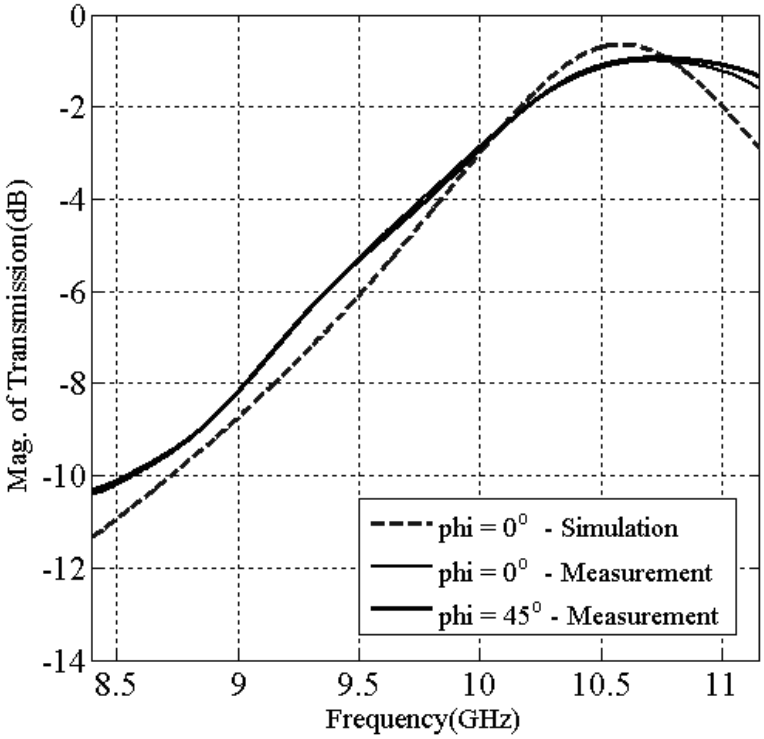

Figure 3.20: The loop-wire miniaturized-element FSS measurement results versus numerical simulation- Angle *phi* measures the orientation on the FSS plane. In both cases $phi = 0^o$ and $phi = 45^o$, the incident wave polarization is parallel to the surface. This measurement shows that the design is polarization insensitive.

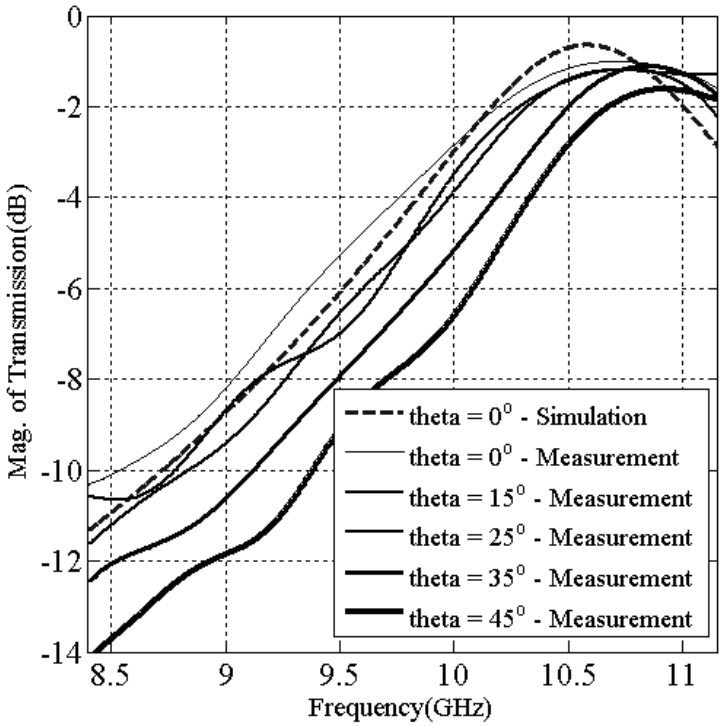

Figure 3.21: The loop-wire miniaturized-element FSS measurement results versus numerical simulation- This measurement shows the effect of off-normal excitation of the surface. Angle *theta* represents the angle between the propagation vector of the incident wave and the normal to the surface.

Tunability Measurement

Another practical feature of frequency-selective surface structures design is the ability to electronically tune the frequency response of these structures. In [85–93], frequency tunability has been accomplished by altering the substrate constitutive parameters. Other methods include either changing the structure geometry using RF-MEMS technology [96, 97], or manipulating the FSS layers' reactive characteristics by incorporating tuning elements into the layers' design [102–104, 106, 107].

It is well known that certain periodic structures can be measured in a waveguide transmission line [79]. In a waveguide environment, an FSS designed for operation in a free-space environment should be modified slightly to compensate for the effect of the waveguide metallic walls. The sides of the rectangular waveguide can perturb the design periodicity once image theory is applied. To prevent such a perturbation, the walls need to lie on the symme-

try planes of the FSS surface. In a rectangular waveguide, the incident wave upon the FSS surface is TE_{10} mode which represents two incident plane waves at opposite oblique incidence angles at a given frequency. Accordingly, if the waveguide aperture covers an integer number of the unit cells along its width and length, and the covered portion has a center of symmetry that lies on the center of the aperture, then the waveguide walls coincide with the symmetry planes. In other words, the waveguide measurement imposes a new constraint on the unit cell size. Therefore, the closest dimensions to those previously used for the free-space design are redesigned such that the waveguide aperture covers an integer number of elements. The appropriate unit cell has dimensions 3.39 mm $\times$ 3.27 mm which correspond to 3 $\times$ 7 unit cells to cover a WR-90 waveguide aperture (10.16 mm $\times$ 22.86 mm). Further optimizations are employed again to achieve the intended response [82].

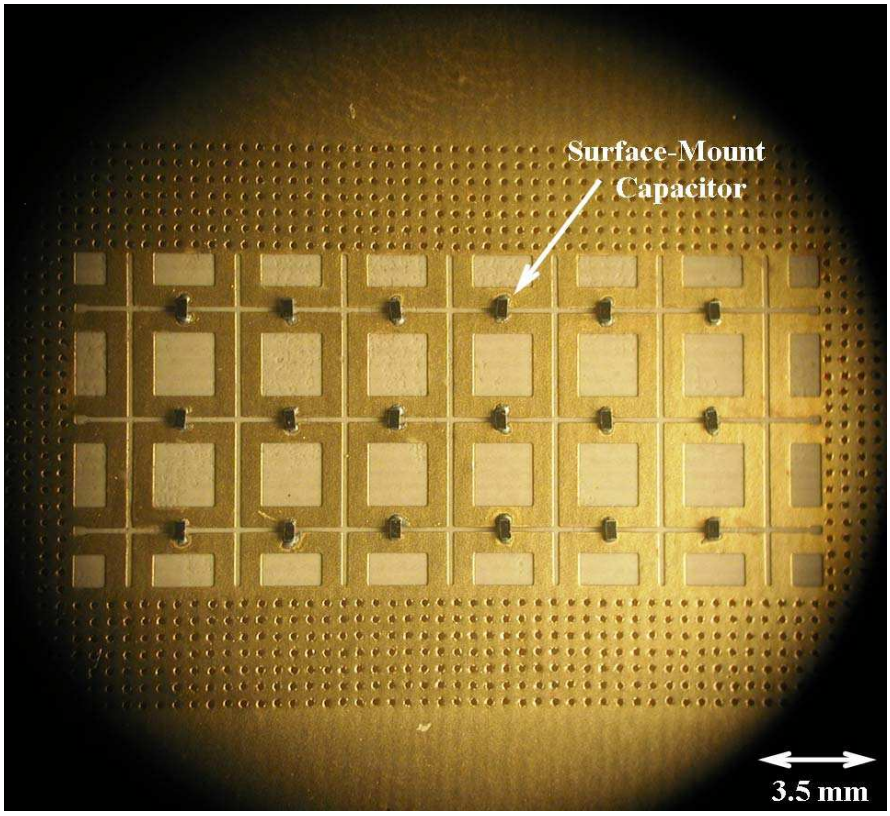

Figure 3.22: The loop-wire miniaturized-element FSS- The waveguide prototype which is an array of 3 $\times$ 7 unit cells, each of which loaded with a surface-mount capacitor (black boxes) parallel with the direction where the electric field polarization (TE_{10}) lies on.

A picture of the miniaturized-element prototype design for waveguide testing is provided in Fig. 3.22. This figure shows the loop array along with lumped capacitors between the loops. To facilitate the flow of the longitudinal conduction current on the waveguide walls, via holes are fabricated on the perimeter of the aperture where the waveguide flanges meet (see Fig. 3.22). Lack of good metallic contact results in disruption of the longitudinal currents, thus generating spurious responses. The geometrical parameters for the waveguide design are summarized in Table 3.4. Measurements are performed in a calibrated WR-90 S-parameter measurement setup shown in Fig. 3.23. The setup includes an 8772D VNA, coaxial cables, and WR-90 standard waveguide sections.

Table 3.4: The Loop-Wire Miniaturized-Element FSS's Design Parameters at X-Band in Waveguide

s	δ	w	t	ε_r	$D_x \times D_y$
0.12 mm	0.675 mm	1.05 mm	0.1 mm	2.94	3.39 mm × 3.27 mm

Four samples of the miniaturized-element FSS with the same geometrical parameters (provided in Table 3.4) are fabricated and then loaded with different, fixed-valued capacitors (0.05, 0.1, 0.15, and 0.2 pF). Fig. 3.24 shows the transmission response for the four different samples. The measurement results show that the center frequency of the response can be changed from 8.49 to 11.48 GHz by simply changing the capacitance of the lumped capacitors. An increased insertion loss (from 1.5 to 2.7 dB), however, is observed as the center frequency decreases. This decrease is partly attributed to impedance mismatch of the surface at lower frequencies in the waveguide. To tune the center frequency down, the lumped capacitance value is increased. Given the circuit model, it can be shown that increasing the capacitance alone reduces the bandwidth and degrades the matching of the filter. Such an effect is inherent in the filters of this type and the simulation results also predict it. In the waveguide, however, another effect also adds to the problem; the lower the frequency is, the steeper the incidence angle becomes. This is due to the center frequency getting closer to

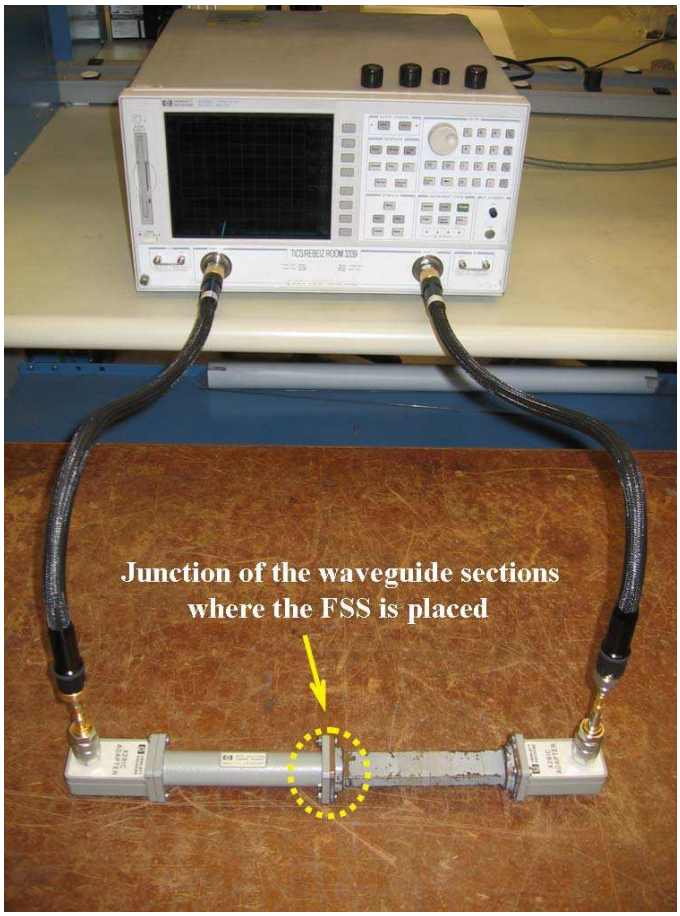

Figure 3.23: Waveguide measurement setup consisting of a VNA, cables, and WR-90 waveguide sections. The FSS is placed in between the two waveguide flanges.

the cutoff frequency of the waveguide. Another trend shown in Fig. 3.24 is that as the FSS is tuned down to lower frequencies, the deviation of the simulation from measurement becomes larger. This issue is associated with the chip capacitors used. The Q-factor of the capacitors decreases as their capacitance increases. In real scenarios where the FSS is operating in a free-space environment near normal incidence, however, the insertion loss is expected to be improved by at least 1 dB.

The measurements show the frequency tuning using fixed-valued capacitors. For real-time tuning, however, surface-mount varactors are needed. The major problem associated with varactors is the bias circuitry required for controlling individual varactors. Although not tested experimentally, a possible approach is to use the loop array itself as the bias

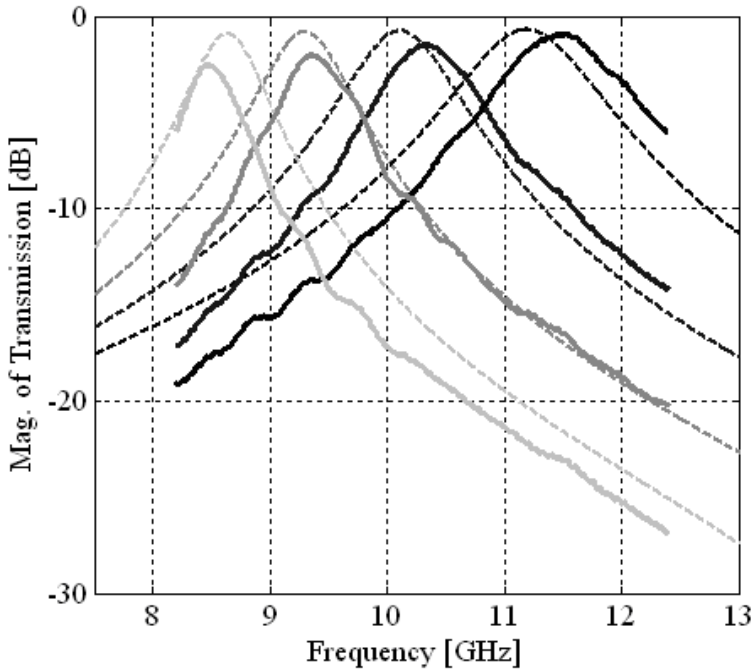

Figure 3.24: The measured transmissivity (solid lines) of the loop-wire FSS in waveguide compared to the full-wave simulation results (dashed lines)- Altering the lumped capacitance from 0.05 to 0.2 pF with a step of 0.05 pF decreases the center frequency from 11.5 to 8.5 GHz.

network for the inserted varactors recalling that the varactors are placed in the loops gaps in both vertical and horizontal directions to maintain the symmetry. The single loop at the top, right corner is connected to a voltage $+v_0$, and the loop element on the opposite corner (bottom, left) takes a zero voltage, thus reverse biasing the varactors in between. Assuming reasonably similar varactors, a uniform voltage difference is expected to be established across each two successive loops once moving from the top, right along the surface towards left and bottom. The two corner loops should be RF-decoupled in order to bypass the voltage source at the frequency of operation.

In practice, however, achieving a uniform voltage distribution across the surface might not be feasible using the method described above given the tolerances of varactors. This method in fact is undesirable since the surface is exposed to single-point failure risk. A practical approach is to use a parallel resistive network [105]. This network simply consists of chip resistors each of which is mounted in parallel with a varactor in the array. The value

of the resistors is chosen such that the performance of the FSS is maintained. This will be discussed in more detail in Chapter 5.

3.4 Chapter Conclusions

In this chapter, a new miniaturized-element frequency-selective surface comprising a wire-grid and a loop-array is presented. A single substrate is used to generate a higher-order, bandpass characteristic with tuning capability. The dimensions of the unit cells of the loop-wire FSS can be as small as $\lambda/12$. The salient feature of the new structures is that their frequency-selectivity is localized and thus suitable for moderate size antenna applications at low frequencies. A higher-order frequency response is achieved by establishing proper coupling between the inductive (wire-grid) and bandstop (loop-array) surfaces on either side of the substrate. An accurate circuit model for the proposed design is developed that allows for rapid optimization of a desired frequency response. The accuracy of the circuit model is verified using a full-wave approach. The frequency characteristics of the FSS and its tuning capability are measured through the free-space and waveguide experiment setups. The expected bandpass characteristics of the FSS are verified. A wide tuning range, with a negligible loss of performance, is demonstrated by altering the capacitance of the chip capacitors interconnecting the loops. A good agreement between the simulations and experimental results is observed.

CHAPTER 4

Multipole Miniaturized-Element Frequency-Selective Surfaces

This chapter presents a novel multipole miniaturized-element frequency-selective surface having a very low thickness and a desired multipole frequency response [47]. For this design, new miniaturized FSS elements are developed to achieve a low thickness solution and improved functionality. The proposed FSS enables implementation of higher order spatial filters over low-profile conformal antenna arrays. First, design of a very thin, modified miniaturized-element FSS producing a single-pole bandpass response and a transmission zero is presented. The modified design is a single-sided circuit-board with a particular unit cell consisting of a loop centered within a wire-grid. Next, using a similar metallic pattern on the other side of a substrate, a dual-bandpass frequency response is produced. This response is achieved by choosing proper dimensions for the loops and wire of each layer and by appropriately positioning the layers with respect to each other. To establish a benchmark, dualpole FSSs using cascaded layers of a previously designed miniaturized-element FSS (Chapter 3) are considered. In comparison with the benchmark, the modified dual-bandpass design has only two metallic layers, instead of four, and a single substrate, instead of three. The proposed multipole FSS is $\lambda/240$ thick which is six times thinner than the benchmark structures. Moreover, the frequency response of the new FSS shows higher out-of-band rejection values. Performance of the multipole screens is tested by fabricating FSSs with maximally-flat and dual-bandpass responses and measuring their frequency responses

using a standard measurement setup in a free-space environment.

4.1 Chapter Introduction

Frequency-selective surface (FSS) structures with multipole filtering characteristics have been widely investigated in the microwave and millimeter-wave frequencies of the spectrum [1–3]. These surfaces have been often employed in the design of multiple-frequency antennas like multiband reflector antennas [39, 40]. The multiband FSS used in these reflector systems forms a sub-reflector in addition to the large reflecting dish in the system. Multiband FSS structures are commonly formed based on two methods. These methods either combine (cascade) previously designed, single-band FSSs or use multiresonant elements as the unit cells of the FSS. In [42], a stack of single-frequency FSSs is used to achieve a multiband frequency response. In [43, 44], two identical resonant elements (double square loop or double ring patch) are embedded in the unit cell to produce a multipole response. Optimization algorithms have also been used to design and refine the unit cell geometry to generate a desired multiband response [45]. Another method employs elements with fractal shapes [46]. Given the self-similarity property associated with the fractals, the FSS made up of such elements has the same geometry in multiple frequency bands. As a result, similar effects are observed in different frequency bands, thus resulting in the multiband frequency behavior of the FSS structure.

As discussed previously in Chapter 3, the first miniaturized-element bandpass FSS was reported in [37] with the goal of decreasing the dependence of the frequency response of FSS to the incidence angle of the incoming plane-wave. Another desired property was to localize the frequency-selective properties, meaning that each element of the FSS can produce the desired, filter behavior with minimal dependence on the neighboring elements. A solution was obtained by designing an FSS structure with element dimensions on the order of a tenth of the wavelength or smaller. This idea was tested and verified experimentally. Another advantage of the miniaturized-element design lies in the fact that the interaction of the surface and incoming plane-wave is predominantly in TEM mode. As a result, higher-order Bragg modes are suppressed, and harmonic responses are eliminated [38].

In this chapter, we aim at developing a very thin, multipole frequency-selective screen using the concept of the miniaturized-element FSSs developed in Chapter 3. To accomplish this, a new high-order miniaturized-element FSS that can occupy only a single side of a substrate is first introduced. This structure, which is similar to the two-sided structure presented in [38], exhibits the desired characteristics including a single-pole passband and a transmission zero. However, the new design has only one printed surface, and therefore, it becomes more suitable for thin, multilayer applications. Next, the possibility of achieving a two-pole behavior using a single, very thin substrate based on the new FSS element is investigated.

Due to the nature of their interactions with the incident wave, the miniaturized surfaces are shown to have equivalent, lumped circuit models. One advantage of having an accurate model is that standard filter theory can be used to achieve a desired filter response by combining FSS layers. Moreover, optimizations can be performed using a circuit simulator in a reasonably shorter amount of time. The knowledge obtained from the circuit optimizations then is used to design the physical surface faster using a full-wave simulator. In a way, the circuit provides better initial starting values for the full-wave design. Throughout this chapter, the behavior of the FSS structures in a multilayer fashion is physically described and modeled using the circuit theory. Circuit models of the single-pole FSSs, based on which the multipole FSSs are built, will be used to model the multilayer FSSs. The accuracy of the circuit models is verified using the full-wave simulation results. Supported by measurements, it will be shown that the miniaturized-element surfaces are in fact very versatile in achieving desired frequency responses.

4.2 A variation of the Loop-Wire Miniaturized-Element Frequency-Selective Surface: A Single-Sided Surface

It is well established that multipole FSS structures can be designed by cascading a number of single-band FSSs. Although this method is straightforward, it might be undesirable as

the layer thickness increases and the fabrication process becomes cumbersome. The latter factor is especially important if the individual single-band FSS layers have reactive, lumped elements in their design.

To address these two main concerns, an FSS element with just a single metal face is proposed. The new element also generates the desired response without the need for lumped capacitors unlike the original two-sided miniaturized-element FSS design presented in [38].

To introduce the new miniaturized FSS element, we need to revisit the fundamental behavior of the miniaturized-element FSS provided in Chapter 3. A single-pole miniaturized FSS is composed of a loop array backed by a wire grid printed on opposite sides of a typically very thin (0.005 in) substrate. Unlike traditional FSSs, the miniaturized element has a very accurate lumped-element circuit model that makes the filter synthesis process very easy. The circuit model and a thorough physical explanation of the wave interaction with the FSS can be found in Section 3.3.2 of Chapter 3. It was shown that this FSS structure could be modeled as a series $L - C$ (representing the loop-array) placed in parallel with an inductor (modeling the metallic grid). It was also discussed that the high-order frequency response of the FSS layers is achieved through the appropriate electric and magnetic coupling between

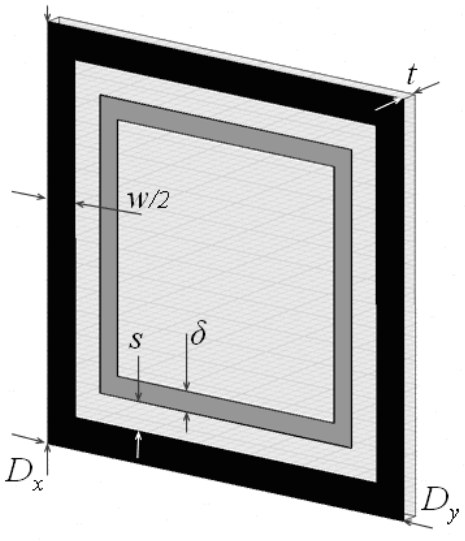

Figure 4.1: The First Modified (Single-Sided) Loop-Wire Miniaturized-Element FSS- The unit cell of the FSS composed of square loops, in gray, and a wire grid, in black, both on the same side of a thin substrate.

two faces of the FSS. The layers' coupling is controlled by changing the lateral placement of the layers with respect to one another as well as the distance between the layers.

To reduce the two-sided FSS into a single-face FSS, we placed the loops and the wire-grid on the same plane as shown in Fig. 4.1. As shown, each loop is surrounded by the traces of the grid. For this topology, the circuit model shown in Fig. 4.2 is proposed. Similar to the model for the loop-wire FSS, this circuit essentially consists of a notch branch in parallel with an inductor. There are, however, differences between the circuits since the wire and the loops in the modified, single-face FSS are placed on the same side of the substrate. One major difference between the single-face and the two-face (loop-wire) FSS is the lack of the series (junction) capacitor between the loop and wire layers in the single-face structure. In addition, the magnetic coupling coefficient is changed, and a free parameter that could control the magnetic coupling (spacing between the loop and the grid) is lost.

Circuit analysis shows that a bandpass response can be achieved by the arrangement provided in Fig. 4.2. Although using a different (weaker) coupling process, this circuit can be tuned to achieve characteristics similar to those of the original loop-wire FSS. This is accomplished by manipulating the values of the reactive elements of the circuit model to compensate for the effects of the weaker mutual coupling. However, the single-face FSS's model, working as a stand-alone bandpass filter, has a lower selectivity compared with the circuit model of the loop-wire FSS.

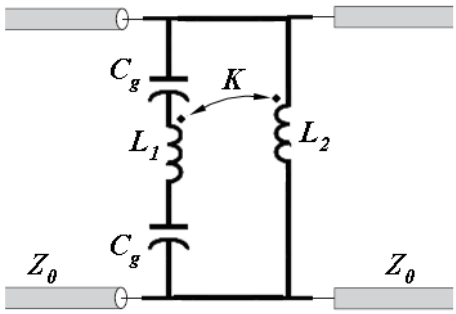

Figure 4.2: Equivalent circuit model for the modified (single-sided) loop-wire miniaturized-element FSS.

In order to analyze the performance of the modified miniaturized-element FSS, first let us

examine the equivalent circuit model of the modified FSS. This will give us a good estimate of the behavior of the actual FSS in a free-space environment. Moreover, the circuit analysis helps us to start the full-wave simulations with a better insight and initial values closer to the optimized values. In the model shown in Fig. 4.2, the gap between the loop and the wire-grid is represented by two series capacitors, C_g. For a given incident polarization, the loop traces that are parallel to the electric field are modeled by an inductor, L_1. Also, inductor L_2 represents the wire-grid, shown in black in Fig. 4.1. The overall circuit model, as a result, consists of two coupled branches: a series $L-C$ branch (L_1 and C_g) modeling the loop-array and an inductive branch (L_2) modeling the grid. The coupling of the branches is denoted by K in Fig. 4.2.

Table 4.1: The Circuit Model Values for the Single-Sided Loop-Wire Miniaturized-Element FSS

C_g	L_1	L_2	K	Z_o
0.21 pF	3 nH	2.65 nH	0.4	377 Ω

Table 4.2: The First Modified (Single-Sided) Loop-Wire Miniaturized-Element FSS' Static Design Parameters at X-Band for Free-Space Operation

s	δ	w	t	ε_r	$D_x \times D_y$
0.1 mm	0.106 mm	0.365 mm	0.125 mm	2.2	6.9 mm × 6.9 mm

Design of the single-sided FSS begins with testing its expected circuit model in order to determine the requirements of producing a bandpass behavior using the model. Table. 4.1 shows the optimized circuit values leading to a bandpass frequency response. Given this model, approximate inductive and capacitive content required for the FSS to generate a bandpass response, similar to that of the model, are determined. After choosing the values

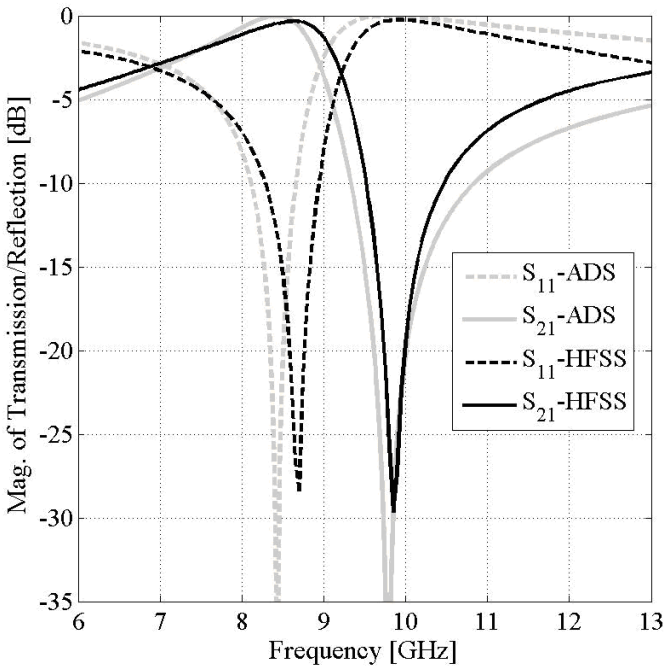

Figure 4.3: The First Modified (Single-Sided) Loop-Wire Miniaturized-Element FSS- Full-wave simulations (Table. 4.2) are well predicted by the circuit model simulations (Table. 4.1).

of the circuit parameters that enable a bandpass characteristic at X-band, the unit cell shown in Fig. 4.1 is optimized. This process is done using the full-wave solver and our knowledge gained from the previous work. The designed values for the single-face FSS are provided in Table. 4.2. The full-wave simulation results using Ansoft HFSS, compared to the circuit simulations using ADS, are shown in Fig. 4.3, demonstrating a good agreement between the results of analyses. This modified version of the loop-wire FSS is a spatial surface with a bandpass filter response comprising a passband and a transmission zero. At low frequencies the filter behavior is inductive and is dominated by the wire-grid (inductor L_2). As the frequency is increased, this inductive characteristic encounters a capacitive effect created by the notch. The bandpass behavior is achieved at the frequency where the capacitive and inductive effects reach to a balance. In other words, the passband is enclosed by an inductive, lower-frequency part and a notch (transmission zero).

Due to a higher external coupling, only a wide passband can be achieved by the single-face

FSS. Further increase in the selectivity of this filter is possible by sacrificing the insertion loss. For instance, increasing the wire width decreases the inductance L_2 (Fig. 4.2), thus pushing the lower frequency part of the transmission response higher in frequency. This shift in frequency squeezes the passband since the notch frequency is fixed. Similarly, one can push the notch further down in frequency, while keeping the lower part fixed, in order to achieve a narrower response.

Although being less selective, the modified FSS maintains the desired bandpass features required here. In addition to a passband, the FSS response has a transmission zero that provides a fast roll-off at upper band frequencies of the frequency response (see Fig. 4.3). Being a single-sided structure, the new, modified element can be utilized in design of multilayer FSS structures. This surface, as will be discussed below, enables the design of multipole FSS structures with a very low thickness. This will be discussed in the next sections where the design process of multipole FSS structures based on the modified and original, [38], single-pole FSS structures is presented.

4.3 Multipole, Cascaded Frequency-Selective Surface Screens

A common technique in filter theory for achieving a higher-order filter response, as mentioned above, uses a number first-order resonators and have them couple with each other. By tuning the resonators as well as the levels of coupling, the multi-order characteristics of the filter is adjusted.

The multipole characteristics of the miniaturized-element FSS structures, the loop-wire and the modified (above), in a cascaded fashion is studied in this section. Two scenarios are considered here: First, layers of the original loop-wire FSS presented in Chapter 3 are used as the building-blocks of a dual-pole surface. Unlike the FSSs presented in Chapter 3, the layers constructing the multilayer FSSs here are bare circuit-boards without any lumped capacitor. Second, a dual-pole surface is built using two layers of the modified, single-face FSS introduced in the previous section. In a way, the first, two-pole FSS constitutes a frame

of reference (benchmark design) based on which the performance of the modified, dual-pole FSS is evaluated.

4.3.1 Benchmark Design: Multipole Surfaces Based on the Double-Sided, Loop-Wire Surface

Building-Blocks of the Multipole Surfaces: A Capacitor-Free, Loop-Wire Surface

In this section, multipole FSS structures based on an existing (loop-wire) miniaturized-elements FSS layer are considered. As mentioned above, lumped capacitors interconnecting the loops in the FSS design reported in [38] cause inevitable fabrication problems for multi-layer structures. To circumvent this problem, we modified the design slightly to reduce the required, lumped capacitance such that the gap capacitance itself is sufficient to maintain the filter characteristics. In this process, the unit cell size had to be increased from $\lambda/12$ to $\lambda/9$. After eliminating the lumped capacitors, multipole FSS structures can be fabricated easily.

Table 4.3: The Capacitor-Free, Single-Pole Loop-Wire Miniaturized-Element FSSs' Static Design Parameters at X-Band for Free-Space Operation

s	δ	w	t	ε_r	$D_x \times D_y$
0.15 mm	0.15 mm	1.2 mm	0.125 mm	2.2	4.4 mm × 4.4 mm

Table 4.4: The Circuit Model Values for the Capacitor-Free, Single-Pole Loop-Wire Miniaturized-Element FSS

C_g	L_1	L_2	L_3	C_s	K
0.2 pF	0.6 nH	0.42 nH	0.055 nH	69 fF	-0.6

The parameters of the single-pole FSS are listed in Table 4.3. As usual, s is the loop

spacing; δ is the width of the traces of the loops; w is the wire width; and t is the substrate thickness. Fig. 4.4(a) shows the circuit model for this two-face FSS which was previously discussed in Section. 3.3.2 in Chapter. 3. The circuit values are provided in Table 4.4. Using the design values provided in Table 4.3, the two-face FSS was characterized using a full-wave simulator. Similar analysis was performed using a circuit simulator for the case of the circuit model given the parameter values of Table 4.4. Comparison between the HFSS (full-wave)

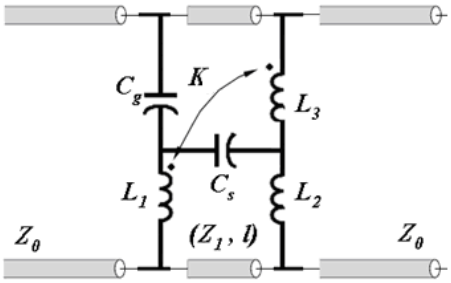

(a)

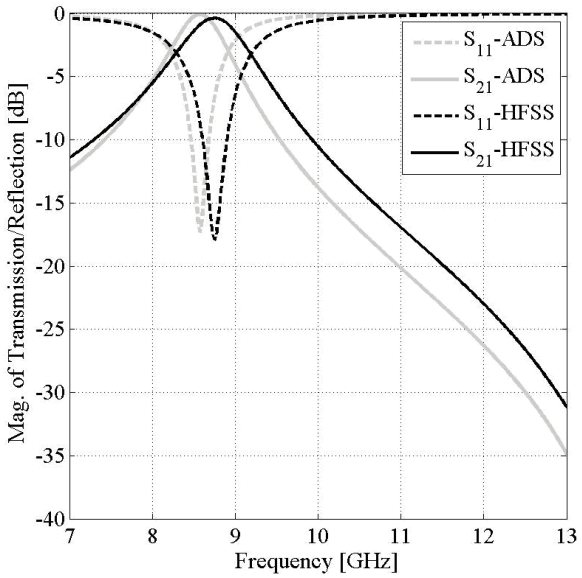

(b)

Figure 4.4: The capacitor-free, single-pole miniaturized-element FSS at normal incidence- (a) The circuit model (b) Full-wave numerical simulations performed using the values of Table. 4.3 are compared with the circuit simulations using the values used in Table. 4.4. A passband and a transmission zero are produced.

simulations and the ADS (circuit model) simulations is demonstrated in Fig. 4.4(b), showing a good agreement between HFSS and ADS.

Optimization and Assembly for a Dual-Pole Operation

The multipole FSSs are constructed in a straightforward fashion by cascading layers of single-pole, loop-wire FSS. A dielectric spacer is also placed between the FSSs. In the multilayer FSS process presented here the only parameters used for optimization are the spacer thickness and the lateral placement of the single-pole FSSs in the stack (multilayer FSS). As will be discussed below, these parameters control the coupling of the building-blocks (single-pole FSSs). The individual layers of FSS have fixed parameters, as listed in Table 4.3, which are not changed in the multilayer design process.

The electrical and physical thickness of the spacer and the lateral position of the FSSs in the stack tune the coupling between the layers. Obviously, increasing the separation distance between two resonators decreases the coupling between them. As a result, spacer thickness controls the magnitude of the mutual coupling coefficients. Moreover, the thickness changes the junction capacitance, if there is any, formed between the layers. The relative lateral position of the layers, as mentioned above, can also manipulate the coupling mechanism. However, such manipulations change the coupling in a more involved fashion. Given the very small size of the unit cell dimensions and the closeness of the layers, a quasi-static approach appears to be adequate to solve the problem. Simply, pairs of inductive traces that are magnetically coupled should be located. Two traces are coupled if one trace intersects the magnetic field of the other trace and vice versa. As a result, we need to have a sketch of the magnetic field distribution in the near-field of each trace. Given the incident wave polarization, the electric current distribution (direction) on the thin traces is known. Given the current direction, the right hand rule can be used to determine the direction of the circulating magnetic field around each trace.

Given the physics of the mutual inductance and the symmetry of the periodic structures (FSS), the magnetic interaction of two metallic FSS screens placed at a close distance to one another can be understood. For example, consider two wire-grids printed on either side of a thin substrate. In one experiment, the layers have no lateral shift, and in another, the wires

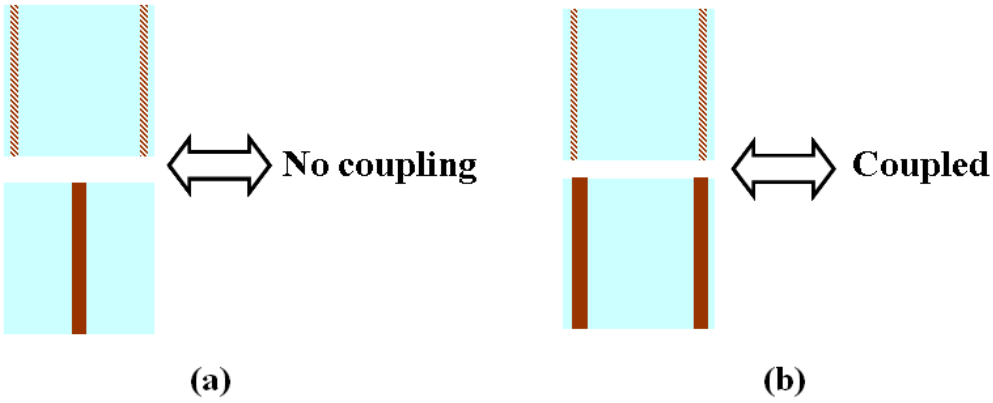

Figure 4.5: The mutual coupling effect of two overlapping metallic grids- The top and bottom sides of the unit cells are shown separately. (a) No coupling is observed if the grids are translated laterally by a half the unit cell size. As shown, the wire shown at the bottom (from the bottom side of the unit cell) is between the two traces from the top side of the unit cell. The top traces have the same electric current distributions because of the symmetry of the periodic, infinite structure. These same currents produce the same magnetic fields in opposite directions at any point on the bottom trace in the middle. As a result, by superposition the overall coupling effects becomes zero. (b) If the wire-grids are right on top of one another, the coupling is maximum.

are translated by half of the period along the two orthogonal directions on the wires' plane. In the first case with completely overlapping wires, the wires are highly coupled, whereas in the second experiment, the layers are uncoupled. This difference can be explained by taking a closer look at the unit cell of these arrangements. The first unit cell has an even symmetry, while the second experiment uses an odd symmetry. Although individual traces are coupled with one another, but the effect of each trace, belonging to a grid, on the opposite grid is canceled by another trace belonging to the same grid. This is demonstrated in Fig. 4.5. It should be mentioned that the coupling is a close-distance effect, and therefore, only traces inside the same unit cell contribute to the coupling of the grids in that unit cell area. In other words, the interaction between different sides of different unit cells in the array is negligible.

As mentioned above, the mutual coupling is the key optimization parameter in the multi-pole circuits provided here as examples of multilayer FSS design. Two dual-pole circuits are demonstrated: 1) the two single-pole FSS screens are translated symmetrically by half of a unit cell size with respect to each other (the center of a unit cell of the FSS sitting on

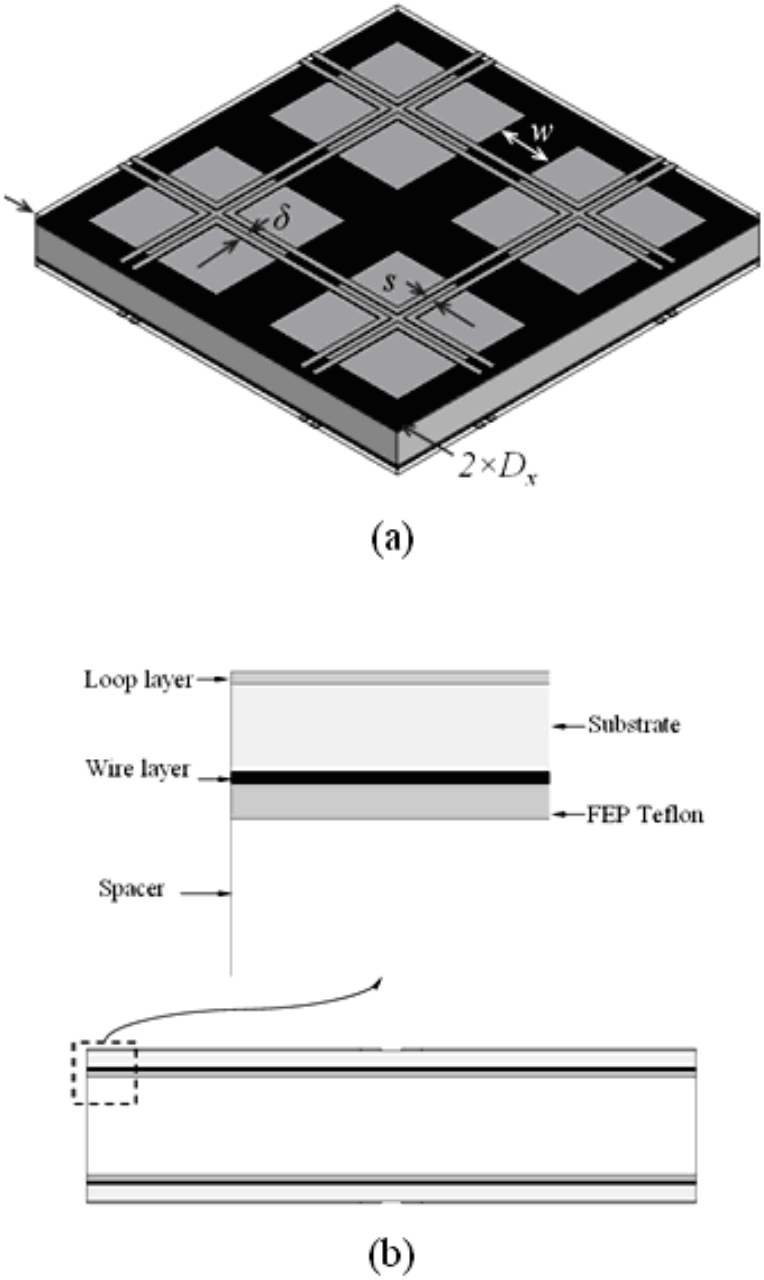

Figure 4.6: Stacked miniaturized-element FSS. (a) Array of four unit cells including two layers of wire grid in black and two layers of loop array in gray. (b) Assembly of the layers in the stack.

top and the corner of a unit cell of the other FSS sitting at the bottom overlap) and 2) the two FSSs are put together without any translation (lateral shift). This way, the variation in the coupling coefficient is used to split the poles to get a dual-band response or to bring

the poles close to each other to produce a maximally-flat response. Fig.'s 4.6(a) and 4.6(a) show the geometry of the unit cell including its parameters for the dual-pole FSSs and the a way the layers of FSS are assembled, respectively As shown in this model, the multilayer structure has a center of symmetry located at the center of the spacer box. For example, both top and bottom layers of the structure are covered with the same loop-arrays.

Modeling and Analysis of the Dual-Pole Surfaces

The dual-pole surfaces introduced in the previous section employ two, same layers of the loop-wire FSS whose circuit model is already known. Two such circuits placed in parallel are expected to be able to model the two-pole FSSs, otherwise the circuit analogy of the FSS structures becomes inconsistent and therefore incorrect. The two circuits must be also coupled with each other in order to account for the effect of closeness of the loop-wire FSSs in the stack. Given the accurate circuit and full-wave simulations, it turned out that the circuits constructed this way to model the dual-pole FSSs are in fact very accurate. Fig.'s 4.7(a) and 4.7(b) show the equivalent circuit models for the dual-pole FSS when the two single-pole FSSs are cascaded with and without a lateral offset, respectively. Each model cascades two circuits which are identical and have been developed previously to describe the single-pole FSS (see Table 4.4 and Fig. 4.4(a)).

The key difference between the cascade models is the magnetic mutual couplings between the elements. As mentioned above, the two-pole FSS has a dielectric spacer which is sandwiched between the two FSSs. Because of the very low thickness of the spacer, the single-pole FSSs (circuits) are coupled with each other. To model the interaction between the FSSs, the two-pole circuits include a new coupling coefficient, K_2, in addition to the elements of the single-pole circuits. These circuits also have other elements accounting for the spacer itself including $Z_1 = Z_0/\sqrt{\epsilon_r}$ and l as the electrical length of the spacer. As shown in the models, the lateral position of the FSSs changes the coupled inductors (K_2) each of which belonging to one of the two single-pole circuits.

The next step is fine tuning the circuit-based design using a full-wave simulator. In this process, the full-wave simulation is employed to find the proper thickness for the spacer in order to produce the required pole-splitting. This thickness, for the dielectric constant of

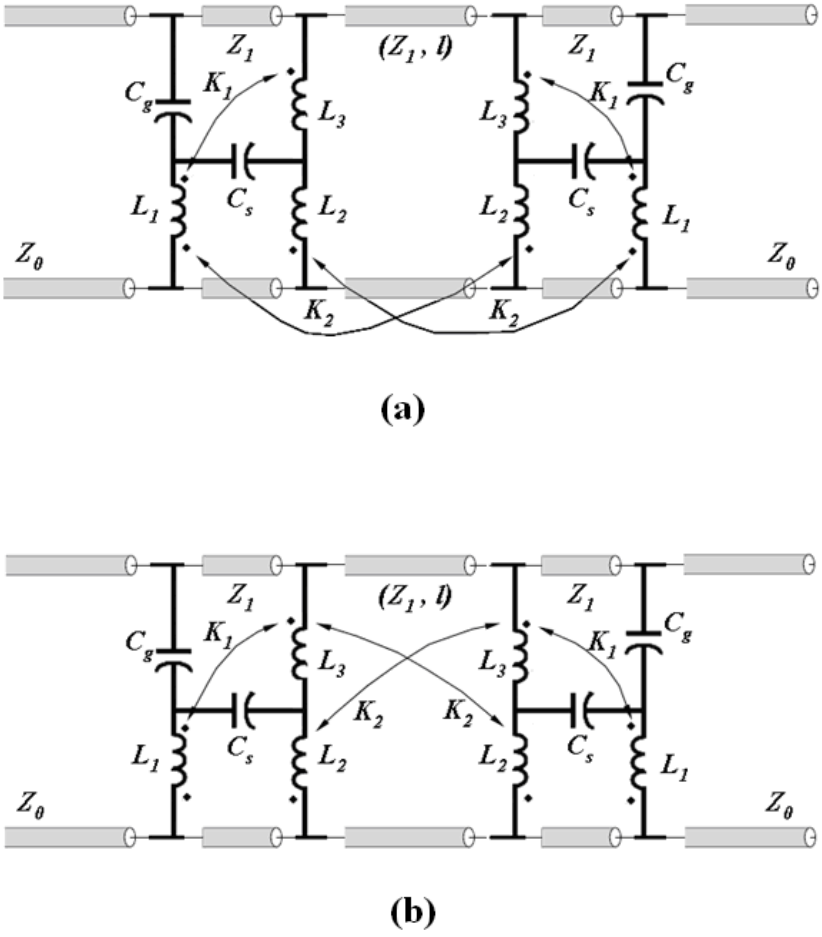

Figure 4.7: Equivalent circuit models of the multilayer, two-pole FSSs based on the single-pole FSS in [38] at normal incidence: (a) The model for the multilayer design whose layers have a lateral translation (half the cell size) with respect to each other. This dual-pole circuit produces a maximally-flat bandpass response. The coupling coefficient between the two FSSs is $K_2 = 0.27$. (b) The model for the multilayer FSS whose layers have no lateral shift with respect to one another. This circuit generates a dual-bandpass response. Coupling coefficient for this circuit is $K_2 = 1$. The transmission line modeling the spacer is the same for both circuits and is characterized by: ($Z_1 = 260\ \Omega$, $l = 9^o$) at 10 GHz.

2.2, was found to be 0.02 in. The comparisons between the ADS simulations of the circuit models and the results of the full-wave model are shown in Fig.'s 4.8(a) and 4.8(b). It should be emphasized here again that in the cascade models, only the elements representing the effects of the spacer (K_2 and l) are tuned to achieve the best fit between the circuit and full-wave results. As demonstrated, the circuit models remarkably predict the behavior of

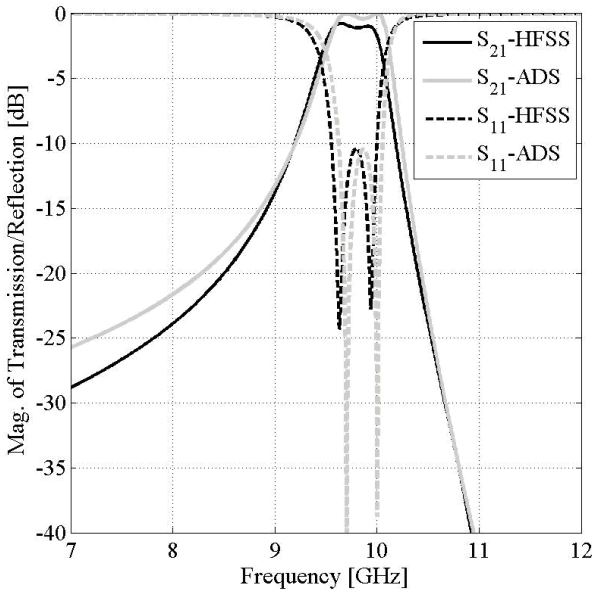

(a)

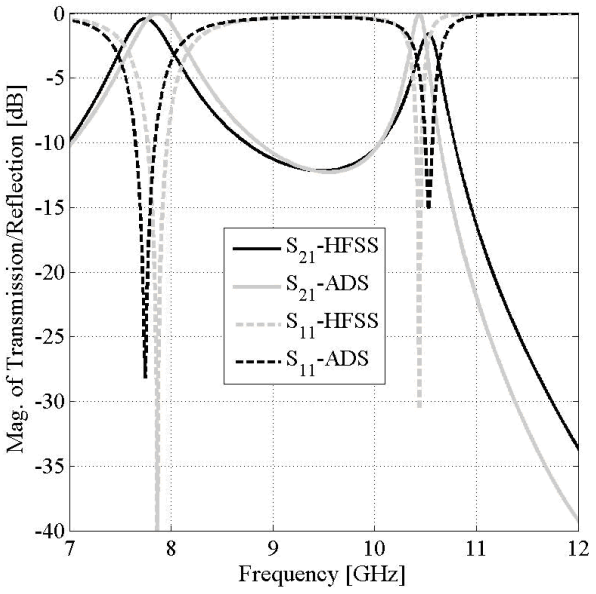

(b)

Figure 4.8: Full-wave numerical simulations for the multilayer, two-pole FSSs based on the single-pole FSS in [38] at normal incidence compared to the results achieved by simulating the circuit models of the FSSs (see Fig.'s 4.4(a) and 4.4(b)). (a) The multilayer design with the lateral shift (half the cell size) - This dual-pole FSS produces a maximally-flat bandpass response. (b) The multilayer design whose layers have no lateral translation with respect to each other- This FSS generates a dual-bandpass response.

the FSS structures in the multilayer fashion, thus showing the consistency of the lumped circuit-modeling approach.

4.3.2 Improved Design: A Multipole Surface Based on the Single-Sided Surface

As mentioned above, our objectives here are reducing the thickness of multipole FSS designs, lowering the complexity and cost of fabrication, and improving the performance. The multipole FSS structures introduced in the previous section are comprised of building-blocks that are two-sided circuit-boards. As discussed previously, this might be impractical for high-order FSS applications where a very low thickness is required. Moreover, the out-of-band rejection for the dual-bandpass design (see Fig. 4.8(b)) is only slightly better than 10 dB, which cannot be further improved without sacrificing the in-band insertion loss.

In Section 4.2, the geometry and behavior of the modified miniaturized-element FSS, as a

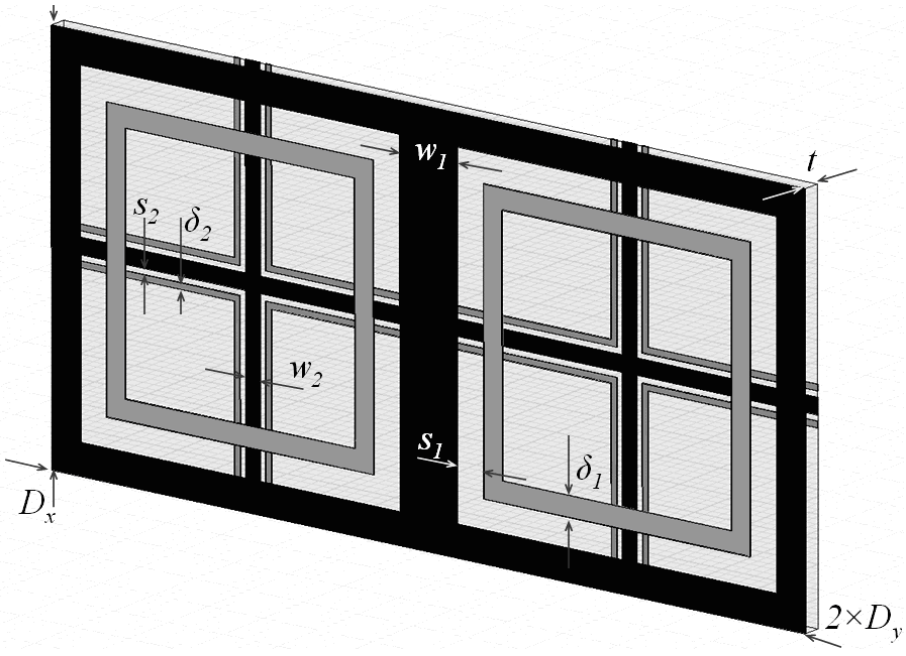

Figure 4.9: Two periods (unit cells) of the dual-bandpass FSS comprised of two modified, single-face miniaturized-element FSSs on either side of a substrate. Index 1 marks the top layer, whereas index 2 is used for the bottom layer. The loops are in gray and the wires are in black.

variation of the loop-wire FSS, was discussed. Through numerical simulations, it was shown that this single-face FSS, similar to the original loop-wire FSS, is able to generate our desired frequency response consisting of a passband and a transmission zero. In this section, the multipole performance of this modified surface is investigated. Similar to the case previous multilayer surfaces, the cascade method is employed to achieve a desired multipole frequency characteristic. The modified FSS is expected to allow for a major reduction in the thickness of the multipole FSS structures. A dual-pole version of modified multilayer FSSs is provided next.

A very thin dual-bandpass surface can be designed by printing two modified layers on either side of a single substrate. A picture containing two unit cells of this dual-pole surface is shown in Fig. 4.9, including the parameters of the structure. For this two-sided arrangement, the overall thickness is only 0.006 in. One side of the substrate is covered with the first modified FSS presented in Section 4.2. The parameters of this layer are provided in Table. 4.2

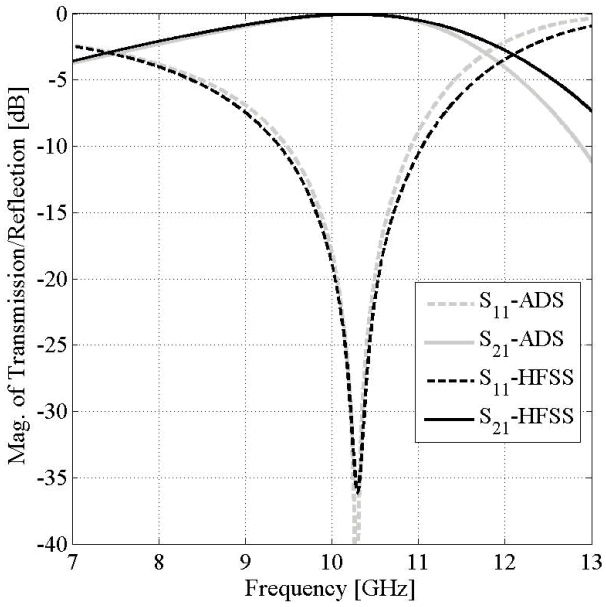

Figure 4.10: The second modified (single-sided) loop-wire miniaturized-element FSS- The physical parameters of this FSS are: $s = 0.48$ mm, $\delta = 0.34$ mm, $w = 0.54$ mm, $t = 0.125$ mm, $\epsilon_r = 2.2$, and $D_x = D_y = 6.9$ mm. Full-wave simulations are well predicted by the circuit model simulations. The values of the parameters of the circuit model shown in Fig. 4.2 are: $C_g = 0.1$ pF, $L_1 = 2.6$ nH, $L_2 = 2.6$ nH, $K = 0.05$, and $Z_o = 377\ \Omega$

above. For the other side, another modified FSS is used which has different values for its structure parameters. This layer is named the second modified FSS. The frequency response of this FSS is shown in Fig. 4.10 which also includes the values of both physical parameters and the circuit model parameters of the FSS. As demonstrated in Fig. 4.9, the two layers are laterally shifted with respect to one another by half of a unit cell in both $\hat{x}$ and $\hat{y}$ directions.

The simulation results for the dual-pole FSS made up of the two single-face FSS structures are shown in Fig. 4.11, demonstrating a remarkable improvement in terms of the out-of-band rejection compared to the benchmark FSS. Similar to the previous multilayer FSSs, equivalent circuit model for this two-pole FSS can be simply obtained by cascading the circuit models of its individual layers (the two modified FSSs) and incorporating appropriate coupling coefficients into the circuit to model the interactions between the layers. Given the small distance between the layers, the two single-sided FSSs used in this design are highly coupled. The new elements accounting for the coupling of the layers are K_3, K_4, and K_5

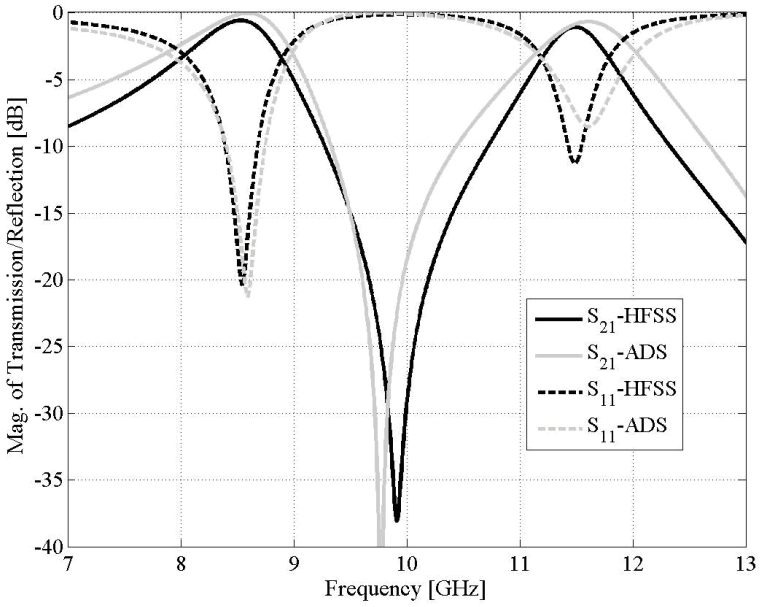

Figure 4.11: Full-wave numerical simulations for the two-pole FSSs based on the single-pole, single-face FSS at normal incidence compared to the results achieved by simulating the circuit model of the FSSs. This dual-pole FSS produces two passbands and two transmission zeros.

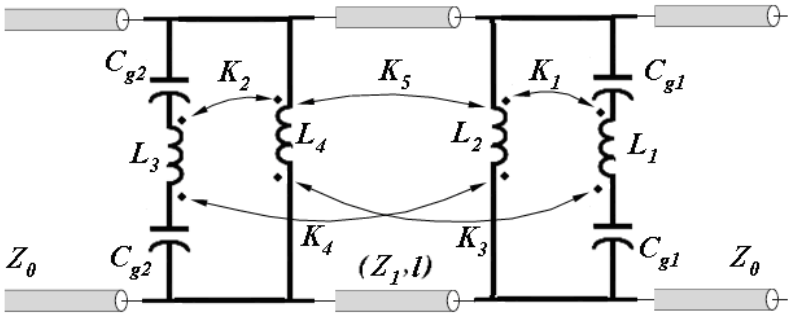

Figure 4.12: Equivalent circuit models of the two-pole FSSs based on the single-pole, single-face FSS at normal incidence- The right half of the circuit is the first single-face whose values are provided in Table. 4.2, whereas the left half of the circuit is the second single-face FSS with parameters shown in Fig. 4.10. The coupling between the two single-pole circuits (single-face FSSs) is shown through the coefficients K_3 = 0.1, K_4 = -0.05, and K_5 = 0.15. The substrate is characterized by: (Z_1 = 260 Ω,l = 10^o) at 10 GHz.

, as shown in the circuit model (Fig. 4.12). Using exactly the same values provided above for the circuit models of the layers, this circuit well predicts the full-wave simulation results (see Fig. 4.11). It should be emphasized again that this dual-band FSS is six times thinner than the four-layer, dual-band FSS (benchmark) shown above.

4.4 Measurement

The FSS structures based on the benchmark design and the proposed improved design were fabricated by the standard commercial etching of 1/2 Oz. copper on 0.005-in-thick Arlon, [112], DiClad 880 substrate (ϵ_r = 2.2, $\tan\delta_c$ = 9E -4). For the benchmark design, two single-pole, 6-in × 6-in, loop-wire FSS screens, without lumped capacitors, were stacked together with a spacer (0.02-thick substrate of the same kind) that was placed between the two screens. The FSS layers and the spacer were then bonded together by a 0.001-in-thick FEP Teflon. The overall thickness in the dual-pole arrangement is $\lambda/40$. Fig. 4.6(b) shows the assembly drawing. As shown, a dual-pole version of this design type has four printed layers. One of the fabricated benchmark, dual-pole FSSs is shown in Fig. 4.13. The improved dual-band design presented in the previous section was also fabricated using a single DiClad

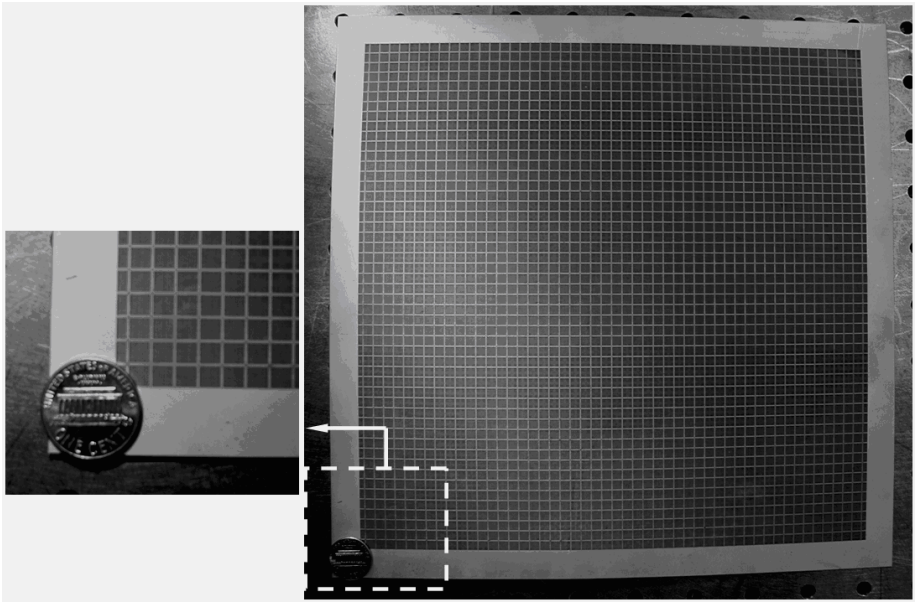

Figure 4.13: Dual-pole, benchmark FSS fabricated using the standard etching process for a free-space transmission measurement- The picture shows the design with the maximally-flat response.

880 substrate. The fabricated surface, which is only $\lambda/240$ in thickness, is shown in Fig. 4.14.

Through a standard transmission measurement in the free-space environment, the performance of each multipole surface was tested. The measurement setup consists of a lens-corrected horn antenna for creation of a uniform phase front over a finite aperture, and a high-gain antenna in the far-field. The surface is placed adjacent to the lens-horn, and the receiving antenna is in the far-field region of the horn and the surface [38].

The measurement result for the benchmark, stacked FSS with laterally offset layers is shown in Fig. 4.15. This FSS, as shown, has a maximally-flat, two-pole bandpass frequency response with a high-frequency roll-off rate of 40 dB/GHz. The measured result, compared with the simulation, for the dual-band benchmark FSS with no offset is provided in Fig. 4.16. The measured transmission coefficient validates the simulations, exhibiting two passbands in the frequency band of 7–12 GHz. The performance of the modified, dual-band design is provided in Fig. 4.17. As shown, the selectivity is improved with a reduced number of metallic layers compared to the benchmark, dual-band FSS. The agreement between the

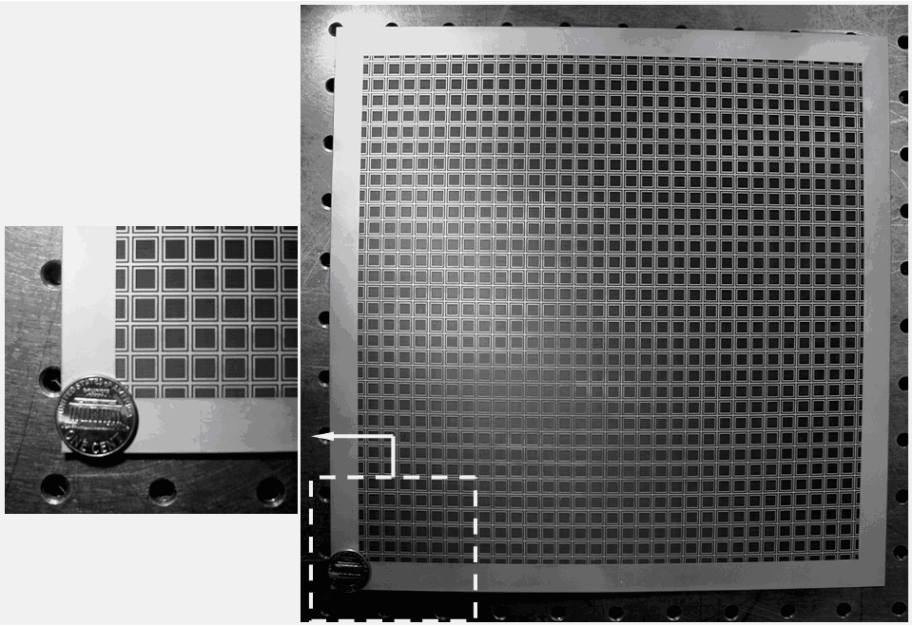

Figure 4.14: Modified dual-pole FSS fabricated using the standard etching process for a free-space transmission measurement.

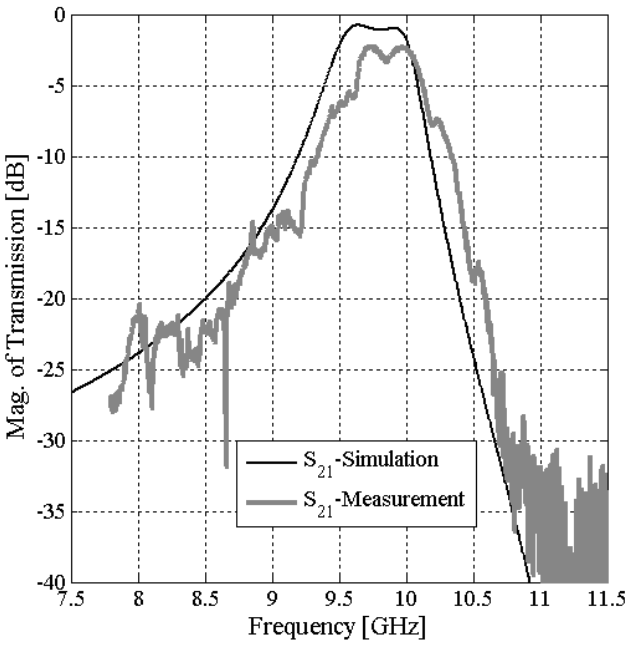

Figure 4.15: Measurement against simulation- Dual-pole, maximally-flat, benchmark FSS with the thickness of $\lambda/33$ (Fig. 4.8(a)).

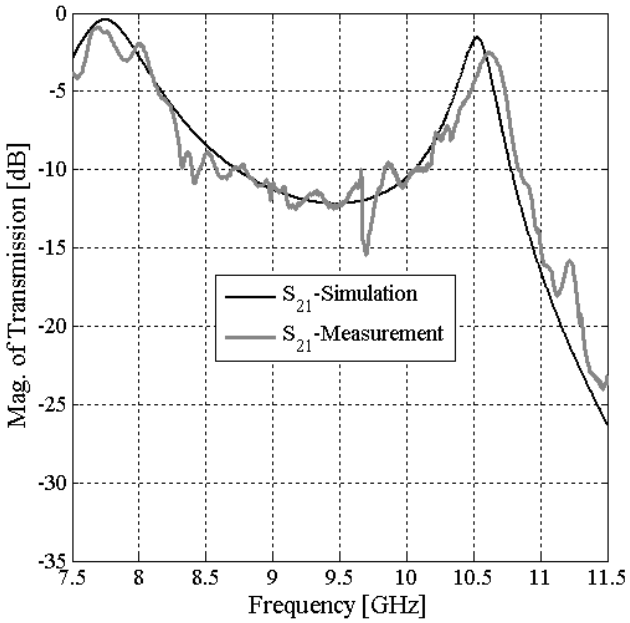

Figure 4.16: Measurement against simulation- Dual-bandpass, benchmark FSS with the thickness of $\lambda/33$ (Fig. 4.8(b)).

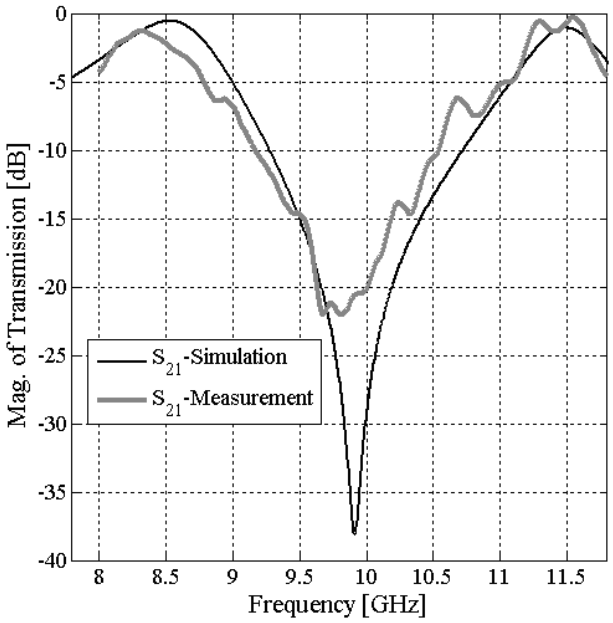

Figure 4.17: Measurement against simulation- Dual-bandpass, improved FSS with the thickness of $\lambda/240$ (Fig. 4.11).

simulations and the measurements verifies the accuracy of the design process.

4.5 Chapter Conclusions

A new, bandpass miniaturized-element FSS is studied as the building-blocks for multi-bandpass FSS structures. Two design approaches are considered, which are: 1) a benchmark design using previously designed FSS layers that achieves multipole behaviors by cascading the layers separated by dielectric slabs and 2) a very thin design based on a cascaded, new miniaturized-element FSS that uses a single-sided circuit-board. Despite having a simple and straightforward design process, the first multipole FSS is rather thick (0.037 in for a dual-pole surface) with a relatively poor out-of-band rejection in the dual-band arrangement. The dual-pole FSS of the second type, in contrast, has a thickness of only 0.006 in, which is six times thinner compared to the first type. Prototype samples of both types were fabricated, and performance of each design was tested against experiments. It is shown that much higher out-of-band rejection can be achieved using the second approach.

CHAPTER 5

Fully Reconfigurable Miniaturized-Element Frequency-Selective Surfaces

A reconfigurable miniaturized-element frequency-selective surface is presented in this chapter [105]. A standard waveguide measurement setup is used to evaluate the performance of the design. The proposed FSS consists of two periodic arrays of metallic loops, with the same periodicity, on either side of a very thin dielectric substrate. The tuning of the reconfigurable surface is shown numerically to be possible by incorporating tuning varactors into the structure. Using varactors on both layers, a reconfigurable frequency response is achieved, which has two modes of operation: bandstop and bandpass. In addition to two completely different modes of operation, the center frequency, as well as the bandwidth of the response can be tuned independently. Frequency tunability with a constant bandwidth over 3–3.5 GHz is shown. A bandwidth tuning at a fixed center frequency is also demonstrated. Simulation results are verified experimentally by fabricating prototypes of the design at S-band loaded with lumped capacitors. To demonstrate the tunability, different pairs of fixed-valued capacitors, as opposed to varactors, are used in a waveguide measurement setup to avoid difficulties associated with biasing varactors in the waveguide.

5.1 Chapter Introduction

Frequency-selective surfaces (FSSs) that provide spatial filtering have been widely used for radar and satellite communications [1–3, 39, 41]. FSS applications in radar primarily

concern radar cross-section (RCS) reduction, whereas applications in wireless concern RF interference (RFI) mitigation. With the advent of multifunctional systems, the need for spatial filters having agile frequency characteristics is on the rise. Here, frequency agility refers broadly to tunability for band selectivity and change in filtering function (e.g., change from bandpass to stopband, etc.), and hence the name reconfigurable FSS. Tunable frequency filters have been the subject of research over the years. Besides mechanical tuning, a common approach for tuning is based on solid-state varactor diodes [98–101], which construct an electronically tunable filter. Reconfigurable FSS surfaces usually use a similar approach; either microelectromechanical systems (MEMS) capacitors [95, 96] or varactors [104] are incorporated into a traditional FSS structure to achieve tunability over a narrow bandwidth.

In Chapter 3, a metamaterial-based FSS proving a high-order bandpass characteristic was proposed. This FSS, which is composed of a thin substrate supporting an array of sub-wavelength periodic loops on one side and a wire-grid on the other side, was shown to have a passband with a transmission zero frequency response [38]. Important features of the metamaterial FSS are: 1) insensitivity of frequency response to the angle of incidence and 2) having a harmonic-free frequency response. It was also shown that the frequency response can be tuned by placing a varactor between each pair of neighboring loops in the array. Altering the capacitance of the varactors tunes the frequency of transmission zero, thus sweeping the response in frequency [82]. This design, however, does not allow for a simultaneous control over both center frequency and bandwidth, as there is only one degree of freedom (transmission zero). The frequency response also cannot be changed from a bandpass to a none-pass if so desired.

A reconfigurable miniaturized-element FSS is presented in this chapter in which not only the bandwidth and the center frequency can be separately tuned, but also the response can be transformed from bandpass to stopband [105]. This FSS has two arrays of loops printed on either side of a thin flexible substrate. The tunability of the design can be achieved by connecting the loops on each layer by varactors. In the following, the design procedure and physical insight into the structure behavior are first presented. It will be shown that the response of this FSS comprise two transmission zeros (two degrees of freedom), which enable a very flexible frequency tuning. The results of a waveguide measurement are then compared

to the numerical simulations to show the validity of the design procedure.

5.2 Design Approach

In this study, a tunable spatial filter whose frequency response can be switched between bandpass and stopband is presented. The design approach begins with developing a realizable concept for the desired reconfigurable FSS. It will be convenient if the filter response be realizable from modular components to generate the desired frequency response over sub-regions. This decomposition will allow structures associated with each sub-region be designed and then brought together to make the desired filter response. In the following, an approach is presented that allows an FSS to have variations in its mode of operation.

Consider a frequency response consisting of a passband region and two transmission zeros (notches). The center frequency of the passband region is chosen to be between the notch frequencies. Depending on the center frequency, as well as the positions of the notches, the overall response can have two different shapes. In a normal case where the notch frequencies and the center frequency are different, a bandpass response is specified. The bandwidth of this response depends on the frequency separation between the notches (passband region remains between the notches). In a sense, the difference between the notch frequencies controls the bandwidth of the passband; the closer the notches, the narrower the bandwidth. In addition to the bandpass shape, this frequency response can have another shape. Instead of being different, if the notch frequencies overlap, the passband region disappears. In this case, the response becomes a single notch.

The approach described above is taken in constructing a multimode spatial filter; assuming the notches being independently tunable, the resulting response can be switched between bandpass and bandstop modes. In the bandpass mode, in addition, by tuning the notch frequencies simultaneously, the FSS response can be swept over the frequency. Since the notches can be tuned independently, this frequency tuning approach offers the opportunity to control the bandwidth independent of the center frequency. In the following, the synthesis of such a response is described.

A miniaturized-element FSS design was recently introduced in [38]. This structure is

composed of two layers: an inductive wire-grid and an array of metallic loops. The array of miniaturized loops, in isolation, has been shown to have a stopband characteristic. By inserting lumped varactors in the gaps between the loops, a tunable notch response can be produced. By cascading two such loop layers, a filter structure having two notch frequencies in its response is expected. This structure has the potential to behave as a reconfigurable FSS. As will be discussed below, a high-order bandpass characteristic can be obtained by placing these layers very close to each other and establishing the proper coupling among the loops on both sides of the substrate.

5.3 Design Specifications and Modeling

The reconfigurable FSS presented in this chapter is composed of two loop arrays. These arrays are fabricated on either side of a substrate, thus constructing two parallel notch layers. Each array by itself acts as a bandstop spatial filter. Given the reflective characteristic of

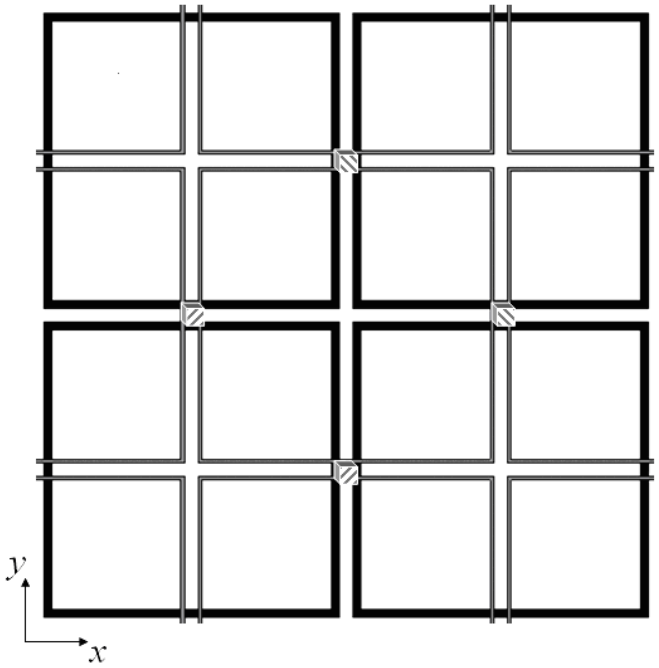

Figure 5.1: Reconfigurable FSS- Four-unit cells are shown; the gray loop array and the black one are printed on opposite sides of the substrate. Varactors are marked by zebra-striped squares (crossing points).

the loop layers, other coupling mechanisms are needed to act in conjunction with loop arrays to produce a bandpass response.

In the FSS design presented in [38], the proper coupling between the FSSs layers is achieved by changing the separation distance of the layers (substrate thickness) and the way the two sides are overlaid. It was shown that the thinner the substrate is, the larger the coupling coefficient becomes, which results in higher -factor resonators. The relative position of the layers, on the other hand, is responsible for pairing up the coupled inductive traces over the two layers. In other words, the lateral position of the layers with respect to each other determines which traces are coupled.

A similar approach is taken here to construct the reconfigurable FSS. The coupling between the loop layers is used to achieve a high-order effect needed to improve the passband characteristics of the FSS. Four unit cells of the FSS (two overlapping loop arrays) are shown in Fig. 5.1. The layers are translated laterally half a unit cell size with respect to each other in both orthogonal directions ($\hat{x}$,$\hat{y}$). To increase the influence of the coupling, a 0.005-in-thick laminate is used for fabrication. For tuning, each array is loaded with varactors interconnecting each two consecutive loops in both $\hat{x}$ and $\hat{x}$ directions at the crossing point of the

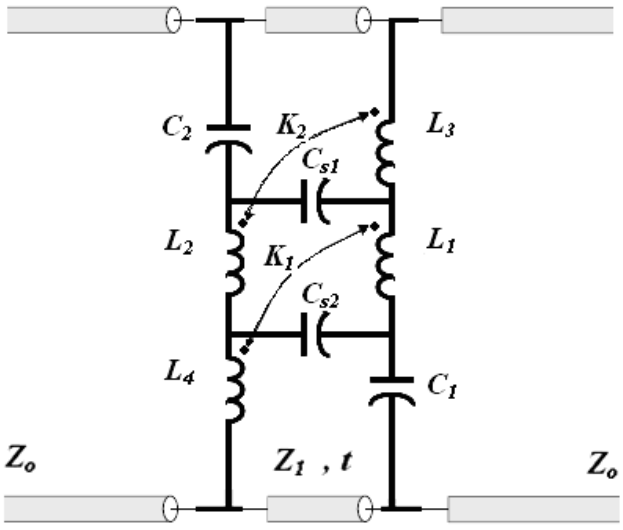

Figure 5.2: Equivalent circuit model of the reconfigurable FSS consisting of two parallel notch circuits that are coupled with each other through magnetic effects and capacitive junctions.

loops of one side and those of the other side. For modeling of the operation mechanism of the FSS described above, a circuit model is introduced below.

A circuit model is a useful tool to describe the behavior of FSS structures that operate in a quasi-static regime (metamaterial-based FSSs). One important feature of the miniaturized-element FSS structures is that, unlike the traditional FSSs, they have equivalent-circuit models. This drastically simplifies the design procedure. The equivalent-circuit model for the loop-array is a series $L-C$ circuit [83]. The inductor in this model represents the inductance of the loops traces, and the capacitor models the gap between adjacent loops. Having two parallel loop arrays, reconfigurable FSSs model essentially consists of two series $L-C$ branches, each representing one layer. A schematic of the circuit is provided in Fig. 5.2. As shown, the circuit model has more elements than just two parallel series $L-C$s. This is due to the close proximity of the layers, which establishes electric and magnetic coupling mechanisms between them. As discussed in Chapter. 3, the layers interactions (mixture of electric and magnetic) are represented by series junction capacitors (C_{s1} and C_{s2}) and magnetic mutual couplings (K_1 and K_2). The series capacitors are expected to form at the crossing points between the two layers. The magnetic coupling coefficients also represent the magnetic interaction of the metallic traces of opposite sides. The choice of the coupled pairs, as mentioned earlier, is based on the lateral position of the layers, as well as the symmetry of the structure.

5.4 Measurement and Numerical Simulation Results

In this section, an optimization process using the equivalent circuit model and a full-wave simulator is used to obtain a reconfigurable FSS for operation in the free-space environment. To verify the design approach experimentally, prototypes of the surface are fabricated and tested. For the experiment, the FSS structure is adapted to a waveguide measurement setup at S-band [82]. This is due to the difficulties associated with the fabrication of a large-scale free-space version of the surface, which requires a few thousands of lumped capacitors.

5.4.1 Free-Space Numerical Simulations

To explore the feasibility of the approach, typical values are assigned to the circuit model elements to test the expected frequency response of the surface, assuming the validity of the model. Circuit simulations using ADS exhibit a bandpass frequency response composed of two transmission zeros on either side of the passband. Next, to achieve operation at S-band, the full-wave simulations using Ansofts HFSS are used to arrive at geometrical parameters shown in Table. 5.1. In this table, δ denotes the width of the traces, s refers to the gap width between the loops, t is the substrate thickness, and (D_x,D_y) are the periodicity along $\hat{x}$ and $\hat{y}$ directions, respectively. Subscripts 1 and 2 are the indices of the layers.

The FSS design also includes choosing appropriate capacitance values that are incorporated into the design as surface-mount capacitors interconnecting the loops. Using capacitors $C_1 = 0.12$ pF (layer 1) and $C_2 = 0.4$ pF (layer 2), full-wave and circuit simulations are performed. The reconfigurable FSS generates a bandpass response including two transmission zeros, which is well predicted by its circuit model, as demonstrated in Fig. 5.3). The values

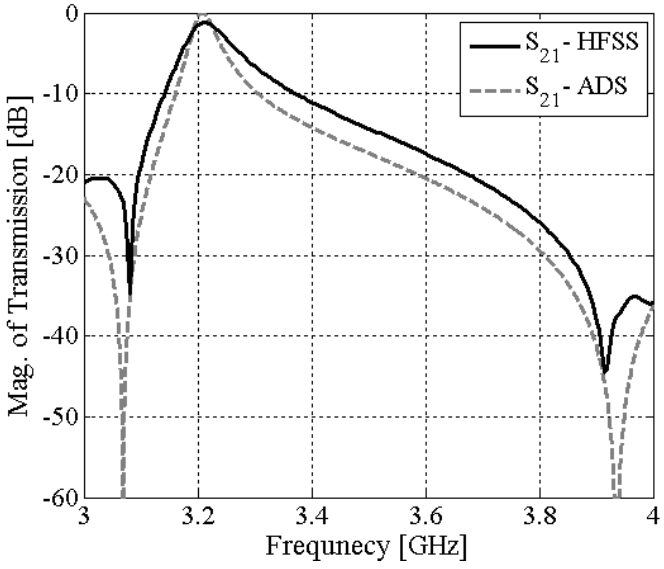

Figure 5.3: Free-space simulations of the reconfigurable FSS using periodic boundary condition (PBC) setup in HFSS at normal incidence compared to ADS circuit simulations. A reference bandpass frequency response is achieved with $C_1 = 0.12$ pF and $C_2 = 0.4$ pF. In this model $Z_0 = 377\ \Omega$ and $Z_1 = 260\ \Omega$

Table 5.1: Reconfigurable FSS's Static Design Parameters at S-Band for Free-Space Operation

s_1 , s_2	δ_1	δ_2	t	ε_r	$D_x \times D_y$
0.45 mm	0.125 mm	0.275 mm	0.125 mm	2.2	10.5 mm × 10.5 mm

Table 5.2: The Circuit Model Values for the Reconfigurable FSS at S-Band for Free-Space Operation

L_1	L_2	L_3	L_4	K_1	K_2	C_{s1}	C_{s2}	C_{t1} ($=C_{g1}+C_1$)	C_{t2} ($=C_{g2}+C_2$)
10.26nH	5.37nH	0.97nH	0.51nH	0.13	-0.93	10fF	27fF	0.139pF	0.413pF

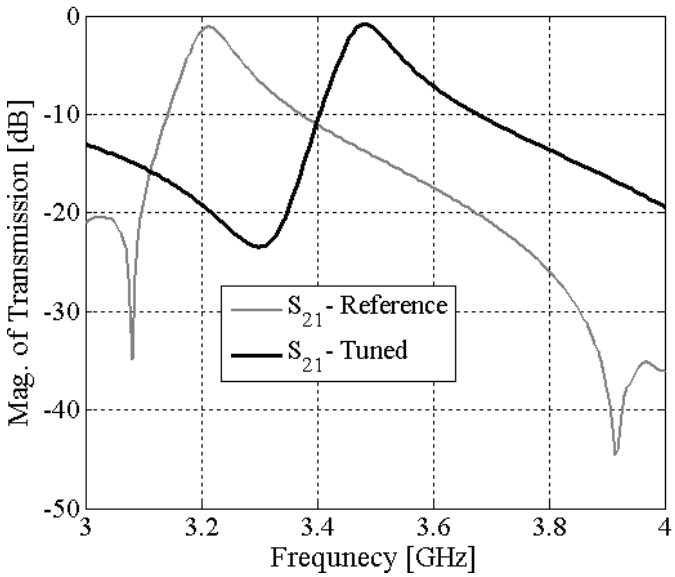

Figure 5.4: Free-space simulations of the reconfigurable FSS using periodic boundary condition (PBC) setup in HFSS at normal incidence. The center frequency tuning from 3.21 to 3.48 GHz, with a fixed bandwidth, compared with the reference response (Fig. 5.3) is achieved with $C_1 = 0.2$ pF and $C_2 = 0.1$ pF.

of the circuit elements are shown in Table. 5.2. These values are the result of a curve-fitting process using ADS to get the best fit between the circuit response and the HFSS response.

To show the tunability, the same surface with parameters listed above is loaded with different pairs of lumped capacitors. These values are achieved by gradually changing capacitances C_1 and C_2 from their reference values (Fig. 5.3) to get the desired response form. The capacitances are chosen in order to demonstrate three different cases, which are: 1) to change the center frequency of the passband while keeping the bandwidth fixed, $C_1 = 0.2$ pF and $C_2 = 0.1$ pF are chosen (see Fig. 5.4); 2) to change the bandwidth while the center frequency is kept fixed, $C_1 = 0.1$ pF and $C_2 = 0.45$ pF are chosen (see Fig. 5.5); and 3) to transform the response from a bandpass shape to a notch, $C_1 = 0.25$ pF and $C_2 = 0.28$ pF are used (see Fig. 5.6).

Although only specific bandwidths and center frequencies are provided above, almost any desired response (in terms of bandwidth and frequency of operation) can be achieved by appropriately choosing the values of the capacitors (C_1,C_2). An important practical issue

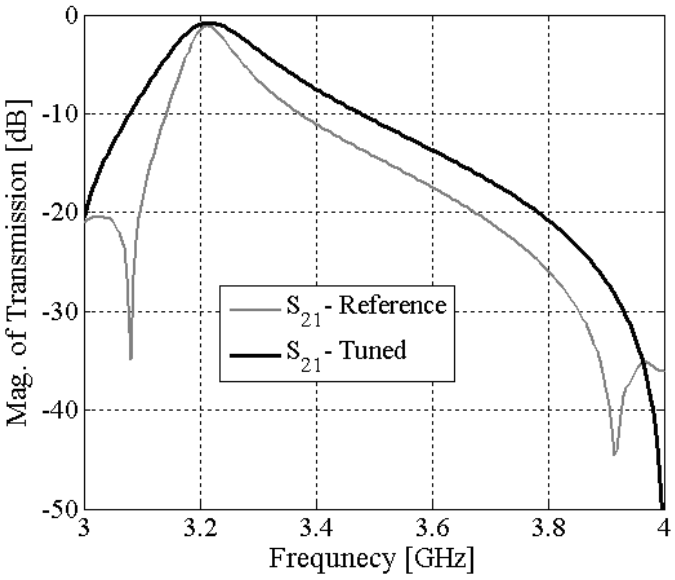

Figure 5.5: Free-space simulations of the reconfigurable FSS using periodic boundary condition (PBC) setup in HFSS at normal incidence. The bandwidth tuning from 90 to 160 MHz , with a fixed center frequency, compared to the reference response (Fig. 5.3) is achieved with $C_1 = 0.1$ pF and $C_2 = 0.45$ pF.

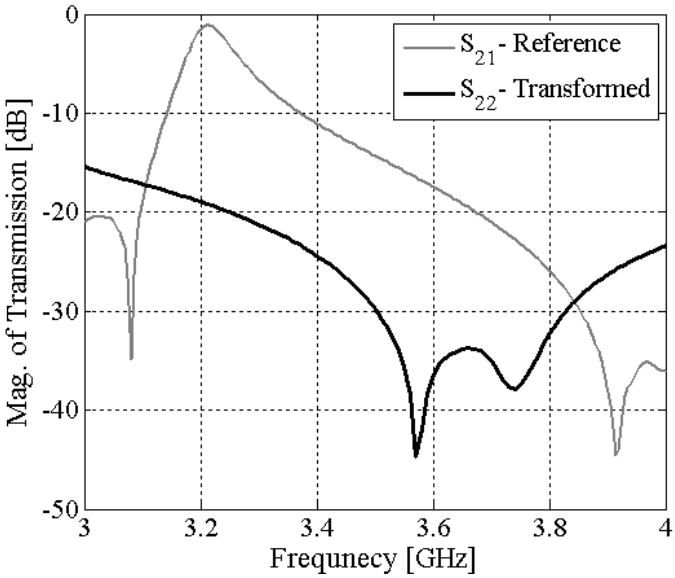

Figure 5.6: Free-space simulations of the reconfigurable FSS using periodic boundary condition (PBC) setup in HFSS at normal incidence. A response transformation compared with the reference response (Fig. 5.3) is achieved with $C_1 = 0.25$ pF and $C_2 = 0.28$ pF.

here is the capacitance range that can be achieved by a varactor. The design presented in this chapter takes into account this issue by manipulating other design parameters so that a practical capacitance range from 0.1 to 1 pF is sufficient to produce desired frequency responses.

5.4.2 Waveguide Measurement and Simulations

As mentioned earlier, fabrication of the reconfigurable surface for free-space testing is rather costly. An alternative inexpensive approach is testing in a rectangular waveguide environment. For this measurement, the dimensions of the FSS screen need to be the same size as the waveguide aperture, as this FSS covers the opening of a waveguide section. Another waveguide section then covers the other side of the FSS to create an isolated waveguide path with an FSS in the middle of the path. To measure the -parameters, the waveguide sections are connected to a calibrated vector network analyzer.

Given the frequency of operation of the reconfigurable FSS (≈ 3.2 GHz), WR-284 standard waveguides are used for the measurement. To fit the FSS appropriately in the standard

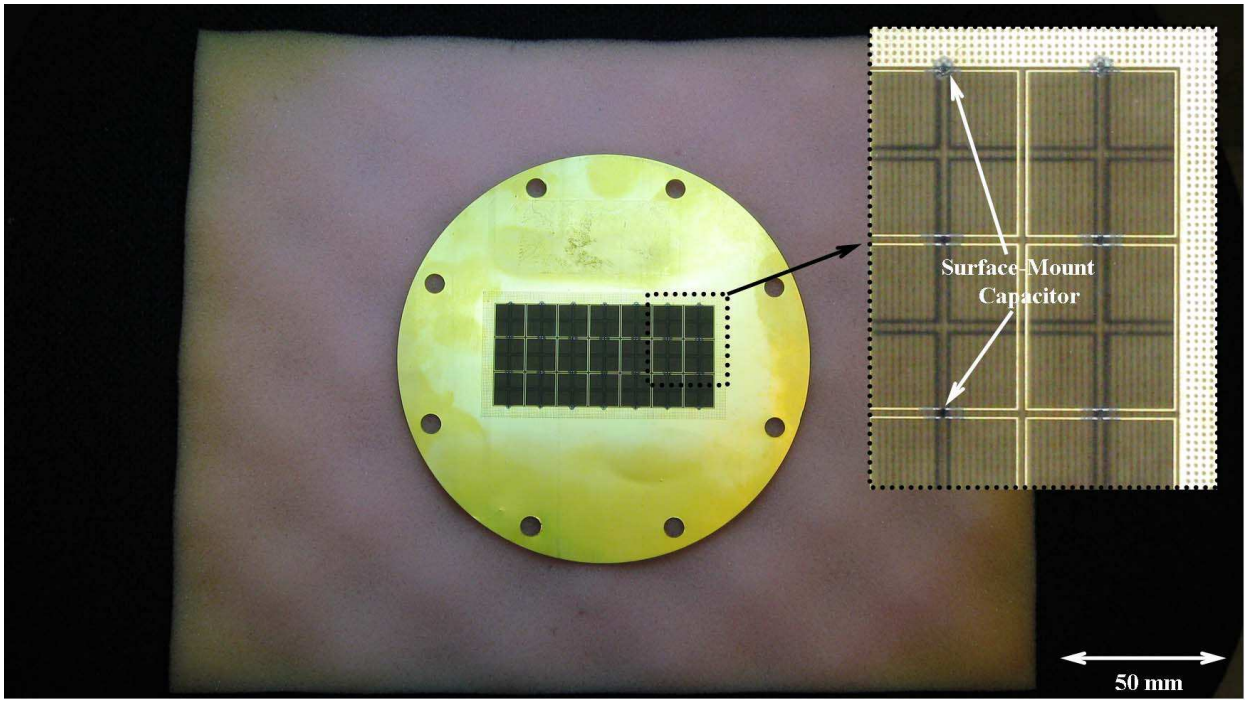

Figure 5.7: Waveguide prototype of the reconfigurable FSS compatible with WR-284 standard flange size.

waveguide [82], the unit cell dimensions (D_x,D_y) are changed slightly from their original values (Table. 5.1) to D_x = 10.3 mm and D_y = 11.3 mm. An 8720D network analyzer is used in this measurement, which is accurately calibrated using a full two-port calibration kit. The range of validity of this calibration is 3–3.5 GHz. A prototype of this circuit is fabricated through a standard etching of copper on a 0.005-in-thick Taconic, [113], TLY5 substrate (Fig. 5.7). The two same circuit-boards are then loaded with two different pairs of capacitors; one pair for producing a bandpass response (C_1 = 0.35 pF, C_2 = 0.1 pF), and another pair for generating a notch (C_1 = 0.3 pF, C_2 = 0.35 pF). The AVX, [114], Accu-P capacitors (size 0201) used for fabrication have Q-factors ranging between 130-170 (depending on the capacitance value) at S-band. Having new periodicities, (D_x,D_y), the entire FSS screen is simulated carefully in waveguide considering the substrate, copper, and capacitors' losses.

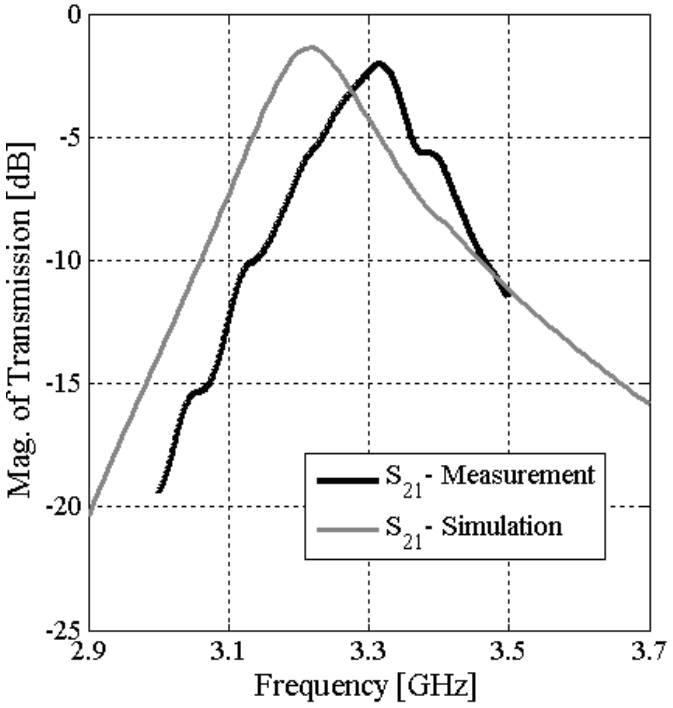

Figure 5.8: Measurement versus simulation in waveguide. This prototype shows the bandpass characteristics of the reconfigurable FSS using $C_1 = 0.35$ pF and $C_2 = 0.1$ pF. The low insertion loss in the simulation is the result of a small mismatch and the capacitor loss.

The measured results compared to the waveguide simulations are provided in Fig's. 5.8 and 5.8, showing a good agreement between the simulation and measurement. As predicted by simulations, the performance of the reconfigurable FSS is well preserved in the waveguide. This is important, as the waveguide environment is rather different than free space. Two major differences with testing an FSS in waveguide are the waveform and the incidence angle of the incoming wave upon the surface. In waveguide, the FSS is excited with a wave (TE_{10}) that consists of two plane waves whose incidence angles are changing with frequency from almost normal to very steep angles. Therefore, a lower performance compared to the free-space case is expected. Specifically, this affects the insertion loss and bandwidth, as the FSS was not optimized for waveguide operation. The point of validation here is to show agreement between the simulation and the measurement.

The 3 percent offset observed in the center frequency of the measured response, shown in Fig. 5.8, is well within the tolerance of the AVX capacitors (± 0.02 pF). The simulated

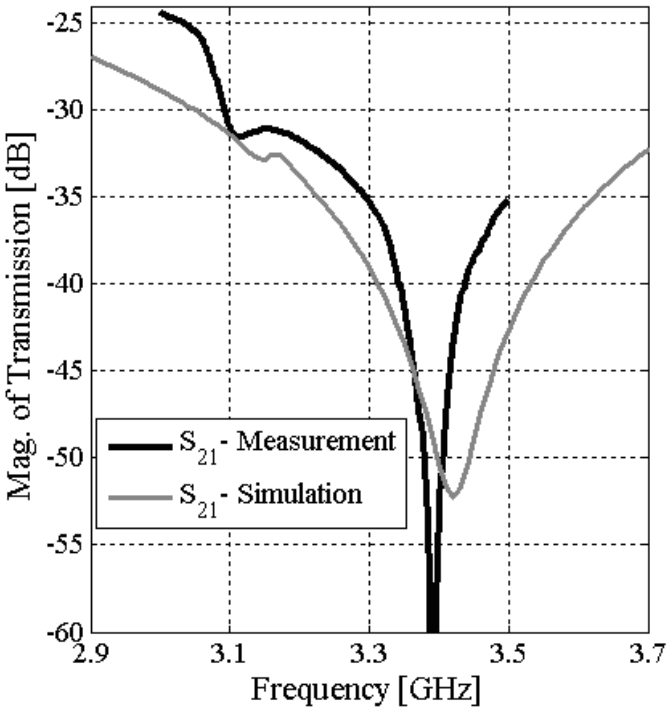

Figure 5.9: Measurement versus simulation in waveguide. This prototype shows the stopband characteristics of the reconfigurable FSS using $C_1 = 0.3$ pF and $C_2 = 0.35$ pF. The frequency shift is very likely because of the ± 0.02-pF tolerance of the capacitors.

waveguide insertion loss of 2 dB is much higher than the expected insertion loss of 0.7 dB of the same surface for the free-space operation (see Fig. 5.3). The narrower bandwidth in the measured response of the stopband (Fig. 5.9) is attributed to tolerances of the lumped capacitors, fabrication tolerances, and S_{21} calibration accuracies. It should be pointed out that Fig. 5.9 is comparing very small quantities.

5.4.3 Free-Space Tunable Prototype Setup

In this section, the construction of the tunable FSS (loaded with a varactor) for operation in a free-space environment is discussed. Unlike waveguide measurement, tunability test in the free-space environment is rather easier and can be done using a simple resistive bias network. A portion of the loop-array loaded with varactor diodes and biasing resistors is provided in Fig. 5.10. The bias network uses the metallic loops as its circuitry, and therefore,

no additional traces are needed. A surface-mount resistor with a proper value is placed in parallel with each varactor. A regulated dc voltage source is then connected to the loop in top-left corner. Finally, the loop sitting in the opposite side (bottom-right corner) is grounded. To avoid disturbing RF operation of the FSS, RF chokes are used to make connections between the FSS and source/ground.

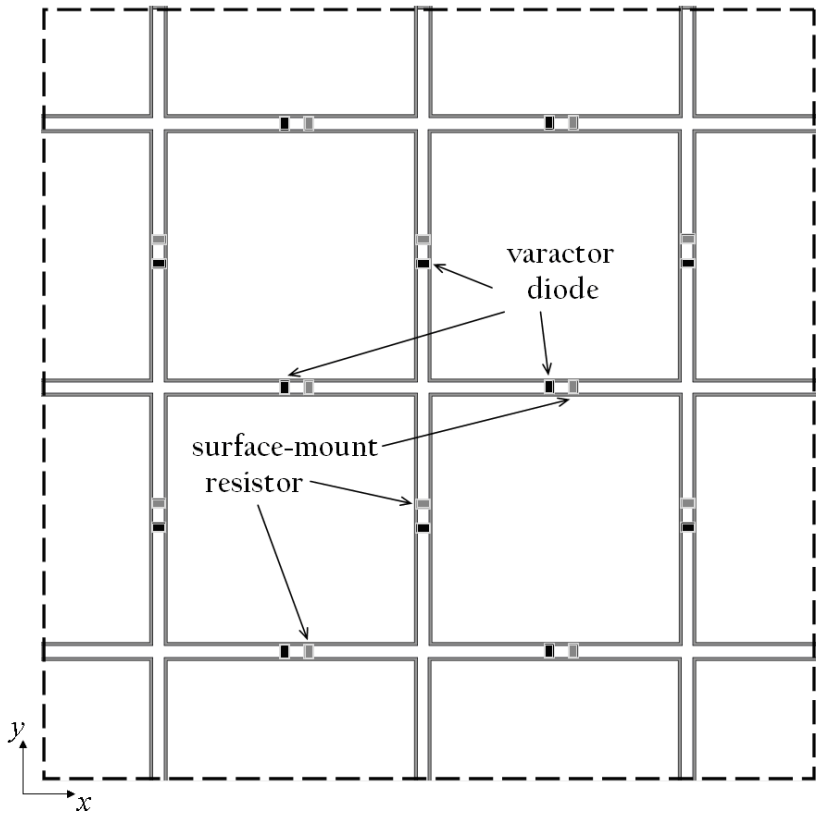

Figure 5.10: Tunable FSS assembly for free-space application using varactors (black boxes) mounted in the gap between the loops. For individually biasing the varactors, a surface-mount resistor (gray boxes) is placed in parallel with each varactor. The resistor value is much smaller than impedance of the varactor in dc and is also much larger than the ac impedance of the varactor.

The bias resistance is chosen to be much smaller than the impedance of a reverse-biased varactor diode in dc ($\approx 10^{15}$ Ω). This way, the voltage across the varactor is determined by the current flowing in the resistor in dc. As a result, a known dc voltage is established for appropriate biasing the varactor. The bias resistance, on the other hand, should be

large enough so that the ohmic loss of the resistor at high frequencies will be well below the varactor loss. For this design, MA46H120 flip-chip GaAs varactors by M/A-COM, [115], are intended given the chip size and capacitance range considerations. An MA46H120 varactor has a Q-factor of ≈ 100 at 3 GHz. A lossy varactor can be modeled as a lossless capacitor in parallel with a resistor. Given the Q-factor of 100, the parallel resistance (Q/wC) becomes on the order of 10^5 Ω . With this calculation, an appropriate bias resistance could be $\approx 10^7$ Ω.

As mentioned above, available varactors are limited by their Q-factors at high frequencies. Varactors used to build the reconfigurable FSS, as a result, contribute to a lower performance of FSS. With a Q-factor of ≈ 150, this loss was shown (Section 5.4.2) to be about 1 dB.

5.5 Chapter Conclusions

In this chapter, a novel reconfigurable FSS based on sub-wavelength (metamaterial) elements is presented. The structure simply consists of a two-sided circuit-board loaded with lumped capacitors. It is shown that the frequency response of this structure can be easily modified using lumped capacitances incorporated into the surface. This feature allows for generating a fully tunable bandpass response. Through numerical simulations, it is demonstrated that one can easily tune either the center frequency with a fixed bandwidth or tune the bandwidth while keeping the center frequency fixed. It is also shown that the frequency response of surfaces can be transformed from bandpass to bandstop by appropriately altering the capacitance of the lumped capacitors. These features of the proposed reconfigurable surface are demonstrated through waveguide measurement of a prototype design loaded with different pairs of surface-mount capacitors.

CHAPTER 6

An Electronically Tunable Miniaturized-Element Frequency-Selective Surface without Bias Network

A novel, tunable miniaturized-element frequency-selective surface that does not require additional bias networks is presented in this chapter [108]. This spatial filter is composed of two wire-grids printed on opposite sides of a substrate and connected to each other with an array of varactors using plated via holes. Varactor diodes are positioned between the grids. Via sections and metallic pads are fabricated and create a dc path for biasing the varactors with the grids themselves. This configuration eliminates the need for any additional network, and therefore resolves the design difficulties associated with the spurious response of the bias network. An equivalent circuit model is developed to facilitate the design procedure. Full-wave numerical simulations are used to validate the results based on the circuit model. Simulations show that by altering the capacitance of the varactors from 0.1 to 1 pF, a frequency tunability from 8 to 10 GHz with an almost constant bandwidth can be achieved.

6.1 Chapter Introduction

The ability to electrically tune or alter the frequency response is a practical feature in design of spatial filters. Generating dynamic frequency behavior requires the reactive characteristics of the FSS to change with a tuning voltage or current. The literature concerning tunable FSS includes studies for the application of ferrite substrates [85–91]; some type of liquid materials as the substrate [92]; and use of plasma instead of metallic traces [93]. Plasma

elements, instead of metal, are used to create an FSS whose response depends on the state of the plasma material. Also, the theory of tunability by using the GA algorithm to control an array of switches is demonstrated in [94]. A more recent method, however, utilizes the microelectromechanical systems (MEMS) technology to build capacitors or switches to vary the shape of the unit cell [95–97].

A well-established method for tuning microwave filters uses solid-state diodes like varactors diodes, PIN diodes, and Schottky diodes [98–101]. Previously, this approach has been applied experimentally in the design of grid arrays (FSS) [53–55, 103]. The grid arrays are FSSs with series resonance characteristics ($L-C$ resonator) which were employed for active beam control applications, i.e. beam shaping (by changing the phase of the incident plane-wave) and wave amplitude control. For biasing the active components, these grid arrays require a separate circuitry. This complementary circuit basically shorts all the grid elements that are in the same row and connects them to a common dc voltage. The grid, consequently, works only for the polarization perpendicular to its rows, and therefor, the array is polarization dependent. Moreover, because of being of the type of $L-C$ resonators with reflective characteristics, such grids are typically less efficient in transmit mode (amplitude control). The reason for this low level of performance is that the bandpass spatial filtering has not been the goal of the past work. Nevertheless, biasing the varactors properly is still an area of on-going research because of the number of varactors needed to build a tunable array. Also, a major difficulty in this research is the effect of bias network on the frequency response of the FSS.

Switchable grid arrays loaded with PIN and Schottky diodes in larger scales were later appeared in [56] and [57], respectively. These arrays yet suffered from the issues of biasing and poor selectivity. A varactor-tuned, dipole-array FSS using a resistive grid for individually biasing the varactors was proposed in [104]; however, the fabrication cost/complexity and the loss associated with the bias grid remained a problem. Finally, in [105], a reconfigurable FSS was provided with a simple method for individual biasing of the varactors. Although being practical, this method required additional components (resistors) besides varactors, thus making its design less cost-effective.

This chapter presents a tunable, bandpass frequency-selective surface with an embedded

bias network. In this design, the varactors are biased in parallel and thus are controlled individually.

6.2 Configuration and Operation Mechanism

The new FSS is a double-sided circuit-board comprised of two wire-grids built on opposite sides of a very thin substrate. The unit cell drawing of this FSS is shown in Fig. 6.1. As illustrated, the grids are laterally shifted with respect to one another by half of the unit cell size in both $\hat{x}$ and $\hat{y}$ directions. A small pad is fabricated inside the grid that lies on front side of the substrate. The pad is connected at a specific point to the bottom grid through a metalized, vertical post (via). Finally, each unit cell is loaded with a varactor placed between the pad and the grid surrounding the pad.

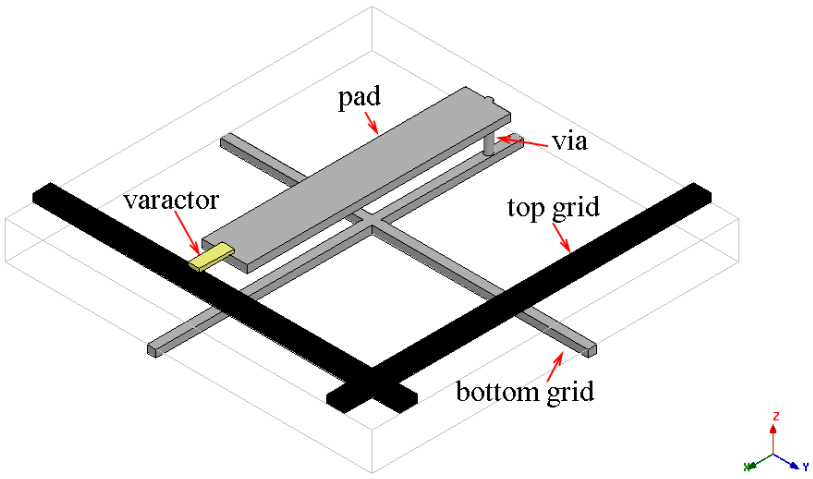

Figure 6.1: Unit cell drawing for the tunable FSS for operation in the free-space environment- The FSS is comprised of two wire-grids translated with respect to one another by half of the dimension of the unit cell. It also includes a varactor which is biased using the two grids along with a pad and a via-hole that make a dc circuit for individual biasing of the varactor.

The bandpass characteristic of the proposed FSS structure can be described using circuit theory: As shown in [5], the wire-grids are inductive which together with the varactor create a circuit topology similar to that of the Wheatstone bridge. Equivalent circuit model of the FSS is shown in Fig. 6.2. In this model, inductors L_1 and L_2 represent the metallic traces of

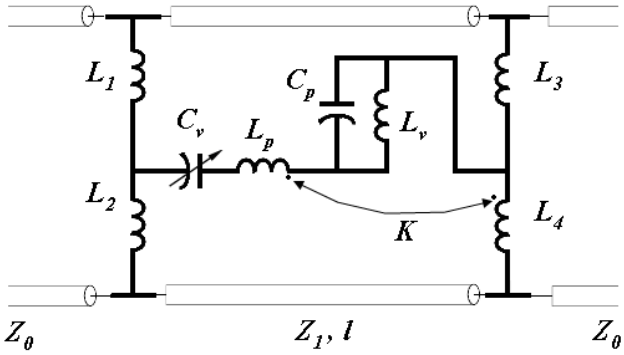

Figure 6.2: Equivalent circuit model of the tunable FSS consisting of two parallel inductive branches connected to one another through a capacitor (varactor) in the Wheatstone bridge fashion. The FSS substrate is modeled as a small piece of transmission line with the characteristics of ($Z_1 = 260\ \Omega$,$l = 5^o$) at 10 GHz.

the top grid, and L_3 and L_4 model the traces of the bottom grid. The varactor is shown by C_v in the circuit. The pad behaves like a small piece of transmission line which is modeled by inductor L_p and capacitor C_p [6]. Other elements of the circuit model are the inductor L_v representing the via and the mutual inductance K. This mutual coupling is created as the pad and the grid in bottom are overlaid on top of one another [47]. Given this arrangement of inductors and capacitors, a bandpass response is produced if the bridge is unbalanced. This happens when the ratio of the two inductors connected to the left terminal (L_1 and L_2) differs from that of the two inductors connected to the right terminal (L_3 and L_4).

As described above, on one side all the varactors are connected to the top grid and on the other side are attached to the bottom grid. Hence, by applying a dc voltage between the two grids, all the varactors are biased at the same voltage (parallel biasing). Obviously, the wire-grids are functioning simultaneously as the elements of the FSS and the bias network.

6.3 Design and Optimization

This section outlines the FSS design procedure deploying full-wave and circuit simulators. The design goals include: 1) achieving a small unit cell dimension ($\approx \lambda/10$) in order to obtain a better uniformity and thus less sensitivity to the incidence angle, as discussed in Chapter 3; 2) achieving a reasonably large tuning range while keeping the capacitance variations within

a practical range (0.1–1 pF).

As mentioned earlier, ADS analysis of the circuit model reveals that a bandpass response can be produced by the FSS provided that the bridge is unbalanced. This requirement can be accomplished in practice by positioning the via so that the unit cell is asymmetrical (unbalanced). The proposed unit cell is shown in Fig. 6.1. After finding an appropriate place for the via, other design parameters are optimized to further improve the bandpass characteristics of the FSS. The simulations use the periodic boundary conditions (PBC) in Ansoft HFSS. This setup simulates a large array of unit cells on an FSS that are exposed to a plane-wave incident at an arbitrary angle. The following simulations assume a plane-wave polarized parallel to the pad. The effects associated with the dielectric/copper loss and a finite Q-factor of the varactor are also included.

6.3.1 Optimized Tunable Frequency-Selective Surface

For operation at X-band, a unit cell size (D_x,D_y) of 4.8 mm is chosen according to the insights gained from our previous work, [38], and to attain the afore mentioned design goals. With such periodicity, the initial values assigned to the width of the wires (δ_t for top grid and δ_b for bottom grid) become 0.1 mm which is well above the minimum feature size ($\approx$ 0.05

Table 6.1: Tunable FSS's Static Design Parameters at X-Band for Free-Space Operation

δ_t	δ_b	w	t	d	ε_r	$D_x \times D_y$
0.24 mm	0.12 mm	0.5 mm	0.4 mm	3.73 mm	2.2	4.8 mm × 4.8 mm

Table 6.2: The Circuit Model Values for the Tunable FSS at X-Band for Free-Space Operation

L_1	L_2	L_3	L_4	L_p	L_v	K	C_p	l
0.35 nH	1.73 nH	1.45 nH	0.17 nH	0.37	0.04	1	$\approx$ 0 (10 fF)	5°

mm) that can be fabricated using the standard copper etching process. The optimization is then focused on other parameters of the design including w representing the width of the pad, d as the length of the pad, and t standing for the substrate thickness (see Fig. 6.1). The substrate used is Rogers RT/duroid 5880 material, [111], with a 1/2 Oz. copper cladding. Table 6.1 provides the optimized values for the parameters. Given these values, the frequency response of the FSS was calculated using HFSS. The simulated results compared to those obtained by ADS are given in Fig. 6.3, showing a good agreement between the FSS and its circuit model. The circuit model values are shown in Table 6.2. These values are the result of a curve-fitting process using ADS to get the best fit between the circuit response and the HFSS response.

The tunability of the FSS is shown in Fig. 6.4. The frequency-band 8–10 GHz is swept by varying the capacitance from 1 to 0.1 pF. Fig. 6.5 shows the scan performance of the FSS. The FSS preserves its frequency-selective characteristic; however a lower selectivity is observed while scanning at a 45^o angle. In the next section, we present the results of sensitivity analyses performed over other design parameters. These results are then interpreted using

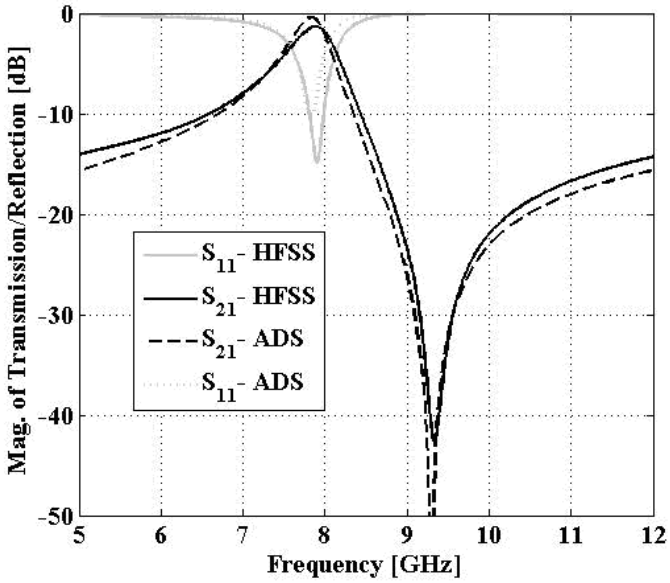

Figure 6.3: Free-space simulations of the tunable FSS using the periodic boundary condition setup in HFSS at normal incidence compared to ADS circuit simulations- The HFSS and ADS parameters values are provided in Tables 6.1 and 6.2, respectively.

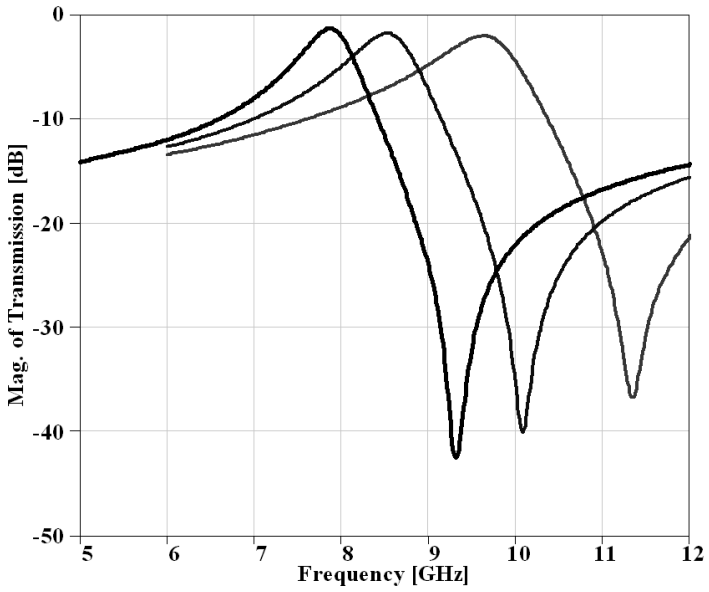

Figure 6.4: Free-space simulations of the tunable FSS using the periodic boundary condition setup in HFSS at normal incidence- Frequency tuning from 8 to 10 GHz with an almost fixed bandwidth is achieved by changing the capacitance, $C_v = 1$, 0.3, and 0.1 pF; $Q_c = 25$. The larger the capacitance, the lower the center frequency of the passband.

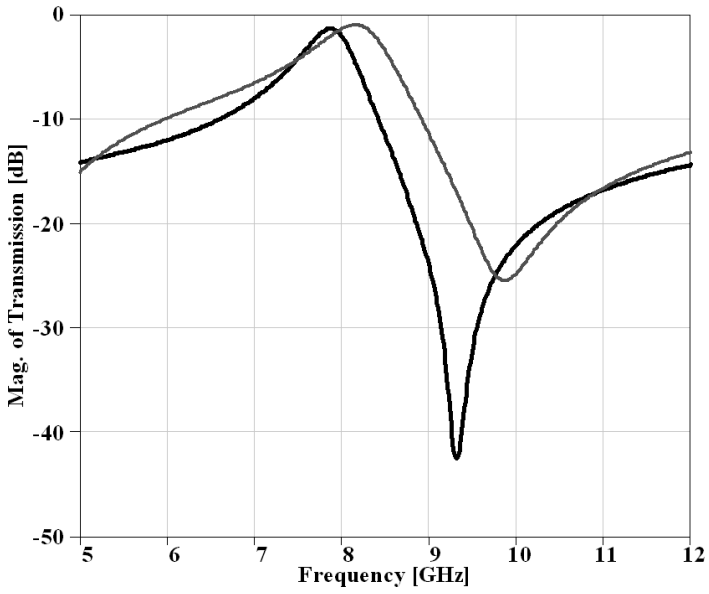

Figure 6.5: Free-space simulations of the tunable FSS using the periodic boundary condition setup in HFSS- Scan performance of the surface at an angle of 45^o (the thinner line) is compared to the case of a normal incidence (the thicker line) with polarization along the pad.

the circuit model, demonstrating the accuracy of the model.

6.3.2 Sensitivity Analysis and Circuit Analogy

The FSS design approach is investigated in more depth in this section through a number of sensitivity analyses. In addition to designing an FSS with optimum characteristics, such analyses give insight into the behavior of the FSS which can also be explained qualitatively using the circuit model. Given the knowledge obtained from the sensitivity analyses and the circuit model, the behavior of the FSS can be predicted readily with some level of accuracy.

The optimization criteria, as discussed previously, consist of staying within the fabrication limits while decreasing the unit cell size and minimizing the insertion loss. As for the filtering characteristics, a roll-off factor of more than 10 dB/GHz around the center frequency of the passband is sought. The sensitivity of the FSS's response with respect to the pad length is shown in Fig. 6.6. In these simulations, the length is varied slightly from the optimum value of 3.73 mm. Increasing the length decreases the center frequency as a result of a larger

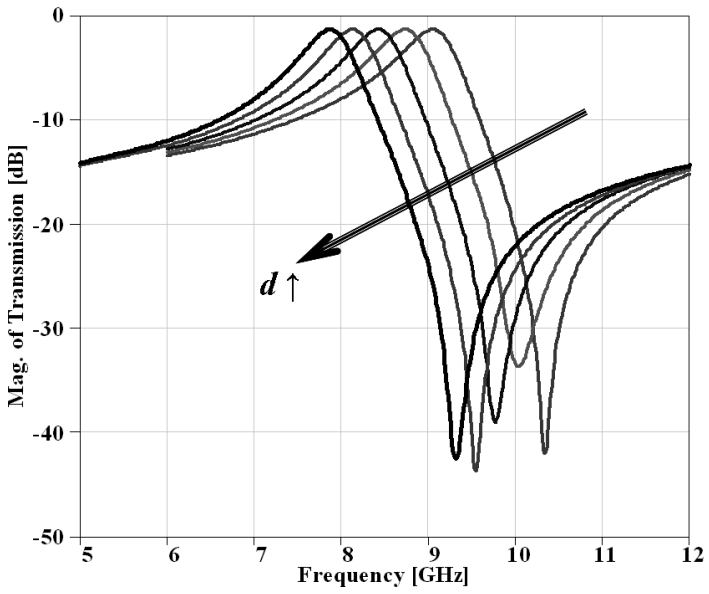

Figure 6.6: Free-space simulations of the tunable FSS using the periodic boundary condition setup in HFSS- Response sensitivity to the pad length (d) is shown for d = 2.93, 3.13, 3.33, 3.53, and 3.73 mm. Other parameters are set to: $\delta_t = 0.24$ mm; $\delta_b = 0.12$ mm; $w = 0.5$ mm; D_x and $D_y = 4.8$ mm; $C_v = 1$ pF; $Q_c = 25$.

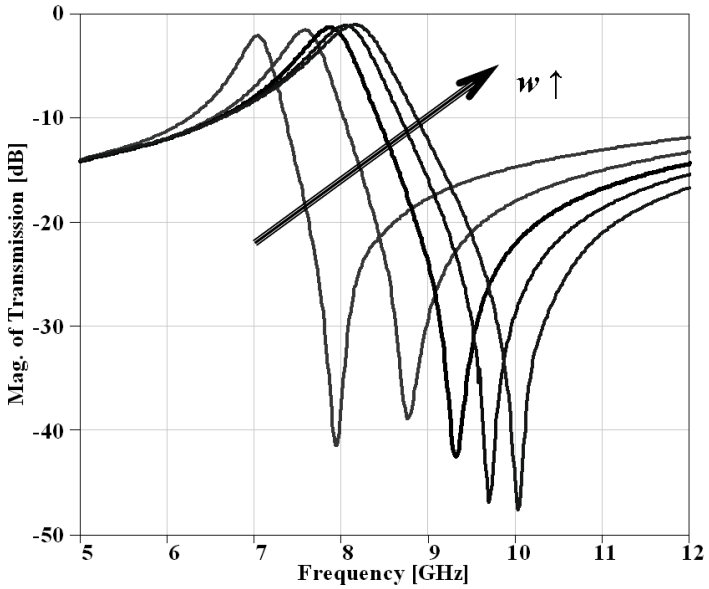

Figure 6.7: Free-space simulations of the tunable FSS using the periodic boundary condition setup in HFSS- Response sensitivity to the pad width (w) is shown for $w = 0.1$, 0.3, 0.5, 0.7, and 0.9 mm. Other parameters are set to: $\delta_t = 0.24$ mm; $\delta_b = 0.12$ mm; $d = 3.73$ mm; D_x and $D_y = 4.8$ mm; $C_v = 1$ pF; $Q_c = 25$.

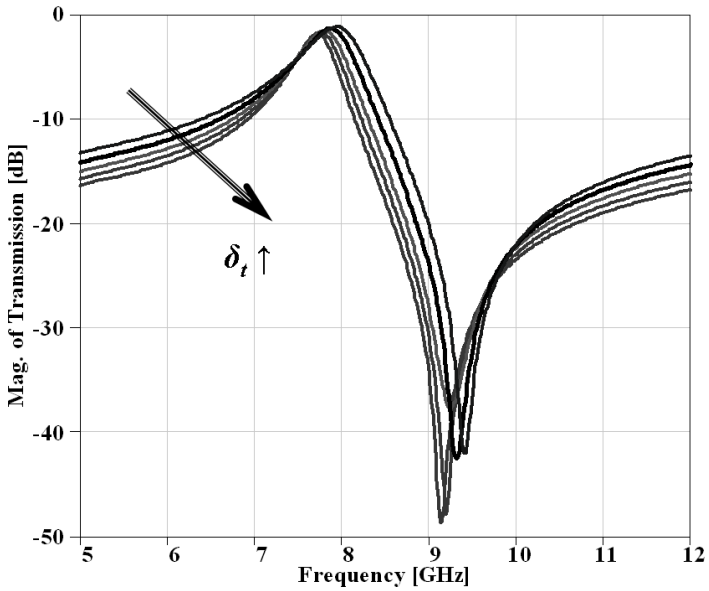

Figure 6.8: Free-space simulations of the tunable FSS using the periodic boundary condition setup in HFSS- Response sensitivity to top grid width (δ_t) is shown for $\delta_t = 0.14$, 0.24, 0.34, 0.44, and 0.54 mm. Other parameters are set to: $d = 3.73$ mm; $\delta_b = 0.12$ mm; $w = 0.5$ mm; D_x and $D_y = 4.8$ mm; $C_v = 1$ pF; $Q_c = 25$.

bridge inductance, L_p. Fig. 6.7 shows the effect of the pad width which is also related to the inductor L_p. A wider pad produces a smaller inductance [6], thus pushing the passband to higher frequencies. Changing the pad dimensions also affects the shunt capacitance, C_p, to some extent. However, for this structure, the inductive effect (L_p) dominates the change in capacitance (C_p).

As mentioned earlier, a wire-grid produces an inductive response which depends on the width of the traces constructing the grid. Wider traces result in lower inductance [5]. According to circuit model, decreasing the inductance (L_{1-4}) increases the center frequency of the response. Sensitivity of FSS to the width of the top and bottom grids is provided in Fig.'s 6.8 and 6.9. As shown, the FSS demonstrates a little dependence on the changes in the top grid (Fig. 6.8). The notch and the passband frequencies remain almost fixed. However, the effect of smaller inductance predicted by circuit model is clearer at lower band frequencies.

Fig. 6.9, however, shows a different, unexpected behavior. By increasing the width of the bottom grid, the center frequency of the passband decreases. This behavior happens because the bottom grid (L_4) is coupled with the pad inductance (L_p). Decreasing L_4 also decreases the coupling coefficient (K) which in turn pushes the notch to lower frequencies according to the circuit simulations. For this specific circuit, K is dominant over L_4; therefore, the center frequency goes down. Nevertheless, the effect of smaller inductance, i.e. shift to higher frequencies, is observed again at the lower band frequencies (see Fig. 6.9).

Finally, the effect of the substrate thickness is provided in Fig. 6.10 which is also validated by the circuit model. A thicker substrate corresponds to a longer transmission line, (Z_1,l), in the model. According to the circuit model, increasing the length of the transmission line decreases the center frequency of the passband slightly. The full-wave simulations (Fig. 6.10), however, predict a much faster change in the center frequency. This is because increasing the length reduces the coupling between the wire-grids. Circuit model well verifies that decreasing the coupling coefficient, K, changes the center frequency rapidly to smaller values.

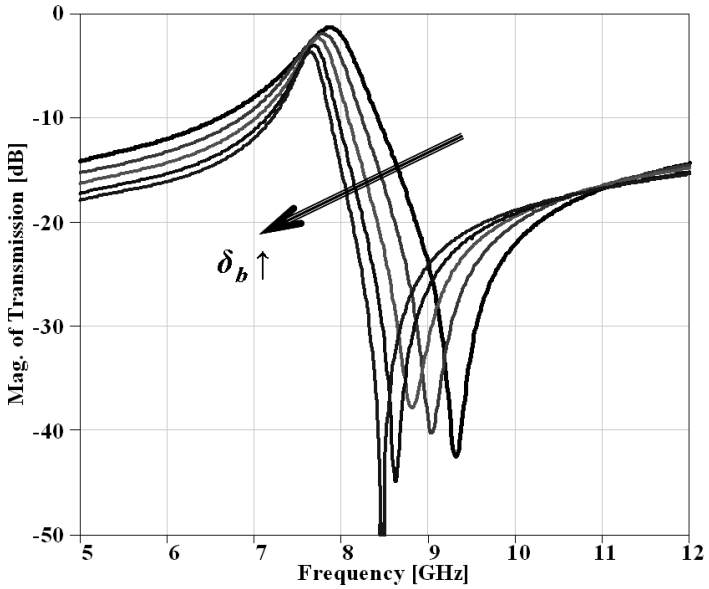

Figure 6.9: Free-space simulations of the tunable FSS using the periodic boundary condition setup in HFSS- Response sensitivity to the bottom grid width (δ_b) is shown for $\delta_b = 0.12$, 0.22, 0.32, 0.42, and 0.52 mm. Other parameters set to: $\delta_t = 0.24$ mm; $d = 3.73$ mm; $w = 0.5$ mm; D_x and $D_y = 4.8$ mm; $C_v = 1$ pF; $Q_c = 25$.

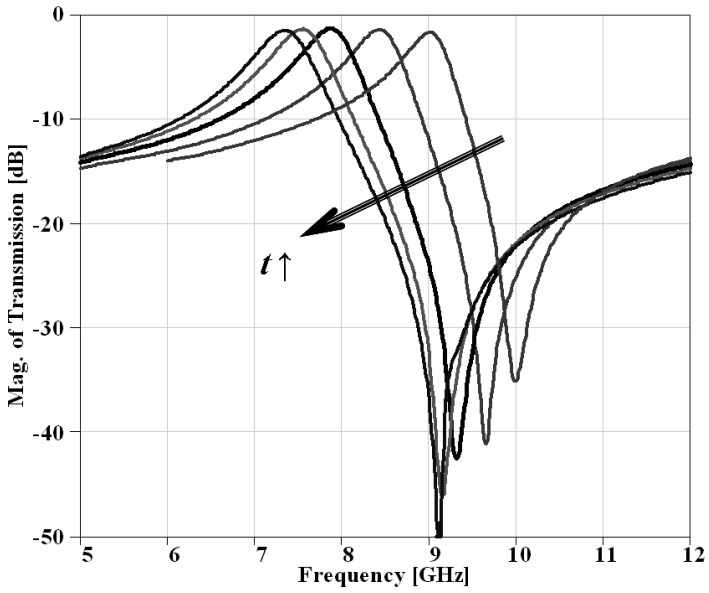

Figure 6.10: Free-space simulations of the tunable FSS using the periodic boundary condition setup in HFSS- Response sensitivity to the substrate thickness (t) is shown for $t = 0.1$, 0.2, 0.4, 0.6, and 0.8 mm. Other parameters set to: $\delta_b = 0.12$ mm; $\delta_t = 0.24$ mm; $d = 3.73$ mm; $w = 0.5$ mm; D_x and $D_y = 4.8$ mm; $C_v = 1$ pF; $Q_c = 25$.

6.4 Chapter Conclusions

In this chapter, design of a tunable frequency-selective surface with sub-wavelength periodicity is presented. The tunability is achieved by using a solid-state varactor diode per period. This research demonstrates a new architecture that enables biasing the varactors in parallel without any external biasing circuitry. The concept for the new biasing architecture consists of two wire layers along with connecting via sections built on a very thin substrate. This simple, practical method allows for implementation of large-scale tunable surfaces with high performance. The sensitivity analyses of different parameters in the numerical simulations of the FSS structure verify the application of the new method.

CHAPTER 7

A Super-Thin, Metamaterial-Based FSS-Antenna Array for Scanned Array Applications

A new filter-antenna array design is presented in this chapter [109, 110]. This design approach can be employed to simplify the vertical integration of array beamformers. Basically, by placing a high-order filter, whose response is not sensitive to angle of arrival, in front of the array elements, the need for integrating bulky RF filters behind each element is eliminated. A new method for design of such phased-arrays is provided here in which the bandpass filters are removed, and instead, a metamaterial-based frequency-selective surface is placed directly over the antenna to perform the necessary filtering. The small spacing between the frequency-selective surface and the antenna, which is as low as $\sim\lambda/10$, results in creation of a compact filter-antenna design. The close proximity of the surface and the antenna is utilized to achieve a proper coupling between the selective surface and the array for high-order filtering without adversely affecting the gain or scan characteristics of the array. To test the performance of this approach, a 9 $\times$ 9-element patch-array is fabricated and measured at X-band. The array is then loaded with a 0.004 in-thick, single-pole frequency-selective layer at a close distance on top. The measured received power as a function of frequency exhibits an improved frequency selectivity (better than the frequency-selective surface or the array alone). An improvement of about 200 percent in terms of selectivity (gain bandwidth) and the frequency roll-off rate is observed once the array is covered with the metamaterial surface.

7.1 Chapter Introduction

Phased-arrays are antenna systems with electronically-steerable radiation capabilities. Phased-arrays have been investigated and developed over the past decades because of their effectiveness in designing and controlling desired radiation patterns. The electronic capabilities of these antennas allow for generating narrow beams having low levels of side lobe and reasonable scanning ranges. The basic concept of operation of phased-arrays can be explained using antenna array theory [7] in which a progressive phase shift is assumed among the array elements. Changing the phase progression in an array can be imagined as mechanical rotation of the array platform which consequently steers the beam pattern produced by

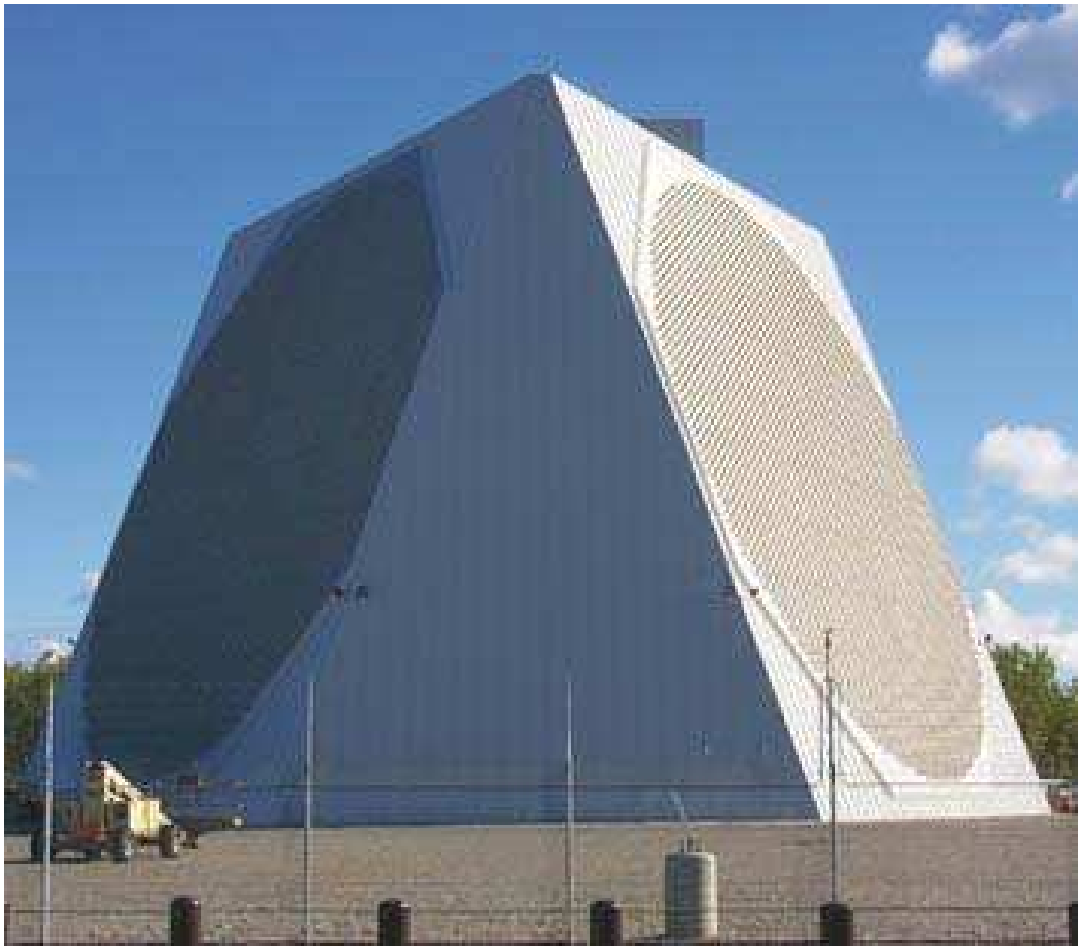

Figure 7.1: PAVE PAWS phased-array in Alaska. This 90-foot diameter radar installation monitors the northern sky (photo courtesy of En. Wikipedia).

the array antenna. A practical demonstration of the phased-array systems is provided in Fig. 7.1.

Practical realization of phase control for individual elements of the phased-array is achieved through an analog phase shifter placed on the path feeding each element. The phase shifter, as a result, is the core technology that can enable implementation of phased-array antennas. Advances in silicon technology over past years have enabled the creation of low-cost, high-yield, on-chip phased-array transceivers with improved functionalities. In [62], a fully integrated, 4-element phased-array receiver with on-chip antennas at 77 GHz implemented in a 130-nm IBM SiGe BiCMOS process is presented. A 16-element, millimeter-wave phased-array transmitter is developed in [63] using a standard 0.18-μm SiGe BiCMOS technology. This chip phased-array uses 4-bit RF phase shifters and is designed at Q-band (40-45 GHz) for satellite communications. The array elements and the digital control units are integrated on a chip area of 2.6 mm$\times$ 3.2 mm, thus achieving a high integration of millimeter-wave phased-array elements.

Radiation performance of an array system is highly dependent on the number of elements constructing the array as well as their spacing in the array. To maintain a high performance in practice, a large number of closely-spaced elements are usually needed. These requirements, from a practical perspective, pose numerous difficulties including fabrication complexity, high power consumption, and cost. Another drawback in application of the phase shifters is their limited range of tunability. Simple bias networks in practice are usually preferred to avoid complicated circuitry to decrease the design risk factor. This consideration, in addition to the limited tunability of the phase shifters themselves, in general limits the applicability of the phased-arrays to one-dimensional, small-angle scanned array scenarios. An alternative approach for generating a controlled, radiated beam has been proposed. This method could offer enhanced scanning features as well as improved antenna performance [64]. This proposal has initiated a new area of research in antenna theory based on the digital signal processing. The new method constructs a digital beamforming (DBF) array with enhanced functionalities.

Digital beamforming is a powerful method to enhance the antenna performance. In DBF the received signal from each array element is processed individually. These systems are

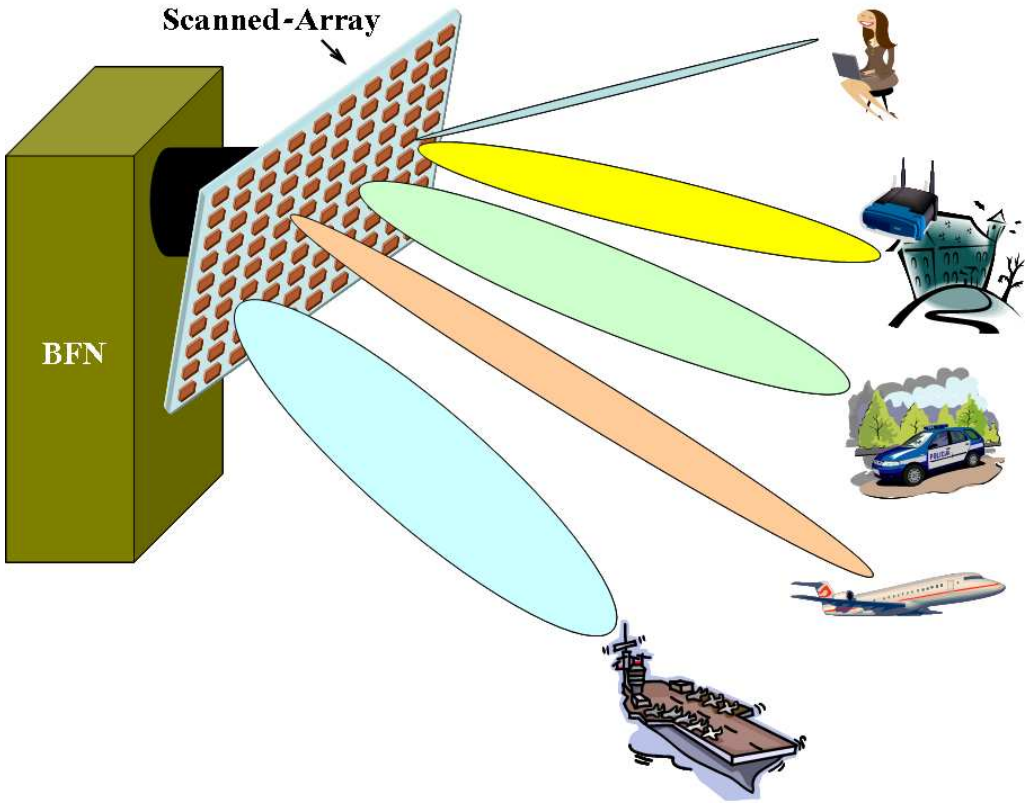

Figure 7.2: A digital beamforming (DBF) array with multiple beams. The required signal processing is performed in the beamforming network (BFN) box which is responsible for controlling the scanning array antenna.

less complex since beamforming is not carried out using analog phase shifters. Signals are simultaneously processed in the digital domain to generate a multitude of beams essential for a variety of applications concerning both communications and radar systems (see Fig. 7.2). These include fast adaptive interference rejection, ultra-low side-lobes, high resolution direction finding, etc. Cars, for example, could use multiple beams to communicate with or track surrounding vehicles. Also, multiple beams could be used to quickly discern the direction of best signal strength in high clutter environments.

DBF is most advantageous in its receive mode [64]. The features provided by DBF in this mode include: improved adaptive pattern nulling; closely-spaced multiple beams; array element pattern correction; antenna self-calibration and ultra-low side-lobes; super-

resolution; and flexible radar power and time management.

Given the recent advances in microwave monolithic integrated circuits (MMICs), high-speed digital electronics and signal processors, implementation of beamformers is practical nowadays. The earliest reported DBF system is the ELRA phased-array radar in West Germany [64]. However, the major drawback of the DBF approach is the cost of vertical integration, i.e. each element of the beamformer requires its own transceiver chain consisting of the amplifier, microwave filters, mixers, etc. In addition, the current silicon technology is not capable of integrating all the components required in the transceiver chain on a single chip. The microwave filters available to engineers are usually bulky and take up large volume. Once used in design of a beamformer, such filters enforce a minimum limit (possibly larger than $\lambda/2$) as for the spacing between the array elements. As a result, the grating lobes could become inevitable.

7.2 Application of Planar, Periodic Structures as Superstrate for Antenna Directivity Enhancement

Research on multilayer, dielectric superstrates in the past primarily concerns the antenna gain or bandwidth enhancement [65–68]. A stack of electric and magnetic superstrate layers, if arranged and chosen properly, is shown that can behave like a lens. Once placed on top of a printed antenna, this stack of substrates bends the rays emanating from the antenna and incident upon the interface of the substrate and the stack according to Snell's law. A transmission line modeling of the multiple layers can be used to choose the layers parameters properly to achieve the highest gain [67].

Application of low-profile, periodic structures, as superstrates, in conjunction with planar antennas has been also considered previously [69, 70, 72, 73] . The gain enhancement using periodic arrangements is based on the same effects occurring in the process of gain improvement using a reflector or a lens placed in front of an antenna. Both cases create a larger radiating aperture compared to that of the antenna alone, thus achieving a higher gain. The use of these structures instead of lenses or reflectors, however, allows for construction of

low-profile, high-gain antenna structures. Research in this area includes studies on electromagnetic or photonic bandgap (EBG or PBG) structures [69, 70, 72] and frequency-selective surface (FSS) structures [73].

The structure presented in [70] is further studied in a follow-up article in [71]. This EBG is composed of an array of cylindrical dielectric rods with dielectric constant of $\epsilon_r = 9.8$ in the air. The rods are parallel, periodically disposed. This structure is then used to the build a two-dimensional EBG resonator antenna for operation at 4.75 GHz. The antenna is basically a patch antenna covered by the EBG at distance $\sim\lambda/2$. By placing the EBG over the antenna, the effective, radiating aperture dimensions are increased to 21.2 $\times$ 21.2 which in turn results in an increased realized gain of about 19 dB compared to a regular patch element ($\sim$5 dB). The overall height of the resonator antenna is 56 mm ($\sim\lambda$). Although being very thick compared to the planar antennas, this antenna competes with classical high-gain antennas like horns, reflectors, and lens-corrected antennas as it has a smaller thickness. Similarly, in [72], a finite cylindrical-rod EBG in the air is presented. This structure is then positioned on top of a patch antenna to enhance the directivity and to perform a limited angular, spatial filtering. This EBG, however, must be about half of the wavelength away from the antenna. Finally, a "thin" FSS-Antenna is presented in [73] in which a single patch antenna is covered with a proposed, two-layer FSS placed at a distance $\lambda/2$ over the antenna. Similar to the case of the previous works, this antenna exhibits an enhanced directivity (compared to the single patch used in the FSS-antenna combination) as a consequence of a larger radiating aperture compared with the that of the original patch. Nevertheless, this design is over $\lambda/2$ thick.

7.3 Application of Miniaturized-Element Frequency-Selective Surfaces in Beamforming Technology

As discussed in previous section, periodic structures (EBG or FSS) have been utilized as superstrates in design of antenna structures with increased gain. They have also been used as the antenna ground-plane to enhance the bandwidth (see Chapter 1). Past research,

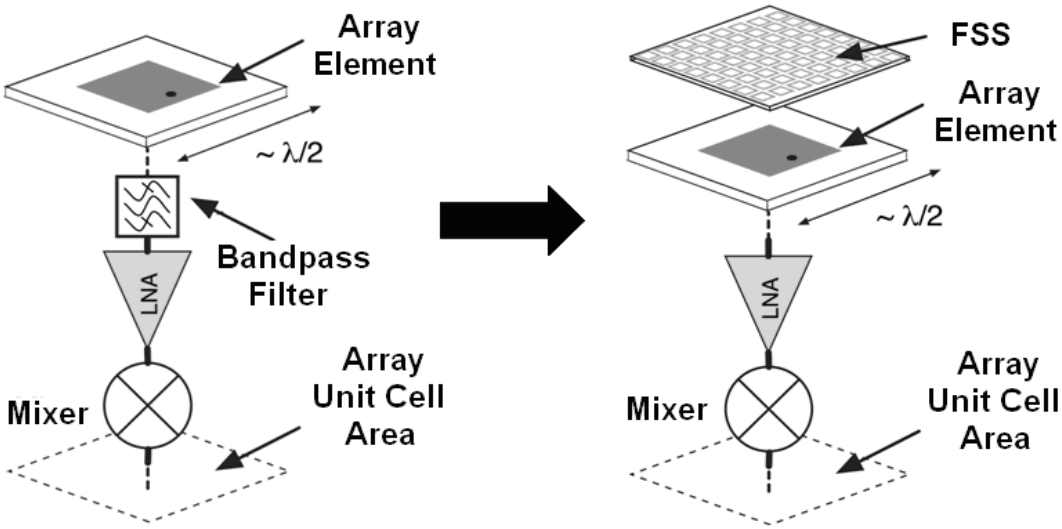

Figure 7.3: The filter in the receive path of each element of the beamforming array is replaced with the FSS above the patch antenna. As a result, one FSS, instead of one filter per element, performs the filtering for the whole array elements.

however, has not addressed a number of issues: There are practical issues related to the use of such structures as the antenna superstrates; the major problem is the adverse effects of the superstrate on the scan performance of the antenna, an undesirable feature that can not be tolerated in scanned-array design. Another issue is the overall height of the superstrate-antenna achieved based on the traditional methods mentioned above. Conventional methods require a separation distance of $\lambda/2$ between the antenna and the periodic structure. This thickness might not be practical for some applications. Moreover, the thickness of the superstrate itself is another limiting issue. Nonetheless, past research on superstrates traditionally studies the antenna characteristics, i.e. the antenna gain or bandwidth, and the frequency filtering characteristics that could be obtained by the superstrates need further investigations.

The purpose of this chapter, from a practical perspective, is to study the possibility of reducing the complexity associated with the integration process of beamforming array systems given the recent advances in semiconductor technology. As mentioned in Section 7.1, the size of the bulky bandpass filters in the receive path of the array elements is a limiting

issue given that the elements should be closely spaced to avoid the onset of the grating lobes. This research proposes that the bandpass filters can be eliminated; instead, a thin layer of FSS is overlaid on top of the antenna array as a filter-superstrate to perform the required filtering. This approach is demonstrated in Fig 7.3. In addition to resolving a portion of the fabrication issues, this scheme reduces the overall cost as a single FSS replaces the bandpass filters required per element.

A super-thin FSS-antenna array based on the miniaturized FSS described in Chapter 3 is presented here. This filter-antenna, which has an extremely low thickness ($\sim\lambda/10$), can be used to construct a reduced beamforming array in which the bulky bandpass filters in the receive chain of each antenna element are eliminated. The necessary filtering is then performed by the miniaturized FSS placed over the array (see Fig 7.3) at a distance of $\lambda/10$.

The localized frequency selectivity of the FSSs based on the miniaturized approach, [38], enables the creation of very thin FSS structures with high scanning stability. In addition, these spatial filters can perform properly even at a close distance (compared to the wavelength) to the antenna. These are critical features generally not seen in traditional FSS structures.

Through the numerical simulations, it is shown that the metamaterial FSS has a negligible effect on the antenna performance. Although being very close to the array antenna, the metamaterial spatial filter has almost no effect on the gain, scan characteristics, and the polarization purity of the array antenna. Next, experiments are performed to test the performance of this approach and the miniaturized FSS's capabilities. This measured characteristics are provided at the end.

7.3.1 Design and Analysis

In this section, numerical analysis of the proposed FSS-antenna array using the periodic boundary conditions (PBC) is presented. The miniaturized surface and the patch-array employed in the antenna building are first described. The antenna performance, calculated using the Ansoft HFSS full-wave simulator is then examined. It should be emphasized that this analysis assumes an infinitely large array of elements and therefore does not account

for the effects associated with a finite size array. These effects are generally the array edge diffraction and the different, nonuniform mutual coupling between the elements of the finite array compared to the infinite case.

Specifications of the Miniaturized-Element Frequency-Selective Surface

As mentioned above, the FSS design used here is based on a structure presented earlier in Chapter 3. As discussed there, the new approach in design of FSS structures, recently introduced in [37] and further developed in [38], achieves an inherent frequency-selective characteristic in the surface, meaning that the constitutive parameters of the surface material are manipulated such that the material itself shows selectivity with respect to frequency. Such manipulations are possible in the sub-wavelength regime where the elements of the FSS are on the order of $\lambda/10$ in dimension. It was shown that very small size of the inclusions on the surface makes it possible to describe the behavior of the FSS using a quasi-static analysis. In addition to giving insight into the physics of the FSS, the results of this analysis are formulated using the circuit theory to develop an accurate model for the FSS [38]. Excellent features of the new FSS include the localized frequency-selective properties, the

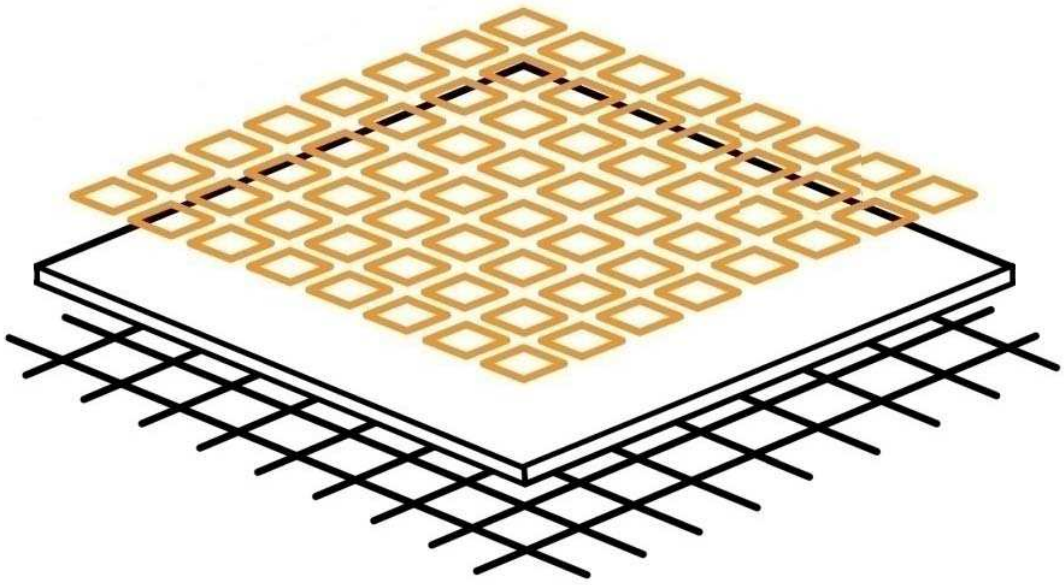

Figure 7.4: The loop-wire miniaturized FSS geometry consisting of loops and wires.

higher frequency selectivity achieved by a single substrate, the lack of pass-band harmonics in the frequency response, and the very low sensitivity of the frequency response to the incidence angle.

The FSS employed for the construction of the FSS-antenna array is a 2-D periodic circuit board consisting of an array of loops and a wire-grid on opposite sides of a thin substrate (see Fig. 7.4). The loop-wire FSS has a periodicity of 3.39 mm for operation at X-band. For the loop layer, the width of the traces used is 0.11 mm, and the gap between loops is also 0.11 mm. The wire-grid is made up of traces which are 0.95 mm thick. The substrate has a dielectric constant of $\epsilon_r = 2.94$, and its thickness is 0.1 mm . Unlike the original surface, [38], this FSS has no lumped capacitors involved in its structure.

Specifications of the Array Antenna

The antenna array is comprised of rectangular patch elements placed on one side of a dielectric substrate. The patches are fed through metalized, vertical posts (probe-fed) from the back side. The substrate has a dielectric constant of 3.38 and is 0.5 mm thick. The

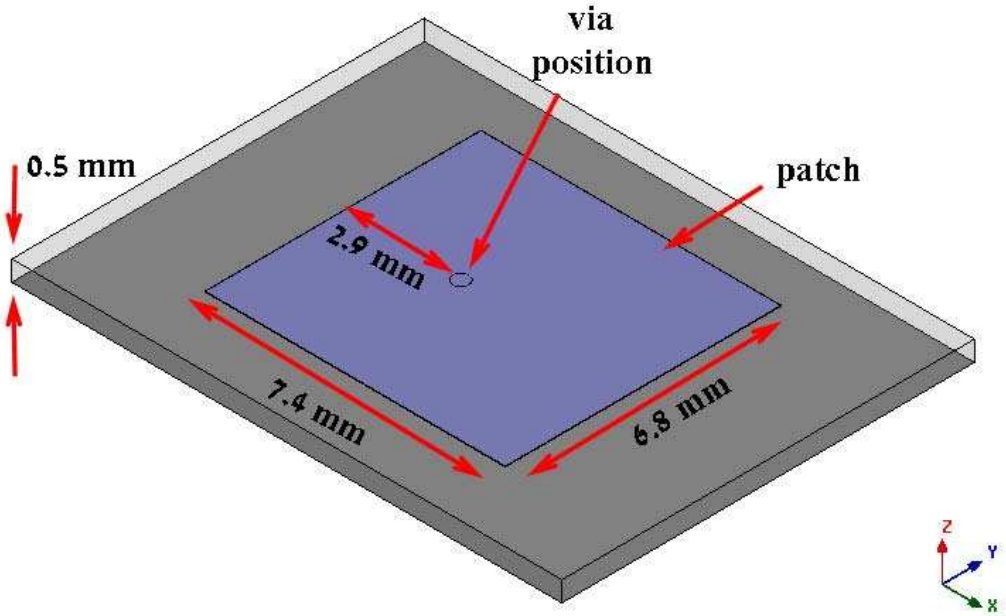

Figure 7.5: The microstrip patch antenna designed as the unit cell of an infinite array antenna- The patch is built on a 0.5 mm-thick dielectric substrate with $\epsilon_r = 3.38$.

patch-array is designed to work at a center frequency of about 10.5 GHz. For this criterion, the patch dimensions are calculated and become 7.4 mm $\times$ 6.8 mm. Other dimensions are provided in Fig. 7.5 which demonstrates a single element of the infinite array antenna.

The microstrip antenna element described above is used to construct a two-dimensional, infinite antenna array on $x - y$ plane. The periodicity of the array along the $\hat{x}$ and the $\hat{y}$ directions is chosen to be smaller than $\lambda/2$ to avoid the grating lobes.

Numerical Simulation Results

The unit cell of the FSS-antenna array is shown in Fig. 7.6. This unit cell is carefully simulated using a PBC setup in HFSS to test the radiation characteristics of the array. As mentioned previously, this simulation assumes an infinite number of such unit cells in the array.

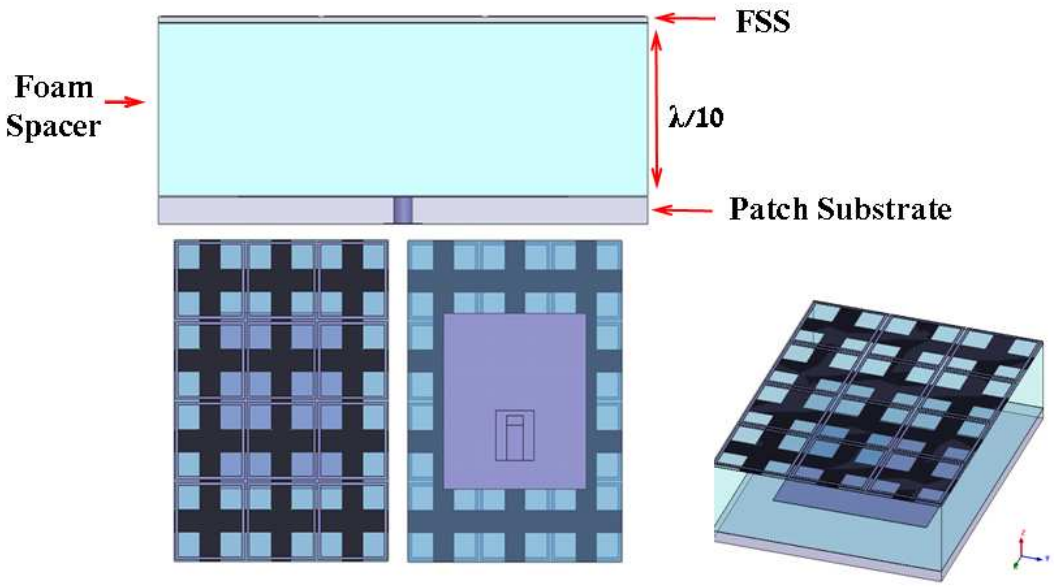

Figure 7.6: The unit cell of the FSS-patch antenna comprising a patch antenna element and an array of 4 $\times$ 3-element of the loop-wire FSS placed on top of the patch through a foam spacer with the thickness of 0.125 in. The FSS structure is much thinner than the spacer.

The results of the full-wave simulations are presented in this section. In the first set of simulations, a 2-D-infinite array antenna using patch elements shown above is considered. The simulated fields for the infinite problem are then used to approximately calculate a finite

array (9 × 9-element). These calculations are performed in HFSS simply by calculating the array factor (AF) and multiplying that with the fields (from the infinite array simulation). Next, similar simulations are performed for the same patch-array which is covered this time with the miniaturized FSS structure. A thin dielectric spacer is placed between the FSS and the antenna. The final FSS-patch-array is only $\lambda/10$ thicker than the original array of patches.

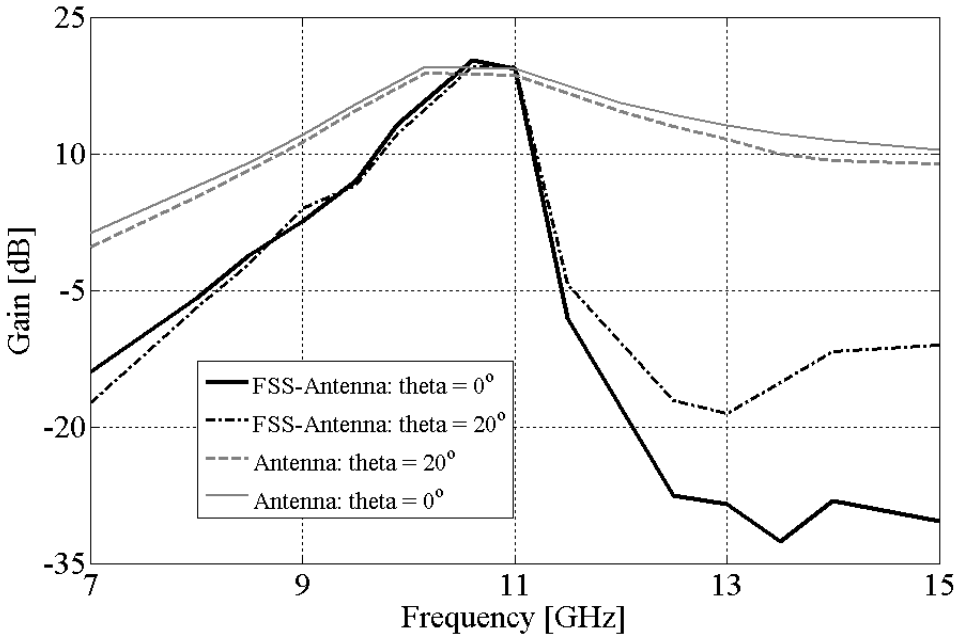

Figure 7.7: Full-wave simulations of the gain for the infinite patch-array and FSS-patch-array for scan angles $(\theta,\phi) = (0^o,0^o)$ and $(\theta,\phi) = (20^o,0^o)$ in spherical coordinate system The gain is calculated by multiplying the radiation of a single element in the infinite array by the AF of a 9 × 9-element array. A sharp filtering feature is added to the characteristics of the patch-array antenna once covered with the metamaterial FSS superstrate. Scanning has a minor effect on the performance of the FSS-array at the higher frequencies in this graph.

As mentioned above, the frequency filtering is the main purpose of the FSS-array design. The simulated maximum gains for the patch-array and the FSS-patch-array as a function of frequency are shown in Fig. 7.7. The simulations are performed for scan angles of 0^o and 20^o. As shown, the FSS-antenna radiates/receives signals with a much higher selectivity. In a way, this array now owns a bandpass filter embedded in its receive/transmit path at the cost of placing a very thin superstrate on the array.

Comparison between the gain-frequency simulations also shows an improvement in the out-of-band-rejection ranging from 20 dB (at the lower band frequencies) to 40 dB (at the upper band frequencies). The loaded array, in addition, achieves an extremely low thickness, demonstrating its superiority over the antenna structures available in the literature. Moreover, the frequency roll-off rate becomes much steeper at the upper band as it changes from -5 dB/GHz to -40 dB/GHz. All this demonstrates the ability of the metamaterial FSS in creation of a filter-antenna characteristic with a high performance. These results well demonstrates the localized frequency-selective nature of the metamaterial FSS which can properly perform frequency filtering even at a very close distance to a radiator.

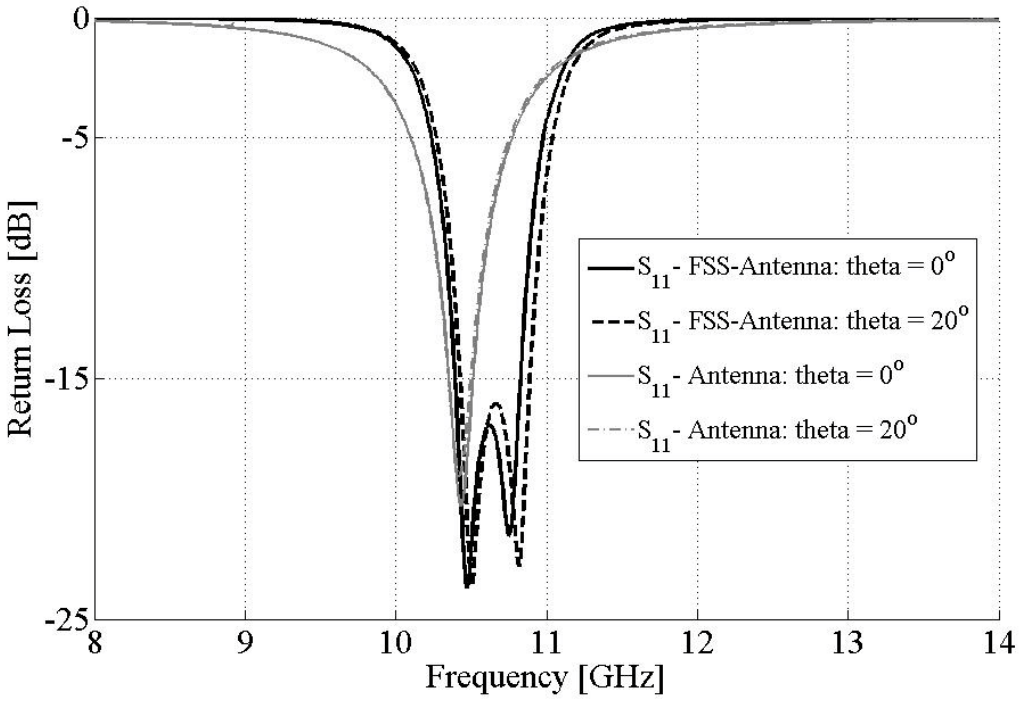

Figure 7.8: Full-wave simulations of the return loss for the infinite patch-array and FSS-patch-array for scan angles $(\theta,\phi) = (0^o,0^o)$ and $(\theta,\phi) = (20^o,0^o)$ in spherical coordinate system The patch-array has a narrow bandwidth with a resonance at about 10.5 GHz, whereas the FSS-patch-array has a two-pole response with a much wider bandwidth.

Next, other aspects of the antenna are examined. The simulated return loss for the patch-array compared with that of the FSS-patch-array, for scanning at 0^o and 20^o, is shown in Fig. 7.8. According to the simulations, the FSS-array antenna produces a two-pole, maximally-flat frequency response. This phenomenon (extra pole) is attributed to the cou-

pling of the FSS elements and the patches as the FSS and the patch-array are very close to one another. This two-pole behavior allows for shaping the frequency response of the antenna; in addition to tuning the bandwidth, this effect is employed to achieve sharper edges (steeper roll-off) around the frequency band of operation. As a secondary feature, the dual-pole behavior facilitates the designer to create a wider band of operation. In the example model considered here, a factor of 2.5 increase in the bandwidth compared with the array antenna in isolation is observed. As shown in Fig. 7.8, the operation band of the antenna is increased from 10.4–10.6 GHz to 10.4–10.9 GHz.

Other antenna parameters are calculated and compared. The radiation pattern cuts of the 9 × 9-element patch-array are shown in Fig. 7.9 (E-plane) and Fig. 7.10 (H-plane) at the resonance frequency of the elements of the patch-array (10.46GHz). As shown, the antenna peak-gain is slightly more than 20 dB and shows no sensitivity to scanning (at least up to 20^o). The calculated pattern for a 9 × 9-element FSS-antenna in transmit is provided in Figs. 7.11 and 7.12. As can be seen, the radiation patterns for the FSS-antenna are very

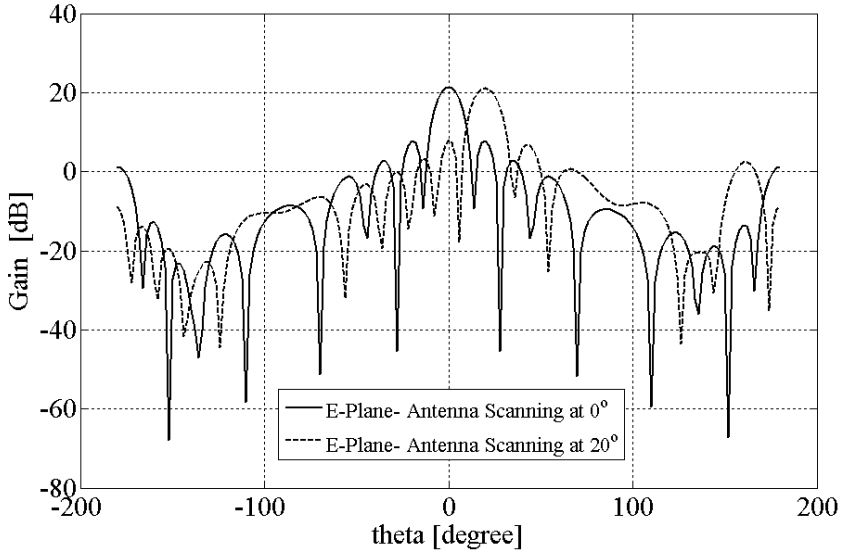

Figure 7.9: Full-wave simulation of the E-plane radiation pattern for the 9 × 9-element patch-array calculated by multiplying the radiation of a single element in the infinite array by the AF. The simulations is performed at the resonance frequency of the patches (f = 10.46 GHz) for scan angles of $(\theta,\phi) = (0^o,0^o)$ and $(\theta,\phi) = (20^o,0^o)$ in spherical coordinate system.

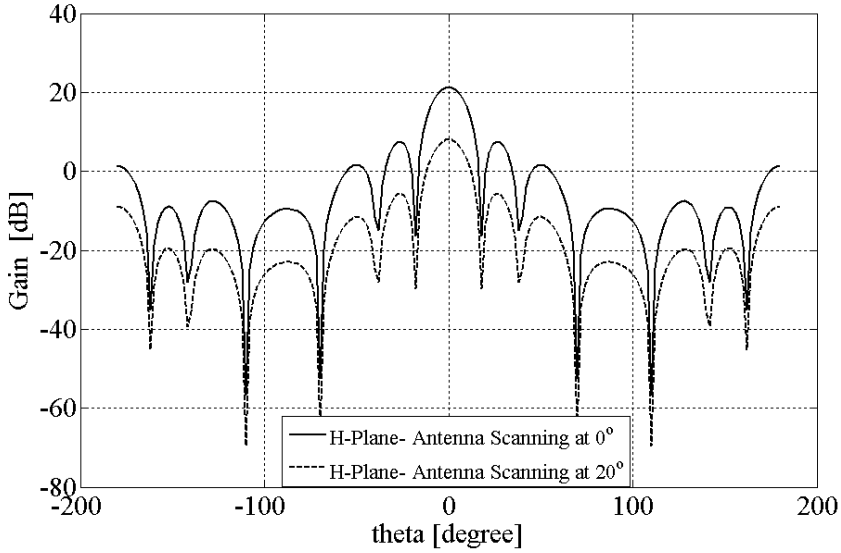

Figure 7.10: Full-wave simulation of the H-plane radiation pattern for the 9 × 9-element patch-array calculated by multiplying the radiation of a single element in the infinite array by the AF. The simulation is performed at the resonance frequency of the patches (f = 10.46 GHz) for scan angles of $(\theta,\phi) = (0^o,0^o)$ and $(\theta,\phi) = (20^o,0^o)$ in spherical coordinate system.

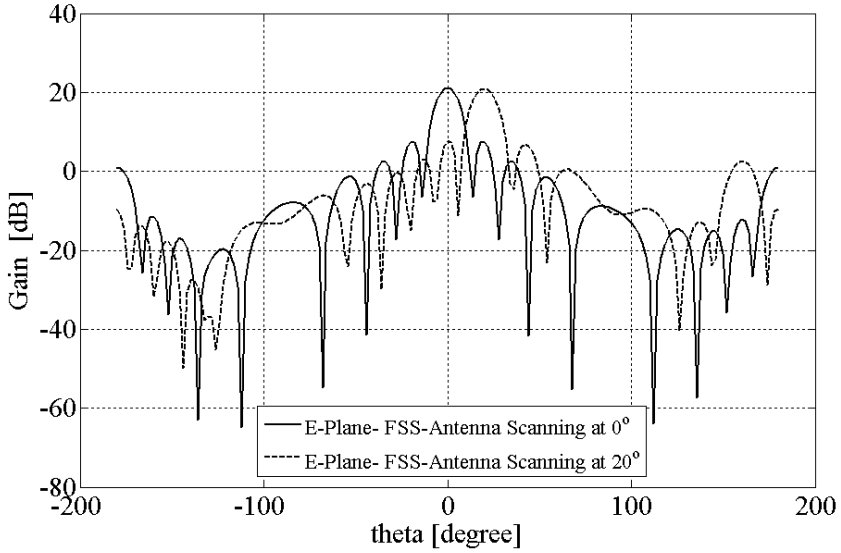

Figure 7.11: Full-wave simulation of the E-plane radiation pattern for the 9 × 9-element FSS-antenna calculated by multiplying the radiation of a single element in the infinite array by the AF. The simulation is performed at a frequency inside the operation band (f = 10.6 GHz) for scan angles of $(\theta,\phi) = (0^o,0^o)$ and $(\theta,\phi) = (20^o,0^o)$ in spherical coordinate system.

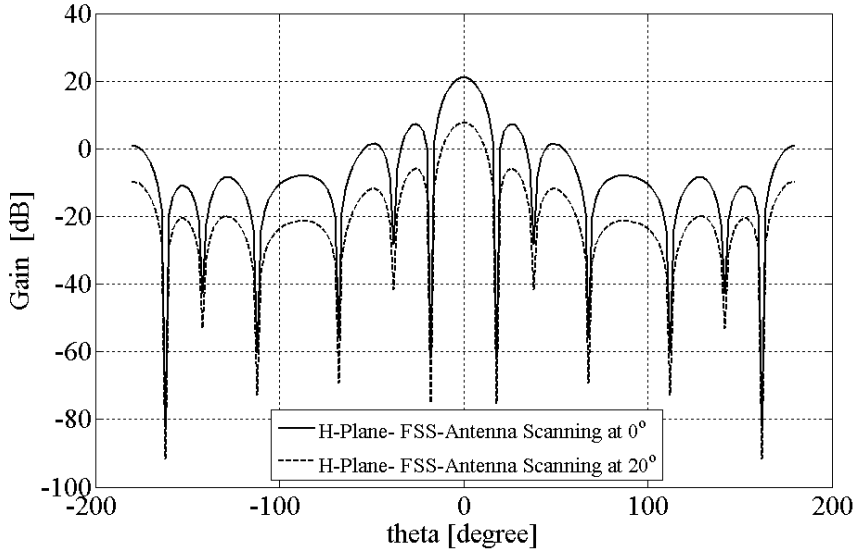

Figure 7.12: Full-wave simulation of the H-plane radiation pattern for the 9 × 9-element FSS-antenna calculated by multiplying the radiation of a single element in the infinite array by the AF. The simulation is performed at a frequency inside the operation band (f = 10.6 GHz) for scan angles of $(\theta,\phi) = (0^o,0^o)$ and $(\theta,\phi) = (20^o,0^o)$ in spherical coordinate system.

similar to those of the patch-array.

Based on the simulation results presented above, the FSS-antenna 1) behaves like filter added to the array antenna structure without affecting the gain, scan performance, and the polarization response of the scanned array antenna; and 2) provides an opportunity to enhances the bandwidth of the antenna array.

7.3.2 Fabrication and Experiment

The miniaturized surface used for antenna filtering is an X-band, 6 in × 6 in, thin FSS described above in Section 7.3.1. The FSS is fabricated through the standard etching of copper on a 0.004 in-thick CLTE substrate by Arlon. This substrate which is a PTFE composite material has a nominal dielectric constant of 2.94. The measured transmissivity of the surface is provided in Fig. 7.13 for different scan angles up to 25^o.

The fabricated array is a 9 × 9-element array of probe-(pin-)fed, rectangular patch antennas built on a 0.5 mm-thick RO4003C substrate with the dielectric constant of 3.38. As discussed in Section 7.1, each element of a beamforming array has a separate feed network.

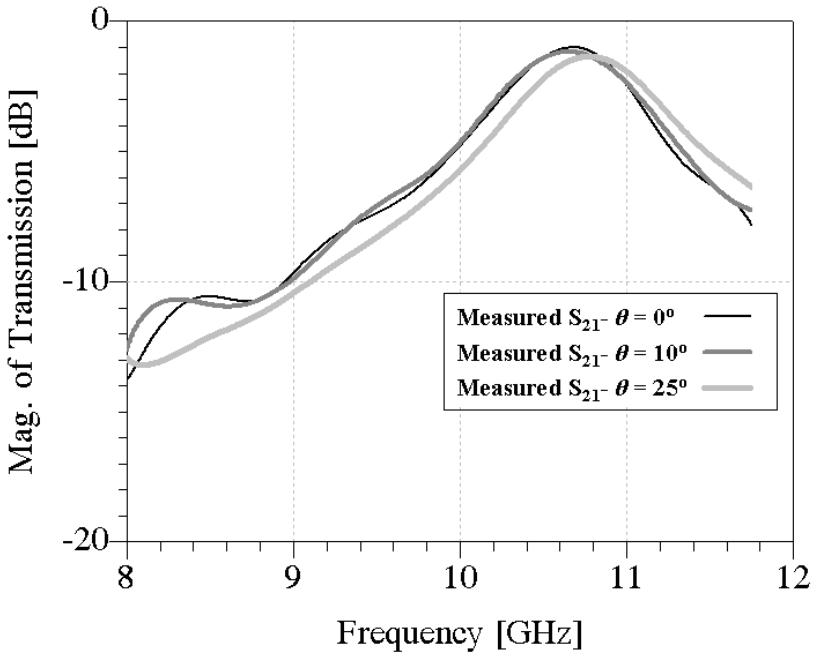

Figure 7.13: The loop-wire FSS measured transmission response is plotted for different angles of incidence (θ) of 0^o, 10^o, and 25^o for the TE polarization.

As a result, the filtering effects of the FSS should be observed at the terminal of the individual element. To emulate a similar condition in the measurement, the patch-array is fabricated with independently-fed elements, i.e. no corporate feed network is used. Each patch can be fed by a pin connected to the patch at a point where the input impedance is 50 Ω at 10.4 GHz. Here, only the received power as a function of frequency by the patch located at the center of the array is presented. To do this, the center patch is connected to an SMA connector for power reading, and the surrounding patches are matched to 50 ω through surface-mount resistors, each of which connecting the pin of an off-center patch to the ground-plane. This way, the array is build to work in the receive mode. Given the receive mode measurement results, the transmission characteristics of the array are also known according to reciprocity theorem [6]. Figs. 7.14(a) and 7.14(b) show the patch-array. Fig. 7.15 demonstrates the FSS-antenna consisting of the patch-array, a foam spacer, and the loop-wire FSS.

As mentioned earlier, the miniaturized surfaces can perform properly in a close proximity of radiating elements. This allows placement of the FSS near the antenna array, thus enabling

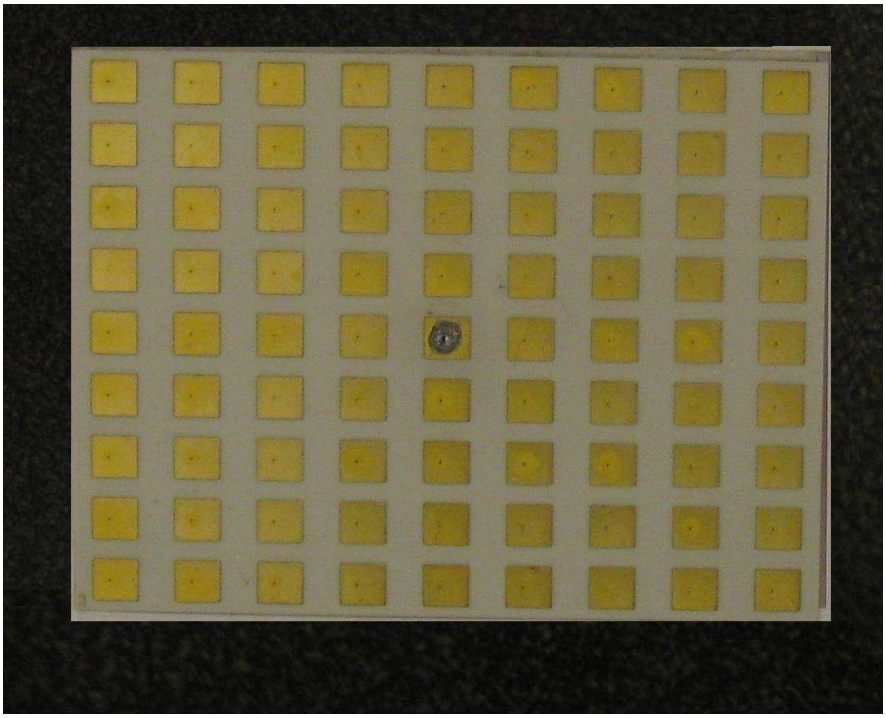

(a)

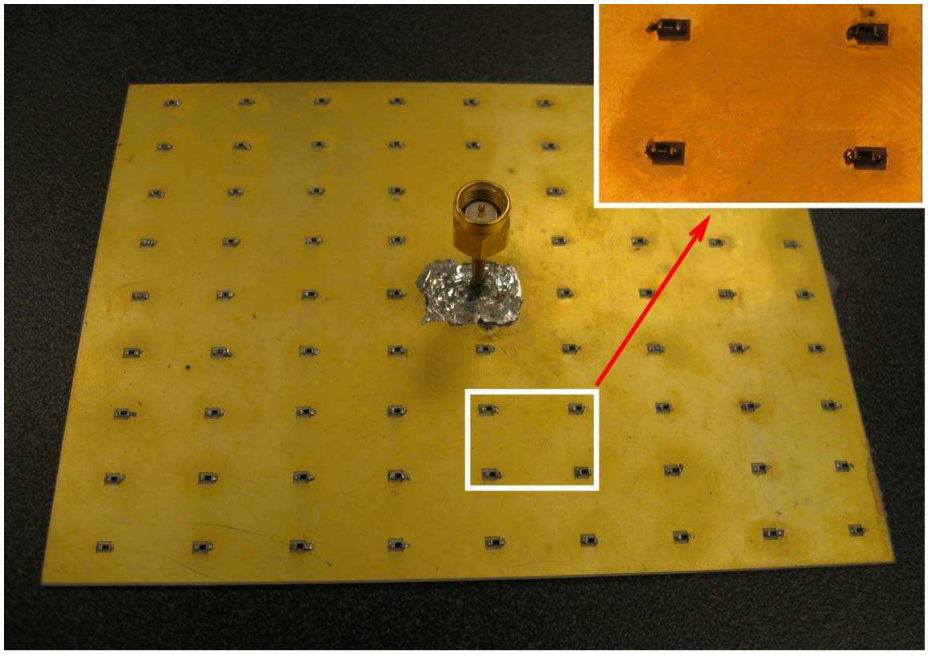

(b)

Figure 7.14: Fabricated patch-array- (a) A 9 × 9 array of patches (top side). (b) The ground-plane (bottom layer) is connected to the via post of each patch, except for the patch element at the center, through a chip resistor.

mutual coupling between the antenna and the FSS resonators. Coupling two resonators, one can achieve a maximally flat or dual-band response. In this design, the FSS is placed at the distance of $\lambda/10$ to the patch-array to establish a proper coupling between the patch and the loops/wires of the FSS. As will be shown below, because of the coupling, the selectivity of the FSS-antenna becomes better than the array or the FSS alone.

Finally, to assemble the FSS-antenna, the $\lambda/300$-thick frequency-selective layer is overlaid on top of the patch-array, as shown in Fig. 7.15. The FSS and the antenna are separated by a $\lambda/10$-thick PF-2 foam ($\epsilon_r = 1.03$) by Cumming Microwave, Avon, MA.

The setup for measuring the receiving characteristics of the array includes a transmitter (horn antenna) placed at one end of an anechoic chamber and the array itself located at the opposite side of the chamber. The center patch of the array is the receiver and is connected

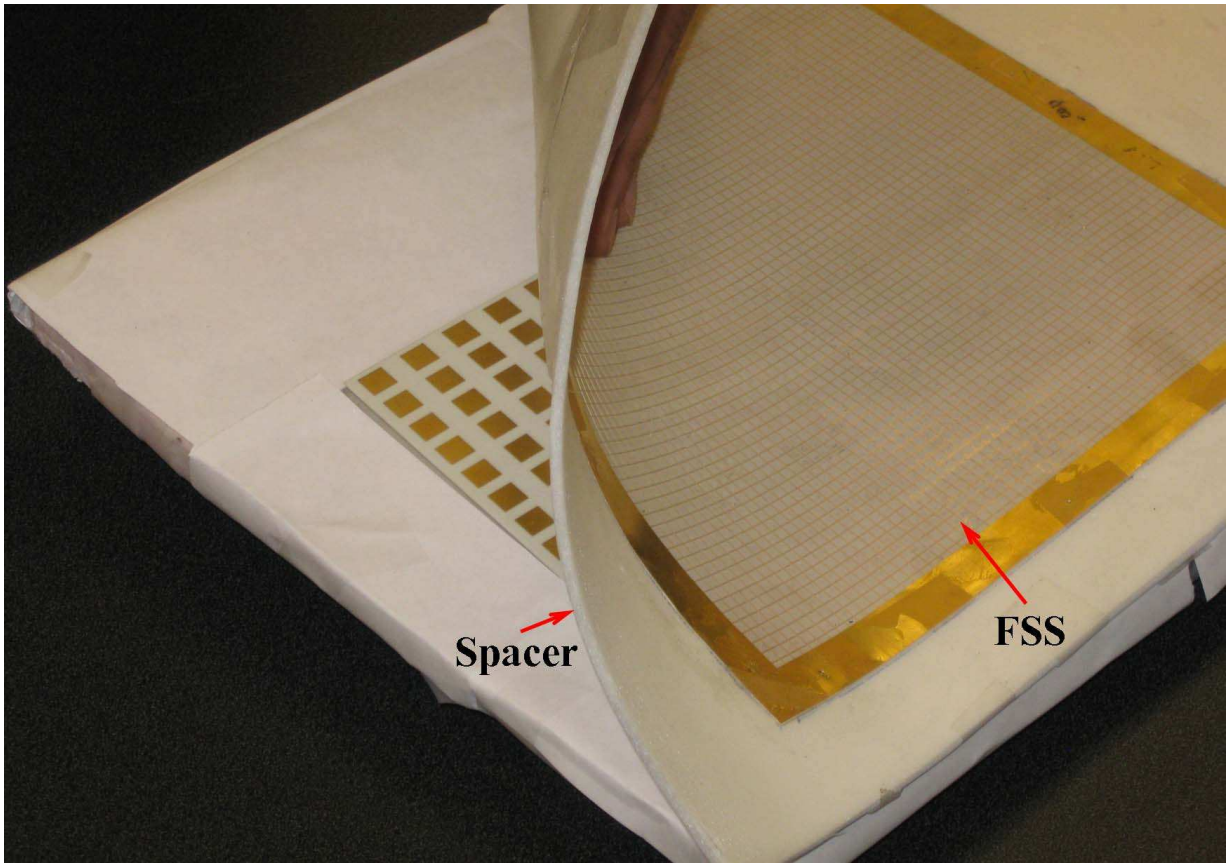

Figure 7.15: Fabricated FSS-Antenna- The thin, flexible FSS layer is placed over the antenna through a thin foam spacer.

to a spectrum analyzer for power reading. The received power at multiple frequency points covering the band 7–15 GHz is manually collected for two cases: 1) patch-array alone and 2) patch-array covered with the FSS.

The measured, received powers by the center patch as a functions of frequency for the two cases mentioned above at normal incidence are shown in Fig. 7.16. Scan performance comparison is provided in Fig. 7.17 for scanning at 0^o, 15^o, and 30^o.

The received power by the FSS-antenna, compared with the antenna alone, exhibit the filtering effect of the FSS; in the power response (Fig. 7.16), the bandwidth becomes half and the frequency roll-off rate increases by almost a factor of two around the center frequency (10.6 GHz). Moreover, the received power shows a maximally-flat characteristic, mentioned in Section 7.3.1, around the center frequency, a dual-pole behavior due to the coupling of the FSS elements with the patches. Resulting from the close proximity of the FSS and the patches ($\lambda/10$), this coupling improves the frequency selectivity of the FSS-array. However, the transmission loss is increased by about 1.5 dB. As shown in Fig. 7.13, the insertion loss

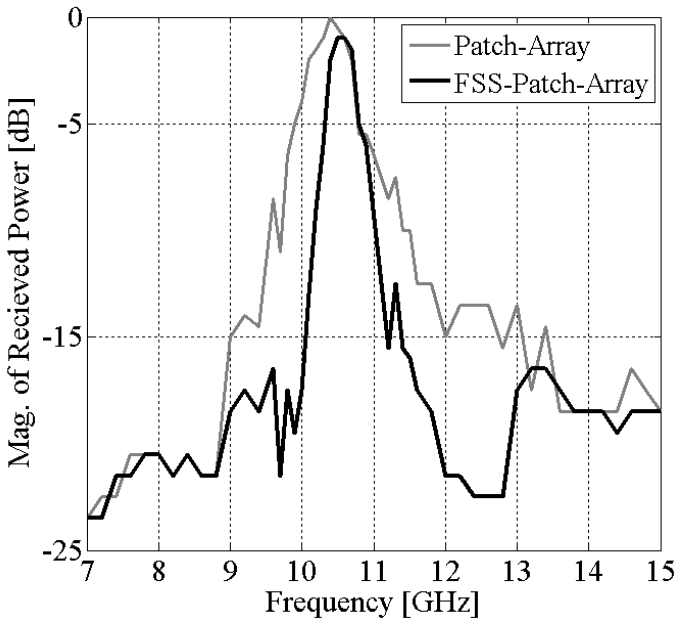

Figure 7.16: The measured received power by the patch element at the center of the array for the case of patch-array alone compared with case of the patch-array covered with the metamaterial FSS (see Fig. 7.13). In this measurement, the transmitter and the receiver were facing one another (normal incidence).

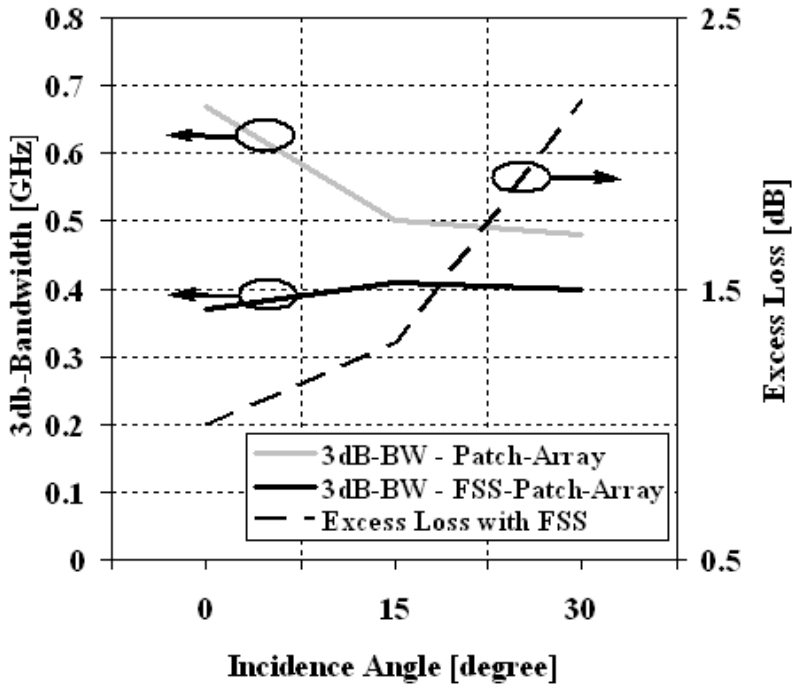

Figure 7.17: The comparison of the 3-dB bandwidth and the excess loss as a function of angle- In this measurement, the transmitter and the receiver were tilted with respect to one another by 15^o and 30^o.

of the FSS itself is about 1.2 dB which increases the insertion loss (1.5 dB) of the FSS-array. The excess insertion loss of 0.3 dB in the response of the FSS-antenna can be attributed to the mismatch occurring at the FSS-foam interface. The 3-dB bandwidth of the FSS is about 1 GHz according to Fig. 7.13. The FSS-antenna shows a reduced 3-dB bandwidth of about 350 MHz which is only 50 percent of that of the array alone and is much less than that of the FSS alone. To examine the bandwidth and the insertion loss characteristics of the FSS-antenna array, the frequency response of the antenna and the FSS-antenna were measured up to 30^o. Fig. 7.17 summarizes the 3-dB bandwidth and the excess loss as a function of angle.

It should be emphasized, however, that the FSS used in this experiment is a single-pole surface and therefore has a limited selectivity. The example presented here, however, is just a proof of concept. Apparently, multipole miniaturized surfaces, [47], can be employed to construct FSS-antenna structures with expected, higher-order filtering characteristics.

7.4 Chapter Conclusions

The loop-wire miniaturized-element FSS structure is utilized in construction of an FSS-antenna array with an extremely low thickness of $\lambda/10$ and wide angular scanning capabilities. In this process, the miniaturized surface is overlaid on top of a patch-array antenna though a foam spacer to tailor the electromagnetic radiations of the antenna in frequency. The high performance of this approach is verified through both numerical simulations and experiment. This method can enable the fabrication of beamforming arrays comprising many closely-spaced antenna elements with lower cost. In this approach, the bandpass filters that are usually required in the receive chain of the individual elements of the beamforming system are eliminated and replaced with a thin miniaturized-element FSS structure.

CHAPTER 8

Conclusion

8.1 Summary of Research

A new theory in design of microwave, spatial filters for compact communications applications is the main advance of this research. The new approach is well developed and is applied to a number of problems concerning spatial frequency filtering. The outcomes of these problems are new frequency-selective surfaces with enhanced scanning and filtering performance as well as a clear physical insight into the behavior of such surfaces (circuit model). A summary of the developments in this area of research is provided in this chapter.

Chapter 3

The theory of the miniaturized-element frequency-selective surface (FSS) is presented here through a discussion on the physics of the new approach. This work introduces a new miniaturized surface, the loop-wire FSS, with excellent characteristics. Being composed of sub-wavelength ($\lambda/12$) elements, the loop-wire FSS achieves an inherent (localized) frequency selectivity in the surface with a harmonic-free behavior. The practical features of interest made possible because of the inherent filtering characteristics include:

1) The higher-order frequency response achieved by a single, thin substrate;
2) The lack of passband harmonics in the frequency response;
3) The very low sensitivity of the frequency response to the incidence angle of the exciting,

electromagnetic wave;
4) The ability to perform filtering even at a close distance to an electromagnetic radiation source; and finally,
5) The overall smaller dimensions of the FSS platform.

Chapter 4

The multipole characteristics of the miniaturized surface are investigated in this chapter. The conventional approach of cascading single-pole FSS structures is used to build a dual-bandpass miniaturized surface using the surface introduced in Chapter 3. This chapter next presents a new element, a single-pole FSS with only one metalized layer. The new surface, which is a modified version of the loop-wire FSS, is then shown that can be used to achieve a super-thin, dual-pole characteristic. This dual-band FSS is only $\lambda/240$ thick.

Chapter 5

Electronic tuning as a practical feature of interest is the focus of this chapter. This chapter presents a reconfigurable bandpass surface made using a parallel arrangement of varactor-tuned, resonant $L-C$ layers. This configuration of bandstop layers allows for more a flexible frequency behavior. The design presented in this chapter has two modes of operation: bandstop and bandpass. In addition to two completely different modes of operation, the center frequency, as well as the bandwidth of the response can be tuned independently.

Chapter 6

The tuning problem is further investigated in this chapter. This chapter, however, takes a different approach; inductive FSS layers (wire-grid) are put together along with an array of varactors connecting the grids. A two layer version of this method is designed with a bandpass characteristic. Varactor diodes are positioned between the two grids. Via sections and metallic pads are also fabricated to create a dc path for biasing the varactors with the grids themselves. This configuration, therefore, eliminates the need for any additional

network for biasing the varactors, and thus is attractive from a practical perspective.

Chapter 7

Finally, application of the new theory in conjunction with the exciting area of digital beamforming is investigated. Fabrication difficulties of the beamforming systems are discussed as challenging issues limiting the applicability of the digital beamforming technique. This chapter proposes a super-thin FSS-antenna array to help to simplify the fabrication process of such beamformers. In this scheme, to ease the fabrication, bulky, RF bandpass filters required in the receive path of the individual elements of the beamformer are eliminated. Instead, the necessary filtering is performed by an FSS structure placed over the antenna. This approach is tested numerically and experimentally through the application of a $\lambda/300$-thick miniaturized FSS separated from the antenna by a foam spacer with the thickness of $\lambda/10$. This proves that the miniaturized approach, unlike traditional FSSs, allows for creation of thin-layer spatial filters that can work at a close proximity of an antenna, thus demonstrating the versatility of miniaturized-element frequency-selective surfaces.

8.2 Future Work

Conformal Leaky Wave Antennas

In order to minimize air drag, it is generally desirable for antennas on moving platforms, such as aircraft or cars, to be conformal and free of other structures, such as radomes, which protrude from the vehicle surface. Designing low profile antennas, however, for use on curved surfaces presents a number of design challenges. One example of such an application is an array of planar patch antennas on an aircraft fuselage. Although, the curvature of the fuselage may be slight, phase shifters for each element are needed to correct for the curvature and send a collimated beam in the desired direction. As mentioned in [9], one particular advantage of leaky wave antennas is their applicability to curved surfaces.

Leaky wave antennas (LWA) have been studied extensively since first patented by Hansen in 1946 [116]. As a result of the numerous studies on LWA, their behavior is well understood

and a number of design guidelines have been developed [9, 117]. Advantages of LWA include ease of fabrication using printed circuit techniques, relatively low-profile design, and accurate control over beamwidth and scan angle. In addition, an advantage over arrays is the use of a single feed point rather than a complex feed network, which reduces complexity and cost. In [117], a number of simple design formulas for general 2-D LWA with partially reflecting surfaces (PRS), as seen in Figure 14, are presented; these results allow straightforward determination of the peak field values and beamwidths in the E- and H-planes as well as the pattern bandwidth.

For designing LWA on curved surfaces what is necessary is straightforward means to control the local surface admittance and, as a result, the longitudinal wavelength. Due to their localized performance, miniaturized surfaces provide such a means to control the amplitude and phase of the partially transmitted signal along the antenna and could be used to design conformal leaky wave antennas. Traditional FSS, which use larger unit cells and require a larger number of periods in the lattice, are unsuitable for accurate phase control over the antenna surface. The miniaturized FSS, however, can provide local control over the surface reactance and more accurate control of the radiated energy direction. In addition, these surfaces do not require vias and can be fabricated on thin, flexible substrates which are easily conformed to the curved surface.

To vary the guided wavelength using a miniaturized-element FSS, one way would be the introduction of clusters of scaled elements with slightly offset passband center frequencies. By slightly tuning the center frequency of the passband, at the frequency of operation the transmission coefficient phase and amplitude may be tuned. Another way would be to vary the gap capacitance along the length of the LWA.

Extremely Short Focal Length Lens

Another application of the proposed surfaces is in constructing very short focal length lenses. Reference [118] describes a filter-lens array system, which employs a planar array of bandpass antenna-filter-antenna elements in order to convert spherical into planar wave fronts. In this case, the ratio of the focal length to lens dimension (f/D) is 1.25. The bandpass elements are two patch antennas coupled through a coplanar waveguide resonator.

The elements on the periphery of the lens are slightly scaled to control their phase response and produce the desired wave transformation.

The miniaturized-element surfaces could be used in a slightly different configuration which would achieve the same focusing objective with minimized focal length over a finite aperture ($f/D \sim 0.2$). For example, in a transmit scenario a source point on the back of a thin dielectric slab, would create modes within the slab that radiate, similar to the leaky wave antenna described above. Here the miniaturized surface would be used to produce plane waves at the output of the lens structure. In receive mode, the surface could do the same of capturing incident energy and refocusing it back to the single source point.

This implementation is enabled by the unique advantages of the proposed surfaces. Most importantly, the small unit cell size allows tuning of the elements frequency response over small apertures to improve control over the transmission coefficient phase. The thin substrate allows the FSS to have 1–2 dB less insertion loss than the antenna-filter-antenna configuration described in [118]. In addition, low sensitivity to the angle of incident radiation permits them to be used for small f/D ratios.

One interesting future application would be to use the miniaturized-element FSSs at optical frequencies. In this application, a single solar cell could be used to collect the energy focused to it by a larger miniaturized-element lens. The layer could be produced using microfabrication techniques on flexible substrates, a sheet of which could lie above fewer solar cells, yielding the same areal coverage for lower cost. The response of the new surfaces would be tuned to capture the highest content portion of the solar radiation spectrum near 475 nm [10].

RF Insulators

The adverse effect of the human body on handheld wireless device operation is well known. Antenna efficiency, in particular, is degraded by the presence of the human hand on the device. There are also concerns over the effects of electromagnetic radiation on the human body and efforts have been made to minimize specific absorption rate (SAR). This application entails developing an encapsulating surface to insulate wireless devices from the human body. The proposed surfaces uniquely enable this application. The miniaturized

surfaces can be designed as a pure reactance to the enclosed antenna, shielding it from lossy dielectrics in the environment. This cannot be accomplished using metallic surfaces as they tend to short circuit the antenna.

8.3 Closing

$\nabla \times \vec{E} = -\partial \vec{B}/\partial t$	Faraday's law
$\nabla \times \vec{H} = \vec{J} + \partial \vec{D}/\partial t$	Modified Ampere's law
$\nabla \cdot \vec{D} = \rho_v$	Gauss's law of electricity
$\nabla \cdot \vec{B} = 0$	Gauss's law of magnetism

APPENDICES

APPENDIX A

FSS Simulation Using the Periodic Boundary Conditions in Ansoft HFSS

An overview of the full–wave analysis of frequency–selective surfaces using Ansoft HFSS is presented in this appendix. This short tutorial is based on the resources provided Ansoft.

Frequency–selective surfaces (FSSs) are fully described through their reflection and transmission characteristics. FSSs are 2–D planar, periodic arrays with an infinite extent. Usually, the problem of interest is the reaction of the FSS to an incident plane–wave. Given the infinite size of the FSS arrays, it can be shown (floquet's theorem) that the scattering from the entire array is known if the field information of a single period of the array (unit cell) is available. This condition assumes a plane–wave excitation.

This theorem is used in Ansoft HFSS to simulate frequency–selective surfaces. This is done through the modeling one unit cell and applying the periodic boundary conditions (PBC). The excitation is in general an incident plane–wave impinging upon the FSS from one side. The process of simulating an FSS in HFSS 11 is provided here through an example, including all the steps for modeling. Example considered here is the surface presented in Chapter 3, the loop–wire FSS.

Simulation Model Setup

The example considered here is a two–sided array of metallic patches on opposite sides of a substrate. After drawing the unit cell, the PBC is assigned as the boundary condition to each pair of the opposite side walls of the model in order to tell the solver that this unit cell belongs to an infinitely wide array in two–dimensional space. Over the top and bottom sides

of the box, perfectly–matched layers (PMLs) are used to absorb outgoing waves. Finally, the excitation is chosen to be the incident plane–wave. These steps are summarized in the following.

1) Draw the unit cell, including the substrate and the two metallic patches on either side of the substrate.
2) Draw an air box which includes the unit cell. The box sides must touch the substrate edges.

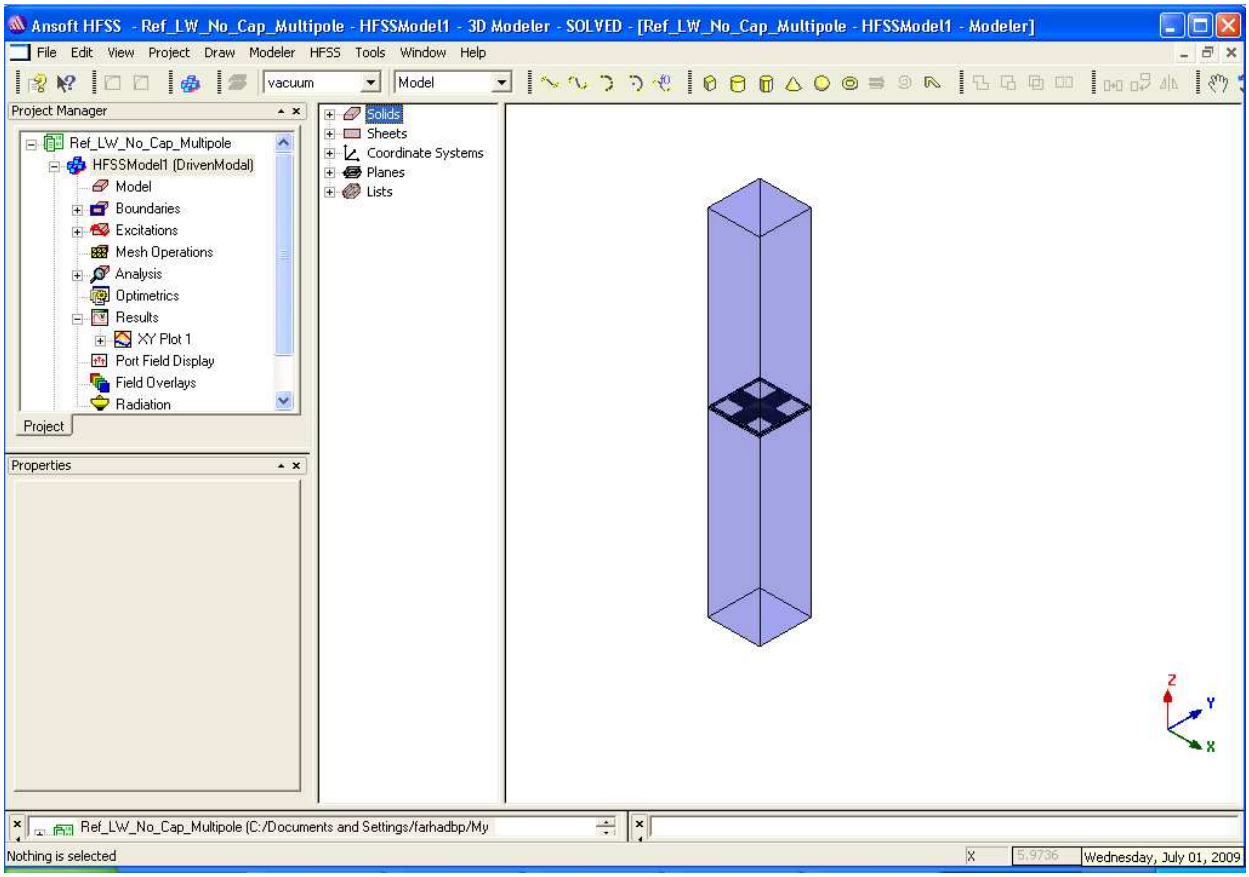

Figure A.1: The unit cell geometry inside the simulation air box

3) Assign PML to the top and bottom sides of the air box. Assume for this example that the excitation is propagating from the top toward down, along the $-\hat{z}$ direction. Select the top face of the air object and create a PML layer (check "Create PML Cover Objects on Selected Faces"). Next, check "Reference for FSS" as shown in Fig. A.2. Once the PML has

been created, select the bottom face of the air box to setup another PML over there. This time, do not check the box "Reference for FSS".

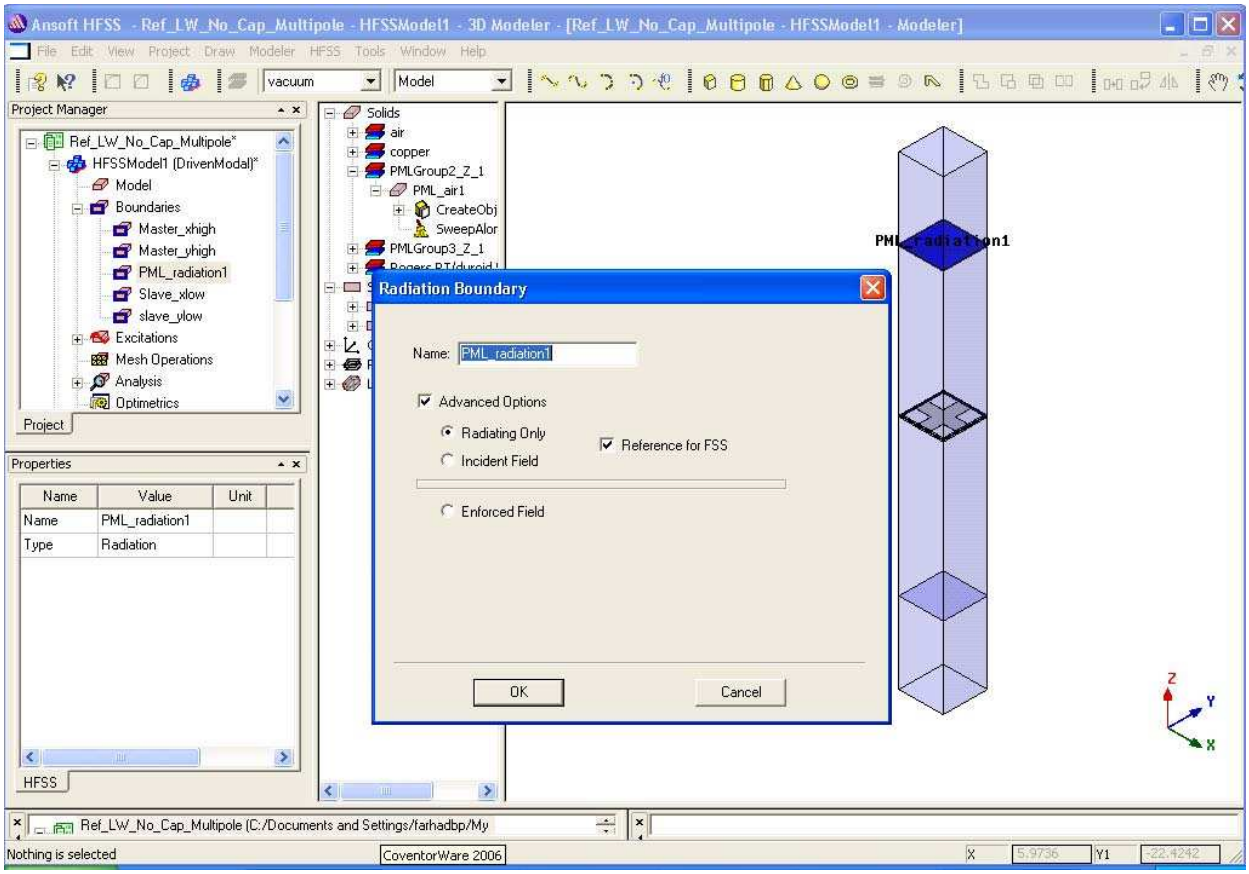

Figure A.2: PML assignment to the top face of the air box. PML should be also assigned to the bottom side.

The label "Reference for FSS" helps with fields post processing. To determine reflection, the software will integrate the "scattered field" over the base face of the PML that has this label. To determine transmission, the software will integrate the "total field" over the base face of the PML that does not have this label.

4) Draw four rectangular surfaces. Each rectangle covers one side of the entire model, including the air box and the two PMLs. PBC will be assigned to these surfaces.

5) Select two opposite surfaces. Assign the Master/Slave boundary conditions. One side

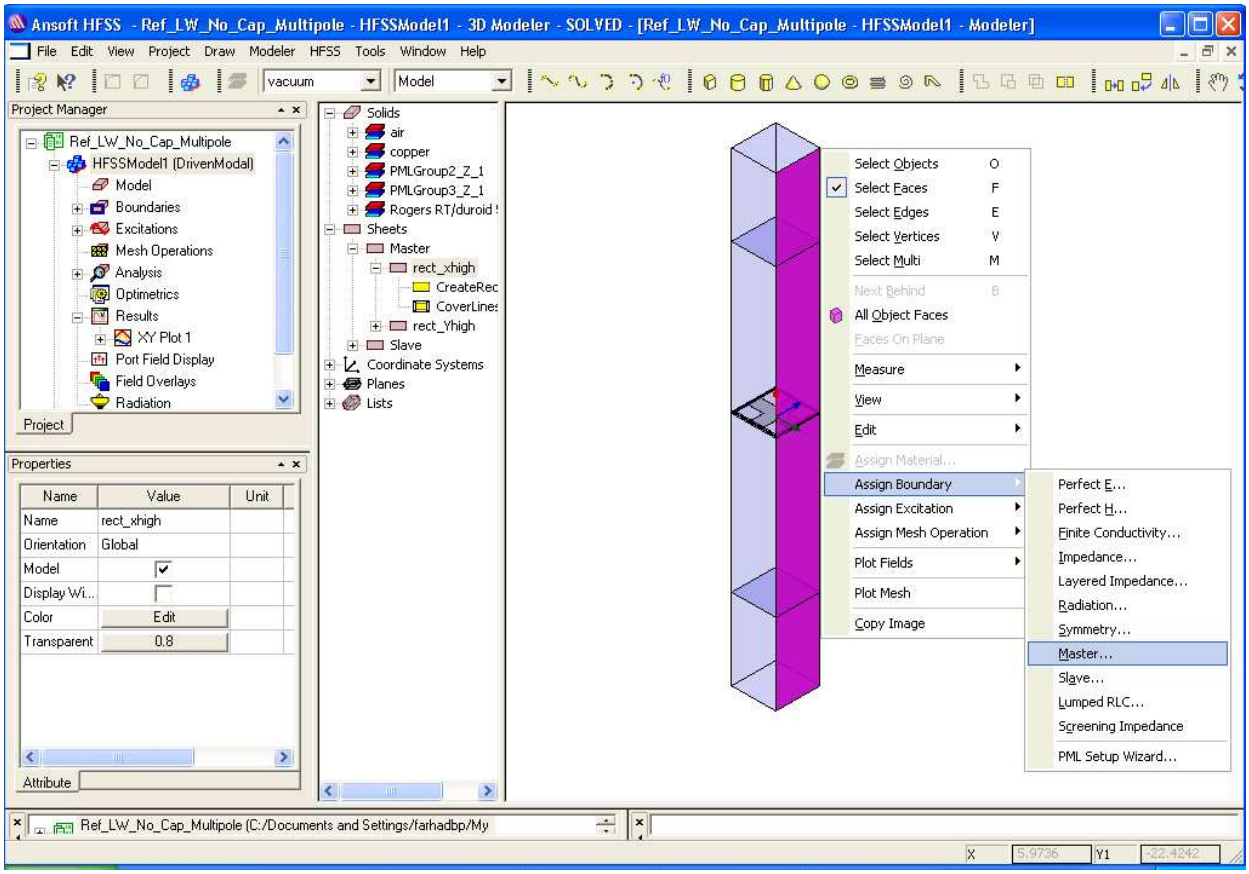

Figure A.3: PBC assignment to the rectangular surface in front. This surface is the Master. The surface opposite to this Master surface takes the Slave boundary.

surface is defined as the Master and the other one is the Slave for this Master wall. Similarly, the other two side surfaces will be assigned the Master/Slave boundary.

The scan angle of the slave boundaries is to be set according to the following rule: When the incident field comes from direction (*theta*,*phi*) then the scan angle will be (*theta*,*phi*+180^o). Physically, this is the direction of specular reflection off the FSS plane, but it applies to all the fields in the model. You can also set it to (-*theta*,*phi*); that results in the same angle. The final model is shown in Fig. A.5.

6) As the last step, a plane–wave in the spherical coordinate is assigned as the excitation. Notice that the the wave propagation angle is determined by a defined variable, mytheta, in this setup. This direction is described in the spherical system with (*theta*,*phi*) = (mytheta,0).

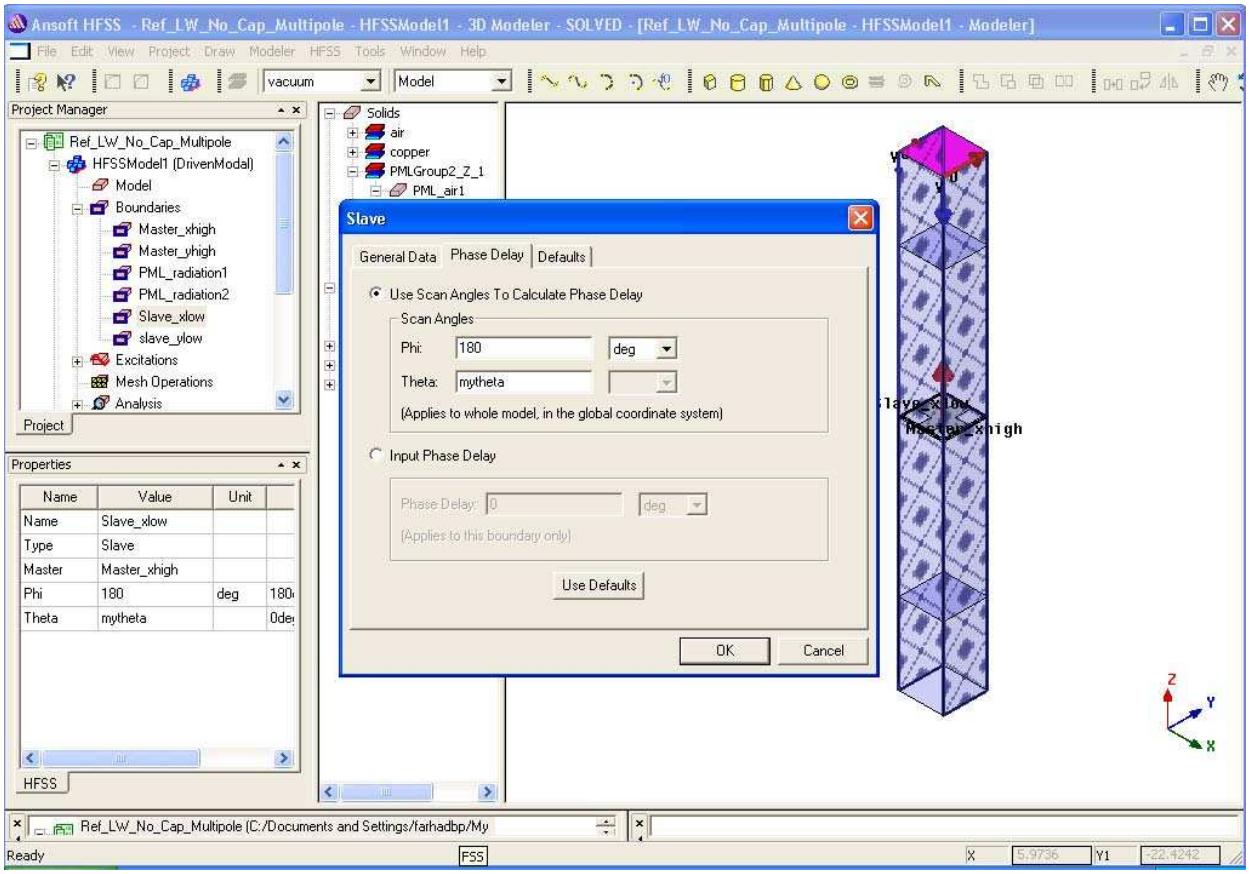

Figure A.4: Defining the scan angle in the PBC setup when the incident wave comes from direction (*theta*,*phi*) = (mytheta,0). mytheta is the variable representing the incidence angle of the plane–wave..

Fig. A.6 shows this assignment.

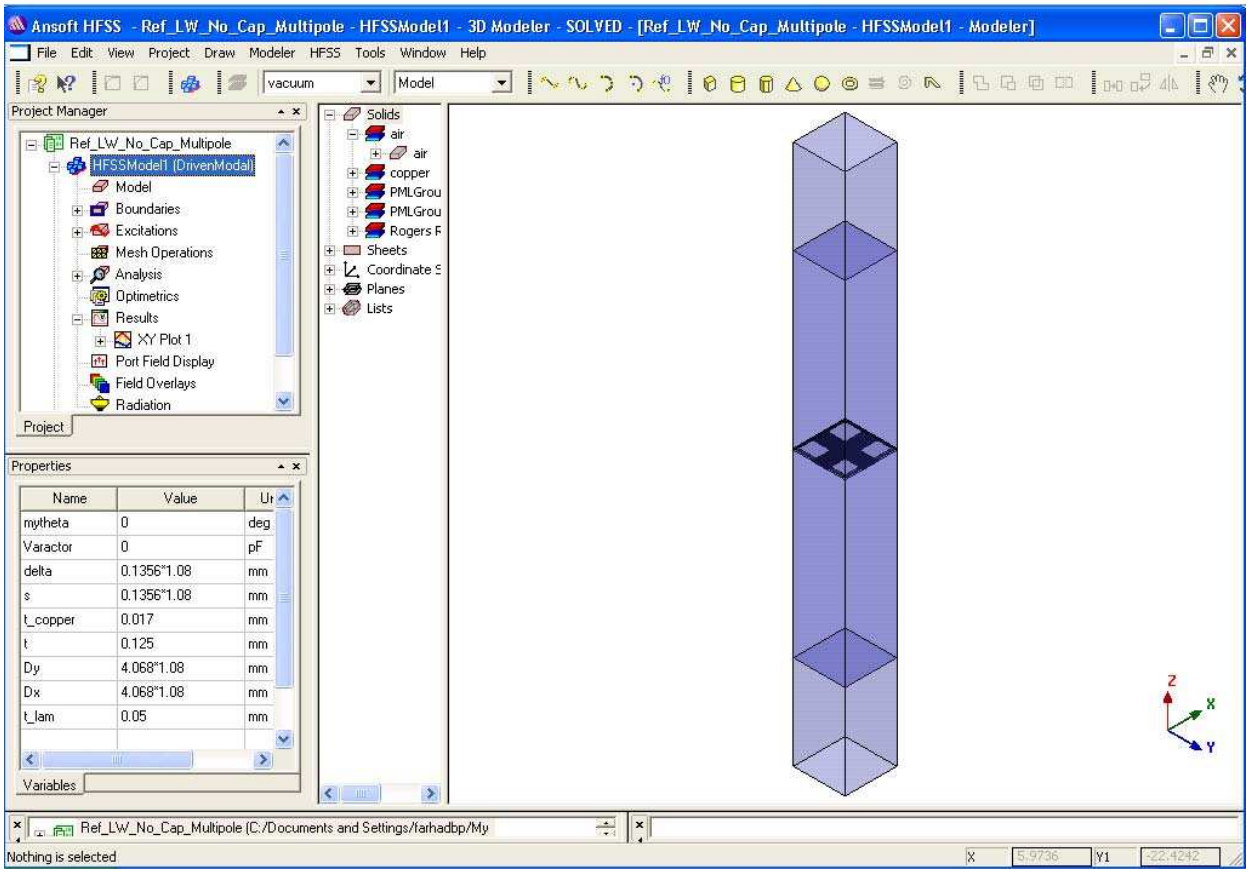

Figure A.5: FSS's simulation model using PML and PBC boundary conditions.

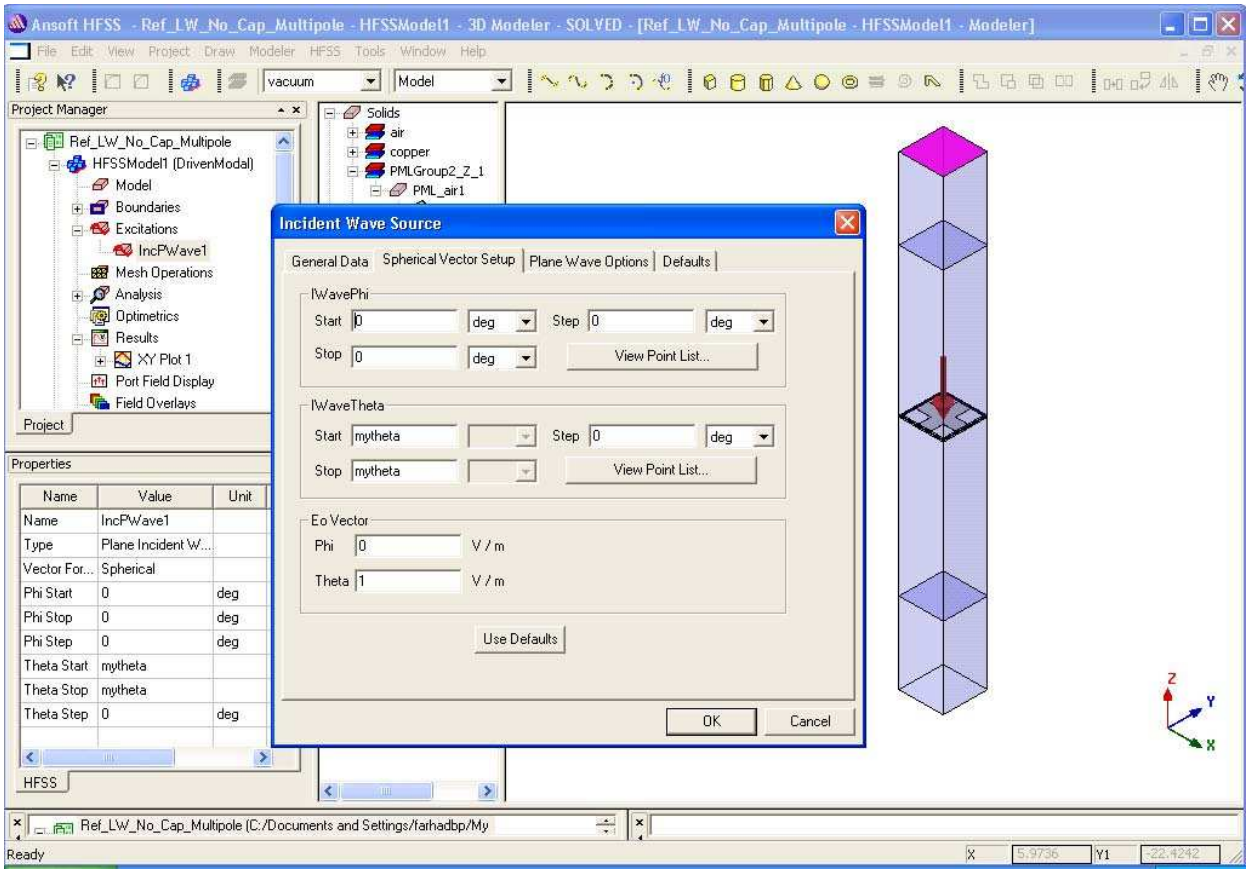

Figure A.6: Plane–wave excitation setup.

APPENDIX B

Contributions of This Research

Journal Articles

6) F. Bayatpur, K. Sarabandi, "Miniaturized FSS and patch antenna array coupling for angle-independent, high-order spatial filtering," submitted for review to IEEE Microw. Wireless Component Lett., 2009.

5) F. Bayatpur, K. Sarabandi, "Design and analysis of a tunable miniaturized-element frequency-selective surface without bias network," submitted for review to IEEE Trans. Antennas Propag., 2009.

4) F. Bayatpur, K. Sarabandi, "A tunable metamaterial frequency-selective surface with variable modes of operation," IEEE Trans. Microw. Theory Tech., vol. 57, issue 6, pp. 1433-1438, June 2009.

3) F. Bayatpur, K. Sarabandi, "Tuning performance of metamaterial-based frequency-selective surfaces," IEEE Trans. Antennas Propag., Vol. 57, no. 2, pp. 590-592, Feb. 2009.

2) F. Bayatpur, K. Sarabandi, "Multipole spatial filters using metamaterial-based miniaturized-element frequency-selective surfaces," IEEE Trans. Microw. Theory Tech., vol. 56, issue 12, pp. 2742-2748, Dec. 2009.

1) F. Bayatpur, K. Sarabandi, "Single-layer, high-order, miniaturized-element frequency selective surfaces," IEEE Trans. Microw. Theory Tech., vol. 56, issue 4, pp. 774-781, April 2008.

Conference Presentations

6) F. Bayatpur, K. Sarabandi, "A Metamaterial-Spatial Filter for Phased-Array Applications," Antennas and Propagation Society International Symposium, IEEE, June 2009.

5) F. Bayatpur, K. Sarabandi, "A Metamaterial Frequency-Selective Superstrate for Phased-Array Applications," Radar Conference, IEEE, May 2009.

4) F. Bayatpur, K. Sarabandi, "Design and Measurement of Multi-Band, Miniaturized-Element Frequency-Selective Surfaces," In Proceeding of the XXIX General Assembly of Union Radio Scientifique Internationale-URSI, August 2008.

3) K. Sarabandi, F. Bayatpur, "Miniaturized-Element Frequency Selective Surfaces," In Proceeding of the XXIX General Assembly of Union Radio Scientifique Internationale-URSI, August 2008.

2) F. Bayatpur, K. Sarabandi, "Multi-Layer Miniaturized-Element Frequency Selective Surfaces," Antennas and Propagation Society International Symposium, IEEE, July 2008.

1) F. Bayatpur, K. Sarabandi, "A Tunable, Band-Pass, Miniaturized-Element Frequency Selective Surface: Design and Measurement," Antennas and Propagation International Symposium, IEEE, June 2007.

BIBLIOGRAPHY

BIBLIOGRAPHY

[1] B.A. Munk, "Frequency-selective surfaces: Theory and design," Wiley, New York, 2000.

[2] T. K. Wu, "Frequency-selective surface and grid array," Wiley, New York, 1995.

[3] J. C. Vardaxoglou, "Frequency-selective surfaces: Analysis and design," Research Studies Press, Ltd., Taunton, UK, 1997.

[4] G. Marconi and C.S. Franklin, "Reflector for use in wireless telegraphy and telephony," U.S. Patent, 1,301,473 1919.

[5] W. R. Smythe, "Static and Dynamic Electricity," New York: McGraw- Hill, 1968, pp. 63-120.

[6] J. A. Kong, "Electromagnetic wave theory," Cambridge, MA: EMW Publishing, 2000, pp. 180-274.

[7] J. D. Kraus, R. J. Marhefka, "Antennas," McGraw-Hill Science Engineering, 2005.

[8] D. Pozar, "Microwave Engineering," pp. 125-160 , third edition, Wiley, New York, 2004.

[9] H. 10, "Antenna Engineering Handbook," Ch. 16, ed. F. J. Zucker, McGraw Hill, New York, 1961.

[10] "Solar Spectral Irradiance, "Handbook of Chemistry and Physics, 82nd Edition, CRC Press, Boca Raton, FL, 2001.

[11] D. Rittenhouse, "An optical problem, proposed by Mr. Hopkinson, and solved by Mr. Rittemhouse," Trans. Am. Philos. Soc. 2, 201-206, 1786.

[12] R. Ulrich, "Far-infrared properties of metallic mesh and its complementary structure," Infrared Phys. 7, 37-55 1967.

[13] S. W. Lee, G. Zarrillo, and C. L. Law, "Simple formulas for transmission through periodic metal grids or plates," IEEE Trans. Antennas Propag., AP-30, 904-909, 1982.

[14] R. Mittra, C. Chan, and T. Cwik, "Techniques for analyzing frequency selective surfaces- a review," IEEE Proc., 76(23), 1593-1615, 1988.

[15] P. D. Potter, "Improved dichroic reflector design for the 64-m antenna S- and X-band feed systems," JPL Tech. Rep. 32-1562, Feb., 1974.

[16] R. H. Ott et al., "Scattering by a two-dimensional periodic array of narrow plates," Radio Sci. 2(11), 1347-1359, 1967.

[17] C. C. Chen, "Scattering by a two-dimensional periodic array of conducting plates," IEEE Trans. Antennas Propag., AP-18(5), 660-665, 1967.

[18] C. C. Chen, "Transmission of microwave through perforated flat plates of finite thickness," IEEE Trans. Microw. Theory Tech., MTT-21(1), 1-6, 1973.

[19] J. P. Montgomery, "Scattering by an infinite periodic array of conductors on a dielectric sheet,"IEEE Trans. Antennas Propag., AP-23(1), 70-75, 1975.

[20] S. W. Schneider, B. A. Munk, "The scattering properties of super dense arrays of dipoles," IEEE Trans. Antennas Propag., AP-42(2), 463-472, 1994.

[21] E. L. Pelton, B. A. Munk, "Scattering from periodic arrays of crossed dipoles," IEEE Trans. Antennas Propag., AP-27(3), 323-330, 1979.

[22] S. M. Hamdy, P. A. Parker, "Influence of lattice geometry on transmission of electromagnetic waves through arrays of crossed dipoles," IEE Proc., Part H: Microwave, Opt. Antennas 129(1), 7-10, 1982.

[23] C. H. Tsao, R. Mittra, "Spectral-domain analysis of frequency selective surfaces comprised of periodic arrays of cross dipoles and Jerusalem crosses," IEEE Trans. Antennas Propag., AP-32(5), 478-486, 1984.

[24] R. J. Lagley, A. J. Drinkwater, "Improved empirical model for the Jerusalem cross," IEE Proc., Part H: Microwaves, Opt. Antennas 129(1), 1-6, 1982.

[25] E. L. Pelton, B. A. Munk, "A streamlined metallic radome," IEEE Trans. Antennas Propag., AP-22(6), 799-803 1974.

[26] B. A. Munk, "Periodic surface for large scan angle," U.S. Patent 3,789,404, 1974.

[27] E. A. Parker, S. M. A. Handy, "Rings as elements for FSS," Electron. Lett., 17(17), August, pp. 612-614, 1981.

[28] E. Parker, S. Hamdy, R. Langley, "Arrays of concentric rings as frequency selective surfaces," Electron. Lett. 17(23), 880, 1981.

[29] J. Huang, T. K. Wu, S. W. Lee, "Tri-band FSS with circular ring elements," IEEE Trans. Antennas Propag., AP-42(2), 166-175, 1994.

[30] R. J. Langley, E. A. Parker, "Equivalent circuit model for arrays of square loops," Electron. Lett., 18(7), 294-296, 1982.

[31] R. J. Langley, E. A. Parker, "Double-square frequency-selective surfaces and their equivalent circuit," Electron. Lett., 19(17), 675, 1983.

[32] C. K. Lee, R. Langley, "Equivalent circuit models for frequency selective surfaces at oblique angle of incidence," IEE Proc., Part H: Microwaves, Antennas Propag., 132(6), 395-398, 1985.

[33] T. K. Wu, "Single screen triband FSS with double-square-loop elements," Microwave Opt. Tech Lett., 5(2), 56-59, 1992.

[34] H. Rosen, U.S. Patent 4,785,310, 1988.

[35] E. A. Parker et al., "FSS," Proceeding ICAP 83, IEE Conf. Publ. 219, 459-463, 1983.

[36] C. C. Chen, "Transmission of microwave through perforated flat plates of finite thickness," IEEE Trans. Microw. Theory Tech., vol. 21, issue 1, pp. 1-6, Jan. 1973.

[37] K. Sarabandi and N. Behdad, "A frequency selective surface with miniaturized elements," IEEE Trans. Antennas Propag., Vol. 55, Issue. 5, pp. 1239-1245, May. 2007.

[38] F. Bayatpur, K. Sarabandi, "Single-layer, high-order, miniaturized-element frequency selective surfaces," IEEE Trans. Microw. Theory Tech., vol. 56, issue 4, pp. 774-781, April 2008.

[39] G. H Schennum, "Frequency selective surfaces for multiple frequency antennas," Microwave J., vol. 16(5), pp. 55-57, May 1973.

[40] V. D. Agrawal, W. A. Imbriale, "Design of a dichroic Cassegrah subreflector," IEEE Trans. Antennas Propag., vol. AP-27, no. 4, pp. 466-473, July 1979

[41] Y. Rahmat-Samii and M. Gatti, "Far-field patterns of space-borne antennas from near-field measurements," IEEE Trans. Antennas Propag., vol. AP-33, no. 6, pp. 638648, Jun. 1985.

[42] G. H Schennum, "The effect of perturbating a frequency-selective surface and its relation to the design of a dual-band surface," IEEE Trans. Antennas Propag., vol. 44, no. 3, pp. 368-374, Mar. 1996.

[43] T. K. Wu, "Four-band frequency selective surface with double-square-loop patch," IEEE Trans. Antennas Propag., vol. 42, issue. 12, pp. 1659-1663, Dec. 1994.

[44] T. K. Wu, S. W. Lee, "Multi-band FSS with multi-ring patch elements," IEEE Trans. Antennas Propag., AP-42(11), 1484-1490, 1994.

[45] M. Ohira, H. Deguchi, M. Tsuji, and H. Shigesawa, "Multiband singlelayer frequency selective surface designed by combination of genetic algorithm and geometry-refinement technique," IEEE Trans. Antennas Propag., vol. 52, no. 11, pp. 29252931, Nov. 2004.

[46] J. Romeu and Y. Rahmat-Samii, "Fractal FSS: A novel dual-band frequency selective surface," IEEE Trans. Antennas Propag., vol. 48, no.7, pp. 10971105, Jul. 2000.

[47] F. Bayatpur, K. Sarabandi, "Multipole spatial filters using metamaterial-based miniaturized-element frequency-selective surfaces," IEEE Trans. Microw. Theory Tech., vol. 56, issue 12, pp. 2742-2748, Dec. 2009.

[48] Comtesse, L. E., Langley, R. J., Parker, E. A., Vardaxoglou, J. C., "Frequency selective surfaces in dual and triple band offset reflector antennas," European Microwave Conference, 1987. 17th, pp. 208 - 213, Oct. 1987.

[49] T. K. Wu, "Double-square-loop FSS for multiplexing four (S/X/Ku/Ka) bands," in 1991 Int. IEEE AP-S Symp. Dig., Ont., Canada, June 1991, pp. 1885-1888.

[50] S. W. Lee and T. J. Fong, "Electromagnetic wave scattering from an active corrugated structure," J. Appl. Phys. 43(2), 388-396 (1972).

[51] J. A. Arnaud and F. A. Pelow, "Resonant-grid quazi-optical diplexers," Bell Syst. Tech. J., 54(2), 263-283 (1975).

[52] I. Anderson, "On the theory of self-resonant grids," Bell Syst. Tech. J. 54(10), 1725-1731, 1975.

[53] W. W. Lam, H. Z. Chen, K. S. Stolt, C. F. Jou, N. C. Luhmann, Jr., and D. B. Rutledge, "Millimeter-wave diode-grid phase shifters," IEEE Trans. Microw. Theory Tech., MTT-36(5), 902-907, 1988.

[54] R. J. Langley, E. A. Parker, "An equivalent circuit study of a PIN diode switched active FSS," Rep. Br. Aerosp. plc, Feb. 1990.

[55] H. X. King, N. C. Luhmann, Jr., X. H. Qin, L. B. Sjogren, W. Wu, D. B. Rutledge, J. Maserjian, U. Lieneweg, C. Zah, and R. Bhat, "Millimeter-wave quasi-optical active arrays," Proc. Int. Conf. Space Terahertz Technol., 2nd, pp. 293-305, 1991.

[56] K. D. Stephan, F. H. Spooner, and P. F. Glodsmith, "Quasioptical millimeter-wave hybrid and monolithic PIN diode switches," IEEE Trans. Microw. Theory Tech., vol. 41, issue 10, pp. 1791-1798, 1993.

[57] L. B. Sjogren, H. N. Liantz Liu, F. Wang, T. Liu, W. Wu, X. H. Qin, E. Chung, C. W. Domier, and N. C. Luhmann, Jr., "A monolithic millimeter-wave diode array beam transmitance controller," IEEE Trans. Microw. Theory Tech., vol. 41, issue 10, pp. 1782-1790, 1993.

[58] D. Sievenpiper, L. Zhang, R. F. Jimenez Broas, N. G. Alexpolous, E. Yablonvitch, "High-impedance electromagnetic surfaces with a forbidden frequency band," IEEE Trans. Microw. Theory Tech., vol. 47, issue 11, pp. 2059-2074, Nov. 1999.

[59] R.F.J. Broas, D.F. Sievenpiper, E. Yablonovitch, "A high-impedance ground plane applied to a cellphone handset geometry," IEEE Trans. Microw. Theory Tech., vol. 47, issue 7, pp. 1262-1265, Jul. 2001.

[60] S. Ramo, J. Whinnery, and T. Van Duzer, "Fields and waves in communication electronics," 2nd ed., New York: Wiley, 1984.

[61] R. Collin, "Field theory of guided waves," 2nd ed., New York: IEEE press, 1991.

[62] Babakhani, A. Xiang Guan Komijani, A. Natarajan, A. Hajimiri, A., "A 77-GHz Phased-Array Transceiver With On-Chip Antennas in Silicon: Receiver and Antennas," IEEE J. solid-state circuits, vol. 41, issue 12, pp. 2795-2806, Dec. 2006.

[63] Kwang-Jin Koh, May, J.W., Rebeiz, G.M.,"A Millimeter-Wave (4045 GHz) 16-Element Phased-Array Transmitter in 0.18-..m SiGe BiCMOS Technology," IEEE J. solid-state circuits, vol. 44, issue 5, pp. 1498-1509, May 2009.

[64] H. Steyskal, "Digital beamforming antennas - An introduction," Microw. J., pp. 107-124, Jan. 1987.

[65] D. R. Jackson, N. G. Alexopoulos, "Gain enhancement methods for printed circuit antennas," IEEE Trans. Antennas Propag., vol. 33, issue 9, pp. 976-987, 1985.

[66] D. R. Jackson, A. A. Oliner, "A leaky-wave analysis of the high-gain printed antenna configuration," IEEE Trans. Antennas Propag., vol. 36, issue 7, pp. 905-910, 1988.

[67] H. Y. Yang, N. G. Alexopoulos, "Gain enhancement methods for printed antennas through multiple superstrates," IEEE Trans. Antennas Propag., vol. 35, issue 7, pp. 860-863, 1987.

[68] A. P. Feresidis, G. Goussetis, S. Wang, and J. C. Vardaxoglou, "Artificial magnetic conductor surfaces and their application to low-profile high-gain planar antennas," IEEE Trans. Antennas Propag., vol. 53, issue 1, pp. 209-215, 2005.

[69] L. Zhang, H. Contopanagos, N. G. Alexopoulos, and E. Yablonovitch, "An electromagnetic bandgap resonator antenna," in Proc. IEEE Antennas Propag. Society Int. Symp., Jun. 21-26, 1998, vol. 1, pp. 186-189.

[70] Thevenot, M. Cheype, C. Reineix, A., Jecko, B., "Directive photonic-bandgap antennas," IEEE Trans. Microw. Theory Tech., vol. 47, issue 11, pp. 2115-2122, Nov. 1999.

[71] Cheype, C. Serier, C., Thevenot, M., Monediere, T., Reineix, A., Jecko, B., "An electromagnetic bandgap resonator antenna," IEEE Trans. Antennas Propag., vol. 50, issue 9, pp. 224-235, Jan. 2005.

[72] Y. J. Lee, J. Yeo, R. Mittra, and W. S. Park, "Application of electromagnetic bandgap (EBG) superstrates with controllable defects for a class of patch antennas as spatial angular filters," IEEE Trans. Antennas Propag., vol. 53, issue 1, pp. 224-235, Jan. 2005.

[73] D.H. Lee, Y.J. Lee, J. Yeo, R. Mittra and W.S. Park, "Design of novel thin frequency selective surface superstrates for dual-band directivity enhancement," Microwaves, Antennas Propag., IET, volume 1, issue 1, pp. 248-254, Feb. 2007.

[74] Yeo, J.; Mittra, R., "Bandwidth enhancement of multiband antennas using frequency selective surfaces for ground planes," IEEE AP-S Symp. Vol. 4, pp. 366-369, July 2001

[75] E. A. Parker, C. Antonopoulos, and N. E. Simpson, "Microwave Band FSS in Optically Transparent Conducting Layers: Performance of ring element arrays," Microwave and Optical Technology Letters, vol. 16, no. 2, October 1997, pp. 61-63.

[76] J. Hirai and I. Yokota, "Electro-magnetic shielding glass of frequency selective surfaces," Proceedings of the International Symposium on electromagnetic compatibility, 17-21 May 1999, pp. 314-316.

[77] www.nipponpaint.co.jp

[78] T. Cwik, R. Mittra, K. C. Lang, T. K. Wu, "Frequency selective screens," IEEE Antennas Propag., Newsl., Feature Article, April 1987.

[79] P. W. Hannan and M. A. Balfour, "Simulation of a phased array antenna in waveguide," IEEE Trans. Antennas Propag., AP-13, 342, 1965.

[80] D. K. Ghodgaonka, V. V. Varadan, and V. J. Varadan, "A free-space method for measurement of dielectric constants loss tangents at microwave frequencies," IEEE Trans. Instrum. Meas. IM-37(3), 789-793, 1989.

[81] G. Arjavalingam et al., "Characterization of quasi-optical filters with picosecond transient radiation," IEEE Trans. Antennas Propag., AP-40(1), 63-66, 1992.

[82] F. Bayatpur, K. Sarabandi, "Tuning performance of metamaterial-based frequency-selective surfaces," IEEE Trans. Antennas Propag., Vol. 57, no. 2, pp. 590-592, Feb. 2009.

[83] B. Monacelli, J.B. Pryor, B.A. Munk, D. Kotter, G.D. Boreman,"Infrared frequency selective surface based on circuit-analog square loop design," IEEE Trans. Antennas Propag., Vol. 53, no. 2, pp. 745-752, Feb. 2005.

[84] S. W. Lee, "Scattering by dielectric-loaded screen," IEEE Trans. Antennas Propag., AP-19(5), 656, 1971.

[85] T. K. Chang, R. J. Langley, and E. A. Parker, "Frequency selective surfaces on biased ferrite substrates," IEE Electron. Lett., vol. 30, no. 15, pp. 1193-1194, Jul. 1994.

[86] G. Y. Li, Y. C. Chan, T. S. Mok, and J. C. Vardaxoglou, "Analysis of frequency selective surfaces on biased ferrite substrate," in IEEE AP-S Dig., vol. 3, Jun. 1995, pp. 1636-1639.

[87] Y. Liu, C. G. Christodoulou, P. F. Wahid, and N. E. Buris, "Analysis of frequency selective surfaces with ferrite substrates," in IEEE AP-S Dig., vol. 3, Jun. 1995, pp. 18-23.

[88] Y. C. Chan, G. Y. Li, T. S. Mok, and J. C. Vardaxoglou, "Analysis of a tunable frequency-selective surface on an in-plane biased ferrite substrate," Microwave Opt. Technol. Lett., vol. 13, no. 2, pp. 59-63, Oct. 1996.

[89] Y. Liu, C. G. Christodoulou, and N. E. Buris, "Fullwave analysis method for frequency selective surfaces on ferrite substrates," J. Electromagn. Waves Applicat., vol. 11, no. 5, pp. 593-607, 1997.

[90] E. A. Parker and S. B. Savia, "Active frequency selective surfaces with ferroelectric substrates," in Proc. Inst. Elect. Eng. Microwaves, Antennas, Propag., vol. 148, Apr. 2001, pp. 103-108.

[91] J. C. Vardaxoglou, "Optical switching of frequency selective surface bandpass response," IEE Electron. Lett., vol. 32, no. 25, pp. 2345-2346, Dec. 1996.

[92] A. C. de C. Lima, E. A. Parker, and R. J. Langley, "Tunable frequency selective surface using liquid substrates," IEE Electron. Lett., vol. 30, no. 4, pp. 281-282, Feb. 1994.

[93] T. Anderson, I. Alexeff, and J. Raynolds, "Plasma frequency selective surfaces," in Proc. IEEE Int. Conf. Plasma Science, June 2003, p. 237.

[94] J. A. Bossard, D. H.Werner, T. S. Mayer, and R. P. Drupp, "A novel design methodology for reconfigurable frequency selective surfaces using genetic algorithms," IEEE Trans. Antennas Propag., vol. 53, no. 4, pp. 1390-1400, Apr. 2005.

[95] J. M. Zendejas, J. P. Gianvittorio, and Y. Rahmat-Samii, "Magnetic MEMS reconfigurable frequency-selective surfaces," J. Microelectromech. Syst., vol. 15, no. 3, pp. 613623, Jun. 2006.

[96] B. Schoenlinner, A. Abbaspour-Tamijani, L. C. Kempel, and G. M. Rebeiz, "Switchable low-loss RF MEMS Ka-band frequency-selective surface," IEEE Trans. Microw. Theory Tech., Vol. 52, pp. 2474-2481, Nov. 2004.

[97] J. P. Gianvittorio, J. Zendejas, Y. Rahmat-Samii, and J. Judy, "Reconfigurable MEMS-enabled frequency selective surfaces," IEE Electron.Lett., vol. 38, no. 25, pp. 1627-1628, Dec. 2002.

[98] I. C. Hunter and J. D. Rhodes, "Electronically tunable microwave bandpass filters," IEEE Trans. Microw. Theory Tech., vol. MTT-30, no. 9, pp. 13541360, Sep. 1982.

[99] M. Makimoto and M. Sagawa, "Varactor tuned bandpass filters using microstrip-line ring resonators," in IEEE MTT-S Int. Microw. Symp. Dig., Jun. 1986, pp. 411414.

[100] S. R. Chandler, I. C. Hunter, and J. G. Gardiner, "Active varactor tunable bandpass filter," IEEE Microw. Guided Wave Lett., vol. 3, no. 3, pp. 7071, Mar. 1993.

[101] A. R. Brown and G. M. Rebeiz, "A varactor-tuned RF filter," IEEE Trans. Microw. Theory Tech., vol. 48, no. 7, pp. 11571160, Jul. 2000.

[102] T. K. Chang, R. J. Langley, and E. Parker, "An active square loop frequency selective surface," IEEE Microwave Guided Wave Lett., vol. 3, no. 10, pp. 387-388, Oct. 1993.

[103] T. K. Chang, R. J. Langley, and E. A. Parker, "Active frequency-selective surfaces," in Proc. IEEE Microwaves, Antennas Propag., vol. 143, Feb. 1996, pp. 62-66.

[104] C. Mias, "Varactor-tunable frequency selective surface with resistive-lumped-element biasing grids," IEEE Microwave and Wireless Components Lett., vol. 15, no. 9, Sept. 2005.

[105] F. Bayatpur, K. Sarabandi, "A tunable metamaterial frequency-selective surface with variable modes of operation," IEEE Trans. Microw. Theory Tech., vol. 57, issue 6, pp. 1433-1438, June 2009.

[106] B. Philips, E. A. Parker, and R. J. Langley, "Active FSS in an experimental horn antenna switchable between two beamwidths," IEE Electron. Lett., vol. 31, no. 1, pp. 1-2, Jan. 1995.

[107] B. M. Cahill and E. A. Parker, "Field switching in an enclosure with active FSS screen," IEE Electron. Lett., vol. 37, no. 4, pp. 244-245, Feb. 2001.

[108] F. Bayatpur, K. Sarabandi, "Design and analysis of a tunable miniaturized-element frequency-selective surface without bias network," submitted for review to IEEE Trans. Antennas Propag., 2009.

[109] F. Bayatpur, K. Sarabandi, "Miniaturized FSS and patch antenna array coupling for angle-independent, high-order spatial filtering," submitted for review to IEEE Microw. Wireless Component Lett., 2009.

[110] F. Bayatpur, K. Sarabandi, "A Metamaterial Frequency-Selective Superstrate for Phased-Array Applications," Radar Conference, IEEE, May 2009.

[111] www.rogerscorp.com

[112] www.arlonmed.com

[113] www.taconic.com

[114] www.avx.com

[115] www.macom.com

[116] W. W. Hansen, "Radiating electromagnetic waveguide," U. S. Patent No. 2,402,622.

[117] T. Zhao, D. R. Jackson, J. T. Williams, and A. A. Oliner, "General Formulas for 2-D Leaky-Wave Antennas," IEEE Trans. Antennas Propag., vol. 53, no. 11, pp. 3525-3533, Nov. 2005.

[118] A. Abbaspour-Tamijani, K. Sarabandi and G. M. Rebeiz, "A millimeter-wave bandpass filter-lens array," IET Microwave, Antennas, Propag., vol. 1, no. 2, pp. 388-395, April 2007.